Microfabricated All-Around-Electrode AC Electro-osmotic Micropump

THÈSE N^{O} 5316 (2012)

PRÉSENTÉE LE 23 MARS 2012

À LA FACULTÉ DES SCIENCES ET TECHNIQUES DE L'INGÉNIEUR
LABORATOIRE DE CAPTEURS, ACTUATEURS ET MICROSYSTÈMES
PROGRAMME DOCTORAL EN MICROSYSTÈMES ET MICROÉLECTRONIQUE

ÉCOLE POLYTECHNIQUE FÉDÉRALE DE LAUSANNE

POUR L'OBTENTION DU GRADE DE DOCTEUR ÈS SCIENCES

PAR

Luca RIBETTO

acceptée sur proposition du jury:

Prof. P.-A. Farine, président du jury
Prof. N. de Rooij, Dr A. Homsy, directeurs de thèse
Dr S. Lani, rapporteur
Dr S. Renard, rapporteur
Prof. H. Shea, rapporteur

ÉCOLE POLYTECHNIQUE
FÉDÉRALE DE LAUSANNE
Suisse
2012

This is impossible, she whispered to the Hatter, standing loyally beside her foot.
Only if you believe it is, said the Mad Hatter.

— *Alice in Wonderland*, adaptation of T. T. Sutherland

Abstract

This thesis presents the fabrication and characterisation of AC electro-osmotic micropumps with a simple design and velocity generation enhanced by about four times with respect to devices with simpler designs. Electro-osmosis is a convenient and effective method to pump liquids without the need for moving components. The implementation of valveless micropumps is important for the realisation of safe and robust biomedical devices, which require long-term reliability. AC electro-osmosis has the advantage, over other kinds of pumping strategies, of being implementable with relatively simple geometries and fabrication processes. Moreover, it uses low voltages and avoids undesired phenomena such as electrolysis, thus being suitable for the implementation in implantable devices that should operate in a closed environment. Whereas AC electro-osmotic pumps presented in the literature exploit planar electrode designs and fail to generate good values of velocity and pressure, the prototypes presented in this work have electrodes patterned all around the pumping channel and can generate much larger values. Moreover, with respect to other improved prototypes based on 3D electrode geometries, our devices are simpler to fabricate and give comparable enhancements of the performances. In this work, we present the development of the all-around-electrode devices and give a theoretical explanation for the measured improvements in velocity generation. The fabrication process is carried out in the cleanroom by depositing Ti/Pt electrodes on pre-structured Pyrex substrates and requires only three lithographic steps. The performances of the fabricated devices are characterised as a function of the applied voltage and frequency, and the dynamic behaviour of the prototypes is studied using the Fourier transform. In order to evaluate the suitability of the pumps for biomedical fluids, the dependence of velocity generation on the concentration of the pumped solution is also addressed. Finally, we show that the fabrication process can be adapted to an industrial batch manufacture requiring lower costs by substituting the Pyrex substrates with thin plastic foils. All-around-electrode micropumps can be successfully fabricated by patterning metal electrodes onto 12-μm-thick plastic foils and the costs might be further reduced by substituting the metal structures with inkjet-printed conductive-polymer electrodes.

Keywords: Microfluidics, Valveless micropump, AC electro-osmosis, Microfabrication, All-around electrode, Pyrex wafer, Plastic foil.

Résumé

Cette thèse présente la fabrication et la caractérisation de micropompes électro-osmotiques AC (EOAC) ayant un design simple et capables de générer une vitesse accrue d'environ quatre fois par rapport à des dispositifs avec un design plus simple. L'électro-osmose est une méthode pratique et efficace pour pomper des liquides sans avoir recours à des composants mobiles. Le développement de micropompes sans vanne est importante afin de garantir la sécurité et la fiabilité à long terme requises par les systèmes biomédicaux. Par rapport à d'autres stratégies de pompage, l'électro-osmose AC a l'avantage d'être réalisable avec des géométries et des procédés de fabrication relativement simples. Par ailleurs, les pompes EOAC utilisent de basses tensions et évitent des phénomènes indésirables tels que l'électrolyse, étant ainsi adaptées à être implantées et fonctionner dans un environnement fermé. Alors que les pompes EOAC présentées dans la littérature sont basées sur un design d'électrodes planaires et ne parviennent pas à générer de bonnes valeurs de vitesse et de pression, les prototypes présentés dans ce travail sont réalisés avec des électrodes situées tout autour du canal de pompage et génèrent des vitesses beaucoup plus élevées. De plus, par rapport à d'autres pompes au design amélioré exploitant des électrodes 3D, nos dispositifs sont plus simples à fabriquer et nous permettent d'obtenir des performances comparables. Dans ce travail, nous présentons le développement de micropompes EOAC et donnons une explication théorique aux mesures expérimentales. Le procédé de fabrication est effectué en salle blanche. Des électrodes en Ti/Pt sont déposées sur des plaques en Pyrex qui ont été structurées au préalable, et seulement trois étapes de lithographie sont nécessaires. Les dispositifs fabriqués sont caractérisés en fonction de la tension et de la fréquence du signal appliqué, et le comportement dynamique des prototypes est étudié à l'aide de la transformée de Fourier. Afin d'évaluer le potentiel des pompes pour les application avec des fluides biomédicaux, la vitesse générée est également étudiée en fonction de la concentration de la solution pompée. Enfin, nous montrons que le procédé de fabrication peut être adapté à une fabrication industrielle nécessitant des coûts réduits en remplaçant les substrats en Pyrex par des feuilles minces en plastique. Les micropompes améliorées peuvent être fabriquées en déposant des électrodes métalliques sur des feuilles en plastique de 12 μm d'épaisseur, et les coûts pourraient être encore réduits en remplaçant les électrodes en métal par des électrodes en polymère conducteur imprimées par jet d'encre.

Mots-clefs : Microfluidique, Micropompe sans vannes, Électro-osmose AC, Microfabrication, Électrode autour du canal, Pyrex, Feuille plastique.

Riassunto

Questa tesi presenta la fabbricazione e la caratterizzazione di micropompe elettrosmotiche AC con un design semplice e una generazione di velocità aumentata di circa quattro volte rispetto a dispositivi dal design più semplice. L'elettrosmosi è un metodo pratico ed efficace per pompare liquidi senza la necessità di componenti mobili. L'implementazione di micropompe senza valvole è importante per la realizzazione di dispositivi biomedici sicuri e resistenti, che richiedono affidabilità a lungo termine. L'elettrosmosi AC ha il vantaggio, rispetto ad altre strategie di pompaggio, di essere realizzabile con geometrie e processi di fabbricazione relativamente semplici. Inoltre le pompe elettrosmotiche AC (EOAC) fanno uso di basse tensioni e riescono ad evitare fenomeni indesiderati come l'elettrolisi. Sono quindi adatte ad essere integrate in dispositivi impiantabili che dovrebbe operare in un ambiente chiuso. Mentre la maggior parte delle pompe EOAC descritte in letteratura sono basate su elettrodi planari e non riescono a generare sufficienti valori di velocità e pressione, i prototipi presentati in questo lavoro hanno elettrodi su tutti i lati del canale di pompaggio e sono in grado di generare velocità molto più grandi. Inoltre, rispetto ad altri prototipi dal design migliorato basati su elettrodi tridimensionali, i nostri dispositivi sono più semplici da fabbricare e mostrano un simile miglioramento delle prestazioni. In questa tesi presentiamo lo sviluppo di dispositivi con elettrodi su tutti i lati del canale e diamo una spiegazione teorica all'incremento della velocità generata. Il processo di fabbricazione avviene in camera bianca e consiste nel depositare elettrodi in Ti/Pt su wafer in Pyrex prestrutturati, utilizzando solo tre passaggi di litografia. Le prestazioni dei dispositivi fabbricati sono caratterizzate in funzione della tensione e della frequenza del segnale applicato e il comportamento dinamico dei prototipi viene studiato attraverso la trasformata di Fourier. Allo scopo di valutare l'idoneità di queste pompe per fluidi biomedicali, è stata valutata anche la dipendenza della velocità generata dalla concentrazione della soluzione da pompare. Infine, dimostriamo che il processo di fabbricazione può essere adattato ad una produzione industriale e a basso costo sostituendo i wafer di Pyrex con sottili fogli di plastica. Le micropompe con elettrodi su tutti i lati del canale possono essere realizzate depositando elettrodi metallici su fogli di plastica spessi 12 μm ed i costi possono essere ulteriormente ridotti sostituendo le strutture metalliche con elettrodi in polimero conduttore prodotti con una stampante a getto d'inchiostro.

Parole chiave: Microfluidica, Micropompa senza valvole, Elettro-osmosi AC, Microfabricazione, Elettrodi intorno al canale, Wafer in Pyrex, Foglio di plastica.

Contents

List of Abbreviations

1SE	One-Side-Electrode
2SE	Two-Side-Electrode
AAE	All-Around-Electrode
AC	Alternating Current
ACE	Acetone
ACEO	AC Electro-Osmotic
DC	Direct Current
DCEO	DC Electro-Osmotic
DI	DeIonised
DNA	DeoxyriboNucleic Acid
DRIE	Deep Reactive Ion Etching
EDL	Electric Double-Layer
EHD	ElectroHydroDynamic
EO	Electro-Osmosis
ESEM	Environmental Scanning Electron Microscope
EWOD	ElectroWetting On Dielectrics
FEM	Finite Element Method
FFT	Fast Fourier Transform
IPA	Isopropanol
ITO	Indium-Tin Oxyde
LOC	Lab-On-a-Chip
LPCVD	Low Pressure Chemical Vapour Deposition
MEMS	Micro Electro-Mechanical Systems
MHD	MagnetoHydroDynamic
MPB	Modified Poisson-Boltzmann
μTAS	micro Total Analysis System
NMR	Nuclear Magnetic Resonance
NOA81	Norland Optical Adhesive 81

PB	Poisson-Boltzmann
PBS	Phosphate Buffered Saline
PCR	Polymerase Chain Reaction
PDMS	PolyDiMethylSiloxane
PEDOT	Poly(3,4-EthyleneDiOxyThiopene)
PEDOT:PSS	PEDOT Poly(StireneSulfonate)
PET	Poly Ethylene Terephtalate
PIV	Particle Image Velocimetry
μPIV	micro Particle Image Velocimetry
PMMA	PolyMethylMetAcrilate
PUR	PolyURethane
RIE	Reactive Ion Etching
rms	Root Mean Square
SAW	Surface Acoustic Waves
SEM	Scanning Electron Microscope
TW	Travelling Wave
TWEO	Travelling Wave Electro-Osmotic
UV	Ultra-Violet

List of Symbols

a	Size of an ion
α	v_{ave}/v_{max} in a Poiseuille flow
B	Magnetic field
β	$\mathscr{P}_{electrodes}/\mathscr{P}_{channel}$
c_-	Concentration of negative ions
c_+	Concentration of positive ions
c	Concentration of the solution
C	Electric capacitance
d	Diameter
Δp	Pressure difference, or backpressure
Δp_{hyd}	Hydrostatic pressure
δ	Uncertainty
ϵ	Electrical permittivity
η_{conv}	Power conversion efficiency
η	Dynamic viscosity of the fluid
E	Electric field
e	Elementary charge
F	Force
f	Frequency
Fr	Framerate
g	Acceleration of gravity
γ_{la}	Surface tension between liquid and air
γ_{sa}	Surface tension between solid and air
γ_{sl}	Surface tension between solid and liquid
h	Height
I	Electric current
J	Electric current density
k	Width-ratio of the electrodes

k_B	Boltzmann constant
κ	$L_{electrodes}/L_{channel}$
L	Length
L_0	Characteristic length
λ_D	Debye length
ν	Packing parameter
ω	Angular frequency
$\mathscr{P}$	Perimeter
ϕ	Phase
ψ	Electric potential
Q	Flow-rate
R_{hyd}	Hydraulic resistance
R	Radius
R	Electric resistance
Re	Reynolds number
ρ	Density of the fluid
ρ_{el}	Density of electric charges
S	Cross-section area
σ_0	Conductivity of the solution
σ	Relative error
t	Time
T	Temperature
θ	Contact angle
v	Velocity
v_0	Characteristic velocity
v_{ave}	Average velocity in a channel
V_0	Applied voltage
V	Voltage
W_{el}	Electrical power consumption
W_{hyd}	Hydraulic power
w	Width
x	x-coordinate
ζ	Zeta potential
Z_i	Valence of the ions in solution
Z	Electric impedance

1 Microfluidics and Micropumps

Dealing with fluids on the micro scale engages phenomena that are very much different to what is commonly observed in life on the macro scale. Not only are quantities involving volumes and energies incredibly smaller, but materials interact with one another in different ways. Forces that we can usually neglect become predominant. Physical effects take place, which are not observed on the macro scale. When these phenomena are clearly understood and well mastered, a wide range of new possibilities opens up. Entire laboratories can be scaled down to the size of a coin, and biomedical therapies become more discrete and can be integrated into people's everyday life.

1.1 Microfluidics

Microfluidic structures include microchannels and microchambers. Typical dimensions of such structures range from a few micrometres to several millimetres: one can find channels smaller than a human hair as well as chambers that are as large as a shirt button. Even when large structures are used, microfluidics deals with very small volumes. As Figure 1.1 illustrates, a cube with a side of 100 μm occupies a volume of 1 nL, whereas a cube with a side of 1 mm has a volume of 1 μL.

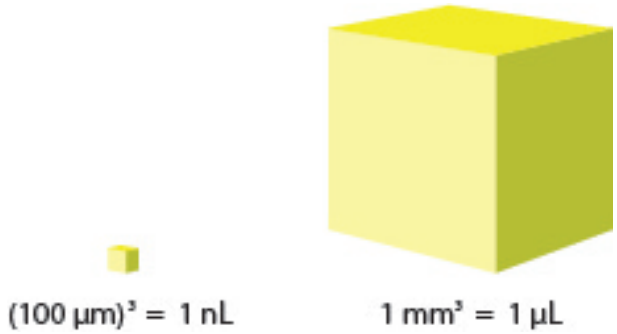

Figure 1.1: Examples of typical dimensions and volumes in microfluidics.

Regardless of the nature of the liquid, the physics involved in experiments with such small volumes will be influenced by the dramatic increase of the surface-to-volume ratio. Let us consider the two cubes in Figure 1.1 again: the surface-to-volume ratio of the large cube is $6 \cdot 10^2$ while it increases to $6 \cdot 10^4$ for the small one.

Surface-to-volume ratio

Increasing the surface-to-volume ratio means increasing the relative importance of surface forces (such as shear stress and surface tension gradients), respect to volume forces (gravity and inertia, for example). The evolution of this ratio is expressed by [1]

$$\frac{\text{surface forces}}{\text{volume forces}} \propto \frac{\ell^2}{\ell^3} \xrightarrow[\ell \to 0]{} \infty, \tag{1.1}$$

and has two main implications: energy and matter exchanges, which take place through surfaces, are sped up, and surface forces overwhelm volume forces.

The first effect allows for faster chemical reactions [2] and eases heat exchange. It is therefore possible to perform complex analyses (e.g. medical or biological) in a shorter time and using a very low amount of analytes and reagents [3, 4], as well as produce complex chemical compounds at a faster rate [5]. Meanwhile, the second effect allows for effective ways of controlling the position and movement of small volumes of liquids. But working on a very small scale does not only mean working with very small physical dimensions.

Reynolds number

On the micro scale, liquid velocities are also strongly reduced. Therefore, the relative importance of inertial forces and viscous forces changes. Their relationship is represented by the Reynolds number [1], which is defined as

$$\mathrm{Re} = \frac{\rho v_0 L_0}{\eta}, \tag{1.2}$$

where v_0 and L_0 are respectively the characteristic fluid velocity and the characteristic length of the system, whereas ρ and η are the liquid density and viscosity.

When $\mathrm{Re} \gg 1$, inertia dominates and gives chaotic flows, such as the stream of a river. When $\mathrm{Re} \ll 1$, viscous forces dominate and give laminar flows, such as the flow of blood in a capillary. Table 1.1 gives examples of typical values encountered in microfluidics and in the macro world: microflows are usually laminar. On one hand, flow laminarity avoids the formation of turbulences and maintains stable interfaces, offering unique functionalities such as the ability to finely control the motion of fluids [6] and use interfaces for sensing purposes [7], and opening the way to new disciplines such as optofluidics [8]. On the other, laminar flows present the main drawback of preventing the mixing of different liquids, which has been the

Table 1.1: Comparison of typical flow parameters and Reynolds numbers in a microfluidic channel and on the macro scale.

	Microfluidic channel	River
ρ	1000 kg/m^3	1000 kg/m^3
η	0.001 $Pa \cdot s$	0.001 $Pa \cdot s$
v_0	100 $\mu m/s$	1 m/s
L_0	100 μm	1 m
Re	1E-2	1E6

motivation for a large amount of research [9, 10].

Microscale phenomena and the possibility of exploiting them to achieve results that are precluded on the macroscale are the reason for the growth of microfluidics in the last decades [1]. Moreover, microfluidics can exploit the established fabrication technologies of microelectronics and microelectromechanical systems (MEMS) and this has allowed for the development of a wide range of devices integrating an increasing number of functionalities on the same chip [11]. Since complete systems were first presented [12], they have been called labs-on-a-chip (LOC) and miniaturised total-analysis-systems (μTAS). They usually include a fluidic net with sites for analyses and reactions, alongside with pumping elements and electronics for data acquisition and control.

1.2 Micropumps

The motion of liquid samples within an integrated chip must be precisely controlled. Operators need to accurately handle very small volumes as well as to generate precise flow-rates. In many cases, a satisfying control of flow-rates is achieved by using bulky external pumps, which are connected to the microfluidic chips [13]. It is clear that, by doing so, the advantage of having compact and mobile systems is lost.

Micropumps address the problem of compactness and portability and can be directly integrated into LOCs and μTASs [14]. They guarantee a fine tuning of the generated flow-rates and pressures, which allows, in turn, control of the rate of chemical reactions and the speed of physical phenomena. Other miniaturised systems may benefit from the use of micropumps: these include fuel cells [15, 16], which should be fed with fuel and where the byproducts of the reaction must be removed, as well as devices that need to be cooled down regularly, where a closed microfluidic circuit can be set up for this purpose [17].

Moreover, micropumps exist as standalone devices. Micropumps have indeed been developed and characterised as independent devices and there are a number of cases where they are used as such. The most important of these examples is drug delivery in biomedical applications

such as insulin therapy. But thanks to the small size and low power consumption, micropumps can also be deployed as external flow control in combination with other integrated microfluidic devices, ensuring the portability of the system.

A wide range of driving principles have been studied and presented in the scientific literature. According to the actuation, we can define two main categories of micropumps: mechanical and valveless. On one hand, mechanical pumps rely on the movement of membranes or other bodies to push the liquid. On the other, valveless pumps usually have no moving component and rely on other kinds of forces, e.g. electrical or magnetic.

1.3 Market needs

Microfluidic devices have long been on the edge of mass industrialisation. Although many products have been developed and are now available on the market, microfluidics has not become a widespread consumer product yet. The difficulties in achieving a high level of reproducibility and reliability, as well as the huge fabrication costs explain this delay [14]. These issues are particularly important when it comes to medical devices.

Most commercially available micropumps are silicon based and drive the motion of the fluid by mechanical actuation. Such devices have several drawbacks: when a MEMS integrates a moving part, its reliability may decrease. First, mechanical moving parts may fail after a certain time, which cannot always be predicted, and possibly cause the failure of the whole device [18]. Second, the flow generated by such pumps is usually intermittent and has a definite volume per stroke, which can hardly be real-time modified. Finally, the fabrication process is carried out on multiple substrates that are bonded together to obtain the final device, which increases the costs.

The possibility to integrate micropumps into implantable drug delivery systems is very attractive, both in terms of benefits for society and potential development for industry [19]. The lack of devices able to generate finely-tuned flows, fabricated with simple yet robust technology, and exploiting a non-mechanical actuation, is a strong motivation to develop a new family of valveless micropumps.

1.4 A valveless micropump for implantable systems

Implantable drug delivery devices are complex systems [20]. As Figure 1.2 shows, these devices must have a biocompatible packaging and they include a pump (the core of the device), alongside a source of energy, flow-rate monitoring and control electronics. The present work focuses on the core pump and will consider the other items of the system only as far as they impose choices on the actuation and design of the pump.

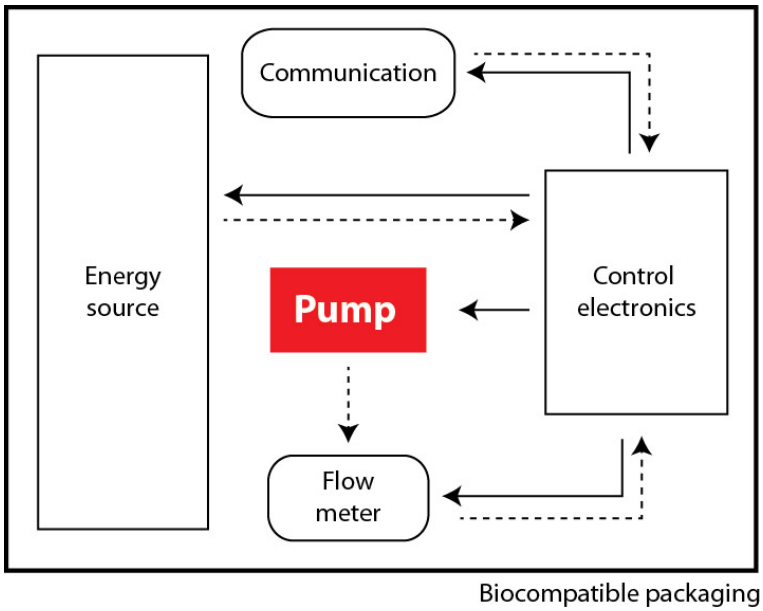

Figure 1.2: Typical composition of a drug delivery system. The energy source supplies power to all the components. The solid lines indicate the control information going from the electronics to the system, while the broken lines indicate the feedback information going from the components to the electronics.

A micropump for implantable drug delivery systems should

- be compact,
- generate no gases,
- have sufficient pressure and flow-rate capability,
- generate low or no heat,
- be made of biocompatible materials,
- be real-time tunable via a feedback loop.

When micropumps are used for the delivery of liquids to the human body, accuracy, resolution, safety and control of the device are of crucial importance [21]. This is one of the reasons why, for several years, there has been increasing interest in investigating alternative solutions allowing liquids to move without exploiting any moving part [18]. Among the existing solutions, electro-osmotic (EO) actuation is probably the most easily implementable, and one allowing the generation of a continuous flow and its control in real time.

This thesis discusses the design, fabrication and characterisation of an electro-osmotic micropump, which exploits AC electric fields to drive the motion of the liquid. AC electro-osmotic

(ACEO) devices are able to effectively generate fluid motion, whilst keeping a low power consumption and avoiding gas generation within the system. The present work shows that depositing ACEO electrodes all around the pumping channel allows for a dramatic increase in the generated velocity and pressure capability.

Chapter 2 will summarise the state of the art of both academic and industrial microfabricated pumps, with a particular focus on electro-osmosis. Based on the experimental results of previous studies, we will motivate the choice of AC electro-osmosis as the actuation principle for our micropump.

Chapter 3 will present the theory of electro-osmosis and the electrical and hydraulic models, which will be used in the following to study and characterise the fabricated devices. The final part will be dedicated to geometrical considerations and the theoretical basis for this specific work.

Chapter 4 will list the experimental approaches to the preparation of the samples, and of the electrical and fluidic setups that were used to characterise our pumps. The algorithms to extract the relevant information from the experimental data will also be described.

Chapter 5 will present the fabrication and characterisation of improved ACEO pumps with electrodes on two sides of the channel. This will prove, with experiments, that our design approach is correct. The comparison between different materials for the electrodes will also be discussed.

Chapter 6 will show that channels with electrodes on all sides can be fabricated with few lithographic steps and that the ACEO pumps that are made in this way are able to generate very large fluid velocities.

Chapter 7 will discuss the possibility of realising the same improved design with polymers and alternative, low-cost fabrication methods. Very thin plastic substrates and ink-jet printing of conducting polymers will be considered as alternatives to standard cleanroom fabrication.

Chapter 8 will summarise the findings of this research and give an outlook on the future of ACEO pumping.

2 State of the Art

Analysing the work that other researchers have previously carried out means learning about the possibilities and the challenges that a subject offers. Micropumps have been studied for several decades and the actuation principles that have been implemented cover a very wide range of physical effects, based on very different laws. Going through the state of the art of micropumps is like a trip across the different domains of physics.

2.1 Comparing pumps

Early examples of devices able to pump micro volumes date back to 1954 [22], even though fully integrated systems only appeared in 1978 [23] and micropumps exploiting microfabrication technologies were first presented only in 1988 [24]. Since then, many devices have been implemented and described in the scientific literature[25, 26, 27]. This chapter presents an overview of the different actuation principles that have been studied and of the devices that have been fabricated.

After a brief summary of mechanical actuation, the review will focus on non-mechanical devices and, in particular, on electro-osmotic pumps. The goal is to understand the advantages and disadvantages of each approach, and to decide which is the most appropriate to be included in an implantable pump. We shall see that AC electro-osmosis is the physical effect that we are interested in, since it avoids gas generation, consumes little power and can be implemented through a simple fabrication process.

In order to be able to compare the devices that will be presented, let us preliminarily define some parameters to describe the pumping performance: the generated flow-rate Q, the backpressure capability Δp, and the power consumption W_{el} and conversion efficiency η_{conv}.

Flow-rate

Volumetric flow-rate is defined as the fluid volume discharged by a channel per unit of time [1]. If the geometry of the channel and the velocity of the fluid are known, it can be computed as

$$Q = v_{ave} \cdot S, \tag{2.1}$$

where v_{ave} is the mean fluid velocity and S the cross-section of the channel. A good micropump can cover a wide range of flow-rates, whilst having a fine and precise control on the generated value.

Backpressure

Any pressure gradient present across a pump and which opposes the flow induced by the device, is called a backpressure. The pressure capability of a pump is the backpressure needed to completely cancel the generated flow [1]. This value should be as large as possible, in order to be able to operate the pump in high-pressure environments. Figure 2.1 shows the typical characteristic obtained when the flow-rate is plotted versus the external pressure. In the literature, backpressure is also called pump head, differential pressure or head pressure [28].

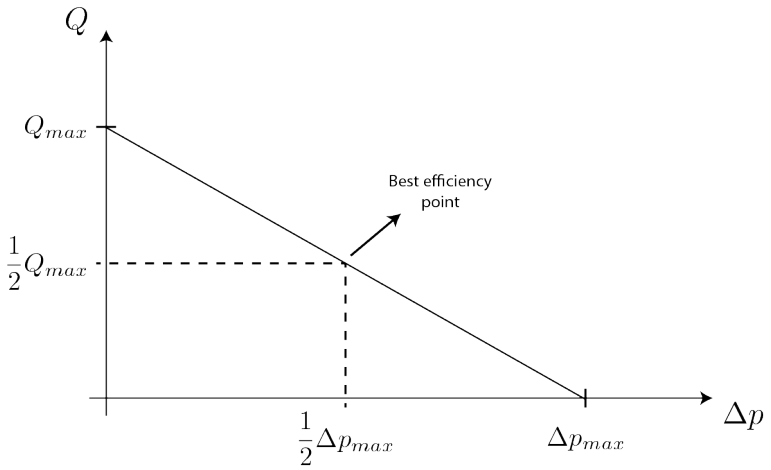

Figure 2.1: Usual fluidic characteristics of a pump. The flow-rate is plotted versus the external pressure. The maximum pressure capability ΔP_{max} as well as the maximum flow-rate Q_{max} are indicated. The pump exhibits the best efficiency at the working point $(0.5Q_{max}; 0.5\Delta p_{max})$.

The flow-rate and pressure in microchannels, and in a low-Reynolds-number regime, are related by the expression [1]

$$\Delta p = R_{hyd} \cdot Q, \tag{2.2}$$

where R_{hyd} is a quantity called hydraulic resistance, whose value depends on the geometry of

the device as well as on the properties of the liquid filling it. A closed formula for R_{hyd} can only be found for very simple geometries, such as circular, square and rectangular channels, while in the other cases the value can only be approximated [1].

Power consumption

Most micropumps exploit electrical energy. When the applied voltage V and the current flow I are known, the power that is dissipated in a pump can easily be computed, as

$$W_{el} = V \cdot I. \tag{2.3}$$

Interest in power consumption and efficiency arises from three main considerations. First, a limited power consumption is required for the proper integration of the pump in systems where a too large heat generation could be critical to the correct functioning of the device. Moreover, when the pump is implemented in an implantable device, excessive heat generation may harm the patient. Second, power consumption determines the size of the batteries and the frequency at which they should be replaced, which may affect the portability of the device and means additional costs for the end user. Third, it might be interesting to replace traditional power supplies with energy scavengers [29]; in this case, low power consumption is a fundamental condition to be able to exploit energy-harvesting strategies.

Thermodynamic efficiency

The thermodynamic efficiency represents the ability of the pump to convert electric power into hydraulic power [30, 31]. For given working conditions, it is given by the ratio of the maximum generated hydraulic power W_{hyd} to the consumed electric power W_{el} and can be computed from the values of the maximum generated flow-rate and pressure[26] as

$$\eta_{conv} = \frac{W_{hyd}}{W_{el}} = 0.25 \frac{Q_{max} \Delta p_{max}}{V \cdot I}, \tag{2.4}$$

where the point $(0.5Q_{max}; 0.5\Delta p_{max})$ on the graph in Figure 2.1 is the maximum efficiency point.

2.2 Mechanical micropumps

Mechanical (or reciprocating) actuation was the first to be implemented in microfabricated pumps [24] and the one that has been reported most often in the literature [26]. The design presented by van Lintel *et al.* in 1988 already included most of the features of present mechanical pumps.

Common features

The actuation principle common to all pumps in this family is that the liquid is pushed by the periodic motion of a deformable membrane, or diaphragm. Because a periodic actuation generates a bidirectional flow, these pumps are usually fabricated alongside a system of rectifying valves. Therefore, mechanical pumps share a common basic structure, which is illustrated in Figure 2.2: a pump chamber with a diaphragm on one side, bound to the actuator mechanism, and with valves at the inlet and outlet [26].

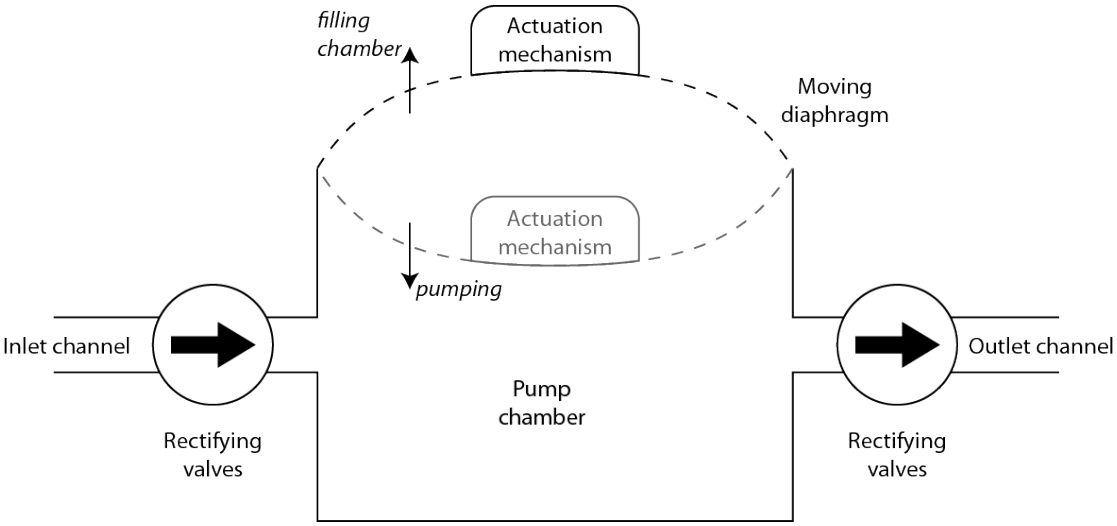

Figure 2.2: Typical structure of most mechanical pumps. It includes a pump chamber actuated by a diaphragm and valves to rectify the flow.

During operation, the active membrane sets the fluid in motion by alternately increasing and decreasing the volume of the pumping chamber. Thus, liquid is sucked in and pushed out of the chamber over a two-stroke cycle, while the valves favour the movement of the liquid from the inlet to the outlet, and rectify the generated flow. Some devices include more than one chamber [32] and pump fluids through a peristaltic actuation of the membrane in each chamber. Thanks to the use of valves and membranes that can hermetically close the channel, mechanical pumps can usually avoid backward flows due to high backpressures [26]. Flow rates as large as 33 mL/min and pressures as high as 920 kPa have been reported in the scientific literature [27].

Reciprocating pumps are usually fabricated on several substrates (silicon, glass or plastics) that are finally bonded together. Examples in the literature include devices obtained by bonding together from as little as two [33] to as many as seven separate substrates [28] to obtain the final device. According to the physics used to actuate the pump membrane, we can list piezoelectric, electrostatic, magnetic, thermopneumatic and pneumatic pumps.

Actuation mechanisms

Piezoelectric materials undergo a lateral and an axial strain upon the application of an electric field. Both lateral [24] and axial [34] strains have been used to deform the pumping diaphragm in microfabricated devices. Typical actuation signals have a frequency of up to several kHz and a magnitude in the order of a few kV [26].

Electrostatic actuation has the advantage of being easier to implement, in the form of a parallel-plate capacitor having one of the two plates bounded to the pumping membrane. As a sequence of positive and negative voltages is applied across the capacitor, the diaphragm is lifted up and down and pumps the fluid. Typical actuation signals have frequencies of several hundred Hz and magnitudes of several hundred V [35].

A similar approach is to actuate the membrane by applying a magnetic force. In this case, ferromagnetic elements should be embedded in the membrane and actuated by an external field [36], provided by a permanent magnet or an electromagnet. Due to their structure, magnetically actuated pumps are not compact. They can be quite bulky and may consume as much as 2 W [37], inducing considerable heat generation [38].

One last example of actuation are pneumatic and thermopneumatic pumps. Such devices exploit the controlled expansion and contraction of an air volume to induce the motion of the liquid. While pneumatic actuation relies on an external source of pressure [39] to deform the pumping membrane, thermopneumatic pumps include micro heaters, which are turned on to make air expand, and off to let it rectract, thus actuating the pumping membrane [17, 40]. A simpler and valveless example of thermopneumatic actuation was used to draw liquid samples into a microchannel [41] and eject them [42], whereby the heating elements were in contact with the air in the channel. Because of the large temperature changes (in the order of 50 $^{\circ}C$ [42]), thermopneumatic pumps are obviously unfit to be integrated in implantable medical devices.

Examples of commercial devices

Many micropumps exploiting mechanical actuation have been developed and commercialised on the market. Among these, the MIP pump series [43] by Debiotech SA (Lausanne, Switzerland) is based on standard cleanroom fabrication and generate liquid motion through piezoelectric actuation. In order to generate flow in a constant direction, the system is coupled with integrated valves and has been successfully implemented in biomedical devices. The MIP pumps generate minimum strokes of 150 nL and are actuated with potentials of 110 V and frequency of a few Hz. The company has also set up a partnership with ST Microelectronics (Crolles, France) for the development of a new series of products called *Nanopumps* and based on SOI-wafer technology [44].

The market also offers access to lower-cost devices. A good example is provided by the *Micro Pump* series by Bartels Mikrotechnik GmbH [45]. Their devices are realised by injection

moulding and are made almost completely of plastics. The actuation is based on piezoelectric materials and the pump is provided with rectifying valves. Using actuation potentials of up to 250 V and frequencies between 100 Hz and 300 Hz, the *mp6* device can pump liquids and gases and generate flow-rates of up to 6 mL/min and pressures as large as 55 kPa. The *mp5* micropump was used by Yuen to implement modular microfluidic systems [46].

Drawbacks of mechanical pumps

Mechanical pumps all exhibit behaviours connected to their actuation mechanism, which make them less suitable for long-term use in implantable biomedical systems. Using high voltages may result in serious harm to the patient, and the presence of moving valves affects the long-term reliability of the devices. In fact, moving components are continuously actuated and subjected to mechanical stress, which may result in rupture during operation.

Moreover, some pumping mechanisms rely on strong heat generation. Mechanical pumps may also require external elements, such as permanent magnets, and they are mostly fabricated by bonding together a stack of two or more structured substrates, which makes them costlier and potentially less reliable. Valveless pumps avoid many of the issues that their mechanical counterparts have by eliminating the moving components.

2.3 Valveless micropumps

Thanks to the exploitation of other kinds of forces, fluid flow in non-mechanical pumps is generated without the need for moving parts. The device usually includes one or more microchannels and a system of electrodes that control the generation of the pumping force. Therefore, this family of pumps are often simpler to fabricate and more resistant to mechanical stress, thus avoiding the drawbacks of mechanical devices. Physical effects that can drive a fluid flow are capillary and contact angle forces, surface acoustic waves as well as electric, magnetic and electromagnetic forces.

2.3.1 Capillary micropumps

Capillary forces arise from the difference between the surface tension of the liquid-air and the solid-air interface in a capillary channel. The pressure generated by such forces is expressed by

$$\Delta p_{\text{capillary}} = \frac{2(\gamma_{sa} - \gamma_{sl})}{d}, \tag{2.5}$$

where d is the smallest dimension of the channel, γ_{sa} is the surface tension at the solid-air interface, and γ_{sl} the one at the solid-liquid interface. Exploiting the capillary forces, it is possible to fill microchannels simply by putting the inlet in contact with the liquid reservoir.

If the channel is vertical, the liquid will rise up to the height where the capillary pressure is balanced by the hydrostatic pressure $\Delta p_{hyd} = \rho g h$, which builds up because of gravity. If the channel is placed horizontally, the force given by surface tension will not be balanced by gravity, and liquid motion will continue until the end of the capillary. A schematic representation of capillary actuation is given in Figure 2.3.

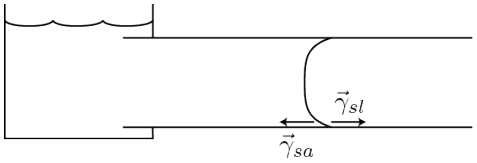

$$\Delta p = \frac{2(\gamma_{sa} - \gamma_{sl})}{d}$$

(a)

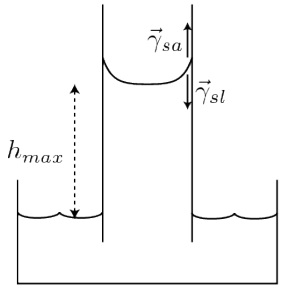

$$\Delta p = \frac{2(\gamma_{sa} - \gamma_{sl})}{d} - \rho g h$$

(b)

Figure 2.3: Schematic view of a micro channel being filled by a liquid thanks to the capillary force. The location and directions of the surface tension forces are indicated. Capillary forces can completely fill horizontal channels (a), whereas in vertical channels the maximum height is limited by gravity (b).

While capillary actuation has the major advantage of consuming no power, its effectiveness is limited to the length of the channel. Once the capillary has been completely filled by the liquid and the air-liquid-solid interface is no longer present, the capillary force will become zero and the pumping cease. Nevertheless, there are several examples in the literature, where capillary pumps were successfully used to move liquids, for example on chips for blood analysis [47].

2.3.2 Electrowetting

Liquids can also be pumped as individual droplets [48]. An effective way of doing this is by making the droplets move by using electric fields to locally change the wetting behaviour of a solid surface. A phenomenon called electrocapillarity and the physics at its basis was first described at the end of the nineteenth century [49] for liquids in contact with metal surfaces.

Since the application of a DC voltage between an electrolyte and a metal can induce electrolysis and generate gases, in order to avoid this problem, the most recent applications of this

technique separate the liquid droplets from the electrodes with a thin layer of insulating material. Electrowetting is therefore usually referred to as electrowetting on dieletrics (EWOD). The basic equation for EWOD, defining how the contact angle changes upon the application of an electric field is [49]

$$\cos\theta = \cos\theta_Y + \frac{\epsilon}{2d\gamma_{la}} V_0^2, \tag{2.6}$$

where θ and θ_Y are respectively the final contact angle and the contact angle at zero applied voltage, d the thickness of the insulating layer, and γ_{la} the surface tension between liquid and gas. The application of the potential V_0 between a liquid droplet and the substrate decreases the contact angle and induces a disequilibrium of the pressure within the droplet, which starts moving in the direction of the applied voltage [50], as Figure 2.4 illustrates.

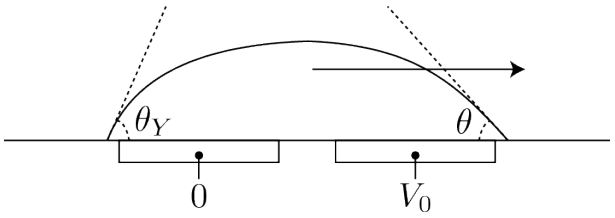

Figure 2.4: Basic implementation of the electrowetting principle. A voltage applied only on one side of the droplet locally changes the contact angle and can set the liquid in motion.

Typical velocities can be as large as 100 mm/s [49], however, as for capillary forces, electrowetting requires the existence of a solid-liquid-gas interface to be effective, which is not the case for applications where the pump should operate in a closed environment and free of gas. Nevertheless, EWOD techniques have been successfully applied to a range of applications including micro-scale mixing [51], micro-lenses [52], displays [53] and, more generally, to the domain of digital microfluidics [54].

2.3.3 Acoustic wave micropumps

An alternative way of moving liquid droplets is to use surface acoustic waves (SAWs). In this case the channel, or the surface onto which the droplets should be moved, must be covered by a layer of piezoelectric material. Interdigitated electrodes must be patterned in contact with the piezoelectric layer and are used to excite its vibrational modes.

The fast-alternating electric field applied by the electrodes generates nanometer scale displacements on the piezoelectric surface [55]. SAWs are these mechanical waves that travel in a region within a few wavelengths from the surface of the material. The momentum and energy that they transport are partially transferred to the bodies encountered on their path, such as liquid droplets [56]. When this coupling of momentums takes place, the acoustic wave induces a local change of the contact angle of the droplet, which in turn represents a non-zero acoustic force within the liquid. According to the magnitude of the acoustic force, relative to

the surface tensions of the involved materials, the liquid can either have a stationary motion that induces mixing ($F_{SAW} < F_{surface}$), or develop a translational motion and be pumped ($F_{SAW} > F_{surface}$), or be sprayed off the surface (($F_{SAW} \gg F_{surface}$).

When the magnitude of the acoustic force is in the range adapted to move the droplets, it will be related to the advancing and receding contact angles by [18]

$$F_{SAW} = 2R\gamma_{la} \sin \frac{\theta_a + \theta_r}{2} (\cos\theta_a - \cos\theta_r), \tag{2.7}$$

where R is the radius of the droplet, γ_{la} the surface tension of the liquid-air couple, and θ_a and θ_r the advancing and receding contact angles respectively. This effect is more efficient on hydrophobic surfaces; however, in typical implementations of acoustic pumping, a voltage larger than 35 V is sufficient to overcome surface tension forces and set the droplets in motion, even on hydrophilic surfaces [18].

Acoustic pumping exploiting $LiNbO_3$ as a piezoelectric layer has been used to fill channels at an average velocity of 50 $\mu m/s$ [57]. The same piezoelectric material has also been used in other applications and was able to generate liquid velocities within the droplets as high as 18 cm/s [58]. Similar performances were also observed with $LiTaO_3$ piezoelectric layers [59]. Because such kinds of piezoelectric materials are quite bulky and cannot be integrated with electronics, thin layers of ZnO deposited on Si substrates have recently been used for SAW micropumps [58] and were able to generate velocities of about 5 cm/s.

Some groups have also been able to use the transfer of kinetic energy from the acoustic wave to the liquid bulk to induce a continuous liquid motion in a closed channel, with generated velocities close to 1 mm/s [60]. Nevertheless, surface acoustic waves do not yet appear as a reliable means to pump liquids in an implantable device. In fact, many implementations are designed to exploit the very high velocity that is locally generated within a droplet to obtain micromixing. Among the examples of translational pumping of a liquid, most rely on an external piezoelectric element or require the presence of a solid-liquid-air interface to be able to make single droplets move. On the other hand, the technology to integrate thin piezoelectric layers in silicon-based microfluidic devices seems costly and unreliable.

2.3.4 Electromagnetic micropumps

The operation of the valveless pumps that we have introduced so far is restricted to the finite time required to fill a capillary, or to the discrete pumping of isolated quantities. But electric and magnetic fields also allow for shape-independent and continuous pumping. One possibility is to induce a pumping force in the bulk of the liquid. According to the specific actuation principle, we can distinguish magnetohydrodynamic (MHD) and electrohydrodynamic (EHD) pumps.

Magnetohydrodynamic pumps

Whereas direct actuation of a ferromagnetic fluid is possible by moving an external magnet close to the channel [61], magnetohydrodynamic pumping is based on the Lorentz force and allows the actuation of non-magnetic liquids. When an electric current flows perpendicular to a magnetic field, a force arises which is orthogonal to both the current and the magnetic field. The principle is illustrated in Figure 2.5 and the Lorentz force density is described by

$$\vec{F} = \vec{J} \times \vec{B}, \tag{2.8}$$

where $\vec{J}$ is the current density and $\vec{B}$ the magnetic field. MHD pumps usually couple a microfluidic system, in which an electric current flows perpendicular to the pumping channel, with an external magnetic field. The Lorentz force then pulls the moving charges in the desired direction and the bulk of the liquid follows by viscosity. MHD pumping may also be performed with AC signals [62]; provided that the alternating current and magnetic field are synchronous, the generated force will always have the same direction and its magnitude will be defined by

$$F = IBw \int_0^{2\pi} \sin\omega t \sin[(\omega+\phi)t]\mathrm{d}(\omega t), \tag{2.9}$$

where I is the current flowing across the channel, B the magnitude of the magnetic field, and ω and ϕ are respectively the angular frequency and mutual phase of I and B. In this case, controlling the phase of the signals allows for the control of both the intensity and direction of the generated flow.

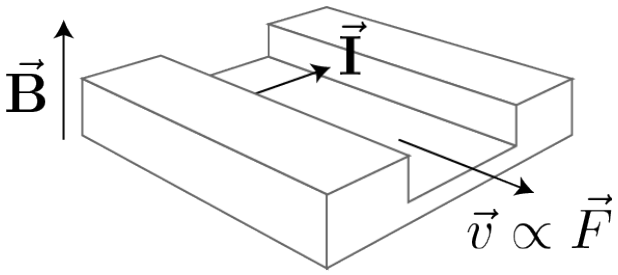

Figure 2.5: Schematic view of the magnetohydrodynamic force building up in the presence of an electric current $\vec{\mathbf{I}}$ crossing the channel and a magnetic field $\vec{\mathbf{B}}$ orthogonal to both. The velocity is generated in the third direction, along the channel.

Liquid metals and electrolyte solutions have been pumped by MHD. The former having a conductivity that is more than five orders of magnitude higher than the latter, they can usually be pumped much more efficiently [63]. Such an approach to generating the motion of a liquid has many advantages. The generated flow is continuous and can be finely tuned by controlling the intensity of the current and the magnetic field. Since the magnetic force is applied to the whole bulk of the liquid, MHD pumps can also stand high backpressures. Nevertheless, permanent magnets can hardly be integrated on a microfluidic chip, which prevents the system from being compact, and the required current levels and magnetic fields may be

quite large, which makes this actuation unsuitable for medical applications. Moreover, the operation of DC magnetohydrodynamic pumps also induces electrolysis and gas generation in the solution.

Microfabricated DC MHD pumps were first presented by Jang *et al.*, who were able to generate flow velocities as large as 2.6 mm/s with their devices [64]. There has also been a huge interest in employing MHD pumps in nuclear-magnetic-resonance (NMR) environments [65]. The presence of strong magnetic fields in the working environment of the pump eases the implementation of the device, which does not need to integrate permanent magnets. Pumps actuated under an NMR field of 7 T were able to generate fluid velocities of up to 2.8 mm/s [66].

AC MHD micropumps were introduced at the same time as DC-operated devices and exploit electromagnets to produce the required magnetic fields [62]. This kind of device has been successfully exploited in many applications, such as microchips for chromatography, where fluid velocities of 40 $\mu m/s$ were measured [67], or polymerase-chain-reaction (PCR) chips for the propagation of DNA, where up to 340 $\mu m/s$ could be generated [68].

Electrohydrodynamic micropumps

Electrohydrodynamic pumps are based on the injection, or induction, of free charges in the bulk of a dielectric liquid [69, 70]. An electric field is applied to these charges in the desired pumping direction. The resulting electric force pulls the charges, and the liquid bulk is dragged by viscous forces. Different kinds of EHD pumps can be defined, according to the strategy used to create the free charges in the fluid [27]. The force acting on the charges in EHD pumps is more generally described by [27]

$$F_{EHD} = \rho_{el}E + P\nabla E - \frac{1}{2}E^2\nabla E + \nabla(\frac{1}{2}\rho\frac{\partial\epsilon}{\partial\rho}E^2), \tag{2.10}$$

where P is the polarisation vector, ρ_{el} the net charge density in the bulk of the liquid, ϵ the electric permittivity and ρ the density of the fluid. Figure 2.6 illustrates the general principle of EHD actuation.

In **induction pumps**, the pumping force is induced by creating a gradient in the permittivity or the conductivity of the liquid. Such a gradient can usually be obtained by either heating the fluid bulk in a non-uniform way, or imposing a material discontinuity, e.g. by filling a channel with two non-mixing liquids. Once a non-zero charge density is obtained in the regions of the channel where the gradients occur, these particles can be set in motion by the application of an electric field in the form of a travelling wave. The direction of pumping will depend on the properties of the wave as well as on the density of charges. Induction pumping has traditionally been used with very-low-conductivity liquids (10^{-14}-10^{-9} S/m) [27]. Only more recently, an EHD device was reported, which was able to generate velocities as high as 80 $\mu m/s$ in a liquid having a conductivity of 140 $\mu S/cm$, which roughly corresponds to an electrolyte

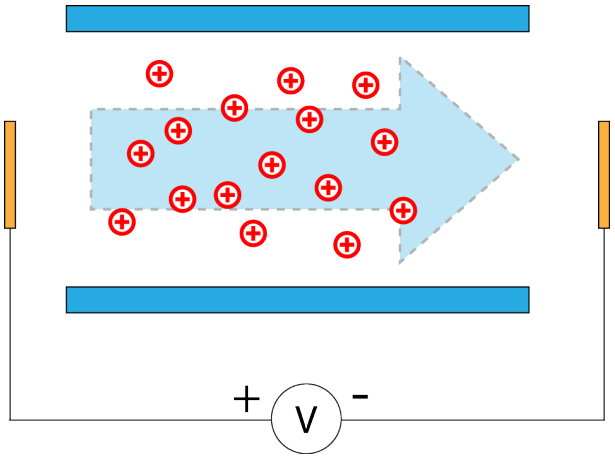

Figure 2.6: General principle of EHD actuation. First, free charges must be created in the bulk of the liquid, then an external electric field makes them move and sets the whole liquid in motion. The generated velocity will be proportional to the EHD force acting on the fluid.

concentration of 1 mM [71].

A different way of creating a non-zero charge density in the liquid is to inject charges. **Injection pumps** create free charged particles through electrochemical reactions, which inject ions into the liquid. Again, this kind of pump works best in very poor conductors and non-polar liquids [27]. A recent study demonstrated the use of an EHD pump in cryogenic cooling systems, in which pressures as large as 600 Pa could be generated [72]. Injection pumps are one of the rare valveless actuation principles that have also been able to pump air [73].

Finally, **Polarisation pumps** introduce a non-uniformity in the electric field density, which causes a gradient in the energy of dipoles in the liquid. Therefore, the dipoles are attracted from regions with high energy to regions with low energy and set the entire fluid bulk in motion by viscous drag [74].

Whereas electromagnetic pumps are very effective at pumping certain kinds of fluids, they still lack the reliability and compatibility that are required for applications with biomedical fluids and/or in closed environments. In fact, too large magnetic and electric fields are used and electrolysis occurs in many cases. Some EHD pumps rely on the modification of the chemical nature of the liquid, which clearly makes them incompatible with a medical use.

2.4 Electro-osmotic micropumps

Electro-osmosis is an approach to pumping fluids, which produces less chemical changes in the pumped liquid than magnetohydrodynamics and electrohydrodynamics, since it does not require any modification of the nature of the liquid. Every time an insulating solid comes into contact with a liquid, it develops a non-zero charge density at its surface, which induces an electrical potential next to the solid wall. In order to mask such potential, opposite-charge

ions present in the liquid accumulate in front of the solid surface and give rise to a double layer of charges. The same phenomenon can also be induced by applying a voltage between a conducting surface and the liquid.

Charged layers formed in such ways can be set in motion by an external electric field and drag the bulk of the liquid by viscous forces. This principle is at the basis of electro-osmotic (EO) pumping. EO devices have been used with a wide variety of working fluids and can be easily integrated, thanks to their small dimensions and the fact that they do not need any external components like, for example, large magnets.

This section will focus on the existing literature on EO pumping and will compare the performances that have been reported until present. Chapter 3 will approach the theoretical aspects of electro-osmosis and, drawing on theoretical considerations, formulate simple design rules and suggestions to improve the performance of the devices.

Two main families of electro-osmotic micropumps have been studied and reported, according to whether the applied potential is continuous or alternative. DC electro-osmotic (DCEO) pumps, whose actuation principle is shown in Figure 2.7, were the first to be implemented for electrophoresis [75] and on-chip chromatography [76]. Some years later, devices actuated with AC signals (ACEO) [77] and travelling-wave potentials (TWEO) [78] were presented, of which Figure 2.8 illustrates the actuation principle. In this section, we present a selection of representative EO micropumps that have been fabricated and tested since 2001. For each device under consideration, we report the maximum achieved flow-rate and backpressure, as well as the parameters of the actuating potential. The review will also highlight any specific or peculiar characteristics of the presented pumps.

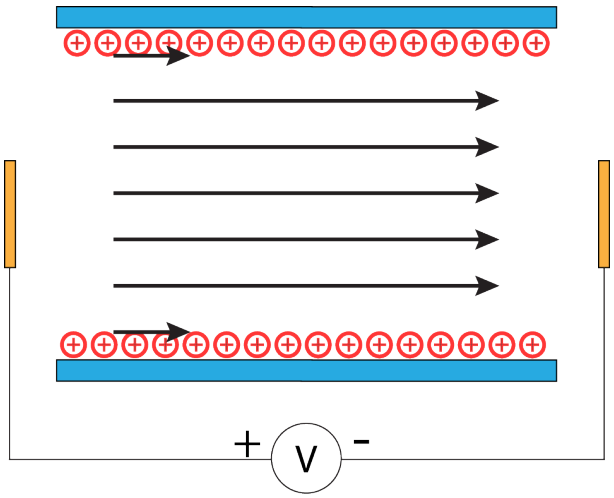

Figure 2.7: Actuation principle of DC electro-osmosis. A layer with non-zero charge density builds up next to the walls and is set in motion by an external electric field, dragging the bulk of the fluid. The generated velocity is proportional to the product of the charge density in the EDL and the applied electric field.

2.4.1 DC electro-osmotic pumps

A common characteristic of EO pumps is that the pumping force arises in the electric double-layer, which is much thinner than the channel diameter. Therefore, the velocity generation does not depend on the hydraulic resistance of the system. This applies specially to DCEO devices, which can be easily improved: a parallel connection of many channels having high hydraulic resistance will allow the pump to stand larger backpressures, while the generated velocity within the channels will remain constant and the overall flow-rate will be given by the sum of the flow-rates in the single channels [1].

DC electro-osmotic pumps also share a major drawback. Because the applied potential is continuous and metal electrodes are usually in direct contact with the liquid, electrochemical reactions involving water and the species in solution may occur. Electrolysis of water is commonly observed and induces the formation of bubbles of hydrogen, oxygen or other gases, which can impede the flow of the liquid by occupying the whole cross-section of the pumping channel, and modify the chemical properties of the solution (e.g. pH).

Innovation of DCEO pumps

Aiming at a chemical separation between the liquid in contact with the electrodes and the one that should be pumped, Guenat *et al.* developed a pump, which was able to produce a constant flow-rate of 984 nL/min at an applied voltage of 750 V [79, 80]. The equivalent pressure generated by the pump, which can be deduced from the geometry of the device, was about 490 Pa. The device was integrated in a microsystem for volumetric nanotitrations and was able to avoid electrolytic reactions in the liquid of interest. Moreover, the behaviour of the pump was independent of the fluid, except for the viscosity.

With a more traditional design, including a wide and thin channel, etched in a glass substrate, with stainless steel electrodes and interconnects, the micropump developed by Chen and Santiago was able to produce a maximum pressure of 140 kPa and a flow-rate of 2.5 $\mu L/min$ for an applied voltage of 3 kV [30].

Exploiting the principle that splitting the pumping channel into several smaller ones with higher resistance will improve the pressure capability while keeping the flow-rate constant, Zeng *et al.* fabricated a high pressure DCEO pump. A structure similar to many parallel channels was realised by packing a silica capillary with 3.5-μm-wide beads [81]. The device was capable of standing backpressures of up to 2.3 MPa and, at its most efficient, could generate about 1 MPa while maintaining a flow-rate of 2.5 $\mu L/min$, at an applied voltage of 2 kV.

Packed capillaries were also chosen by Chen *et al.* to develop a multi-stage pump [82]. Their devices exploited a sequence of wider and smaller channels to achieve a maximum pressure capability of 10 MPa and flow-rates of about 1.7 $\mu L/min$ for applied potentials in the order of 5 kV. An evolution of this device was constituted by a capillary channel packed with

nanosilica particles [83] and was able to generate pressures as large as 24 MPa and flow-rates of 1.5 $\mu L/min$ at 4 kV.

Unlike the previous examples, Razunguzwa *et al.* realised a fritless pump [84]. Based on two parallel pumping channels with opposite zeta-potential, each containing cation- (respectively anion-) exchange beads, this device had the advantage of reducing the dependence of velocity generation on the pH of the solution to pump. It exhibited a maximum flow-rate of 2 $\mu L/min$ for an applied potential of 3 kV.

Low-voltage DCEO

Many groups have dealt with the issue of the very large voltage required by DC electro-osmosis, and many approaches allowing pumping at low potentials have been reported. Among these, a DCEO pump was developed by Takamura *et al.*, which gave a maximum pressure of 1.73 kPa and a flow-rate of 415 nL/min at an applied potential as small as 10 V [85]. This very good result was achieved by implementing a folded structure and reducing the distance between the electrodes to less than a millimeter. The pump was fabricated in a glass substrate, and exploited $Ag/AgCl$ and gel electrodes. The presence of a salt bridge could guarantee bubble-free operation, while high pressure capability was assured by implementing a multi-stage structure realised by replicating the basic sequence of positive electrode, wide channel, negative electrode, small channel.

An alternative approach to reducing the required voltage levels is to exploit inorganic porous membranes made of silica and alumina. Thanks to its reduced thickness, this kind of structure allows small potentials to induce large electric fields. At the same time, large hydraulic resistances due to the very small size of the pores guarantee a high pressure capability. Examples of such devices have been presented by Prakash *et al.*, who fabricated single-stage and multi-stage pumps able to generate pressures of up to 1.6 MPa and flow-rates of 170 $\mu L/min$ at an applied potential of 370 V [86]. Relying on a similar principle, Vajandar *et al.* realised pumps based on SiO_2-coated porous alumina membranes [87], which could generate a maximum flow-rate of 142.5 $\mu L/min$ when 40 V were applied between the electrodes.

A micropump revolution

Even though large pressures and flow-rates can easily be generated by DCEO, most micropumps still do not directly communicate with the other elements of the system. The ability to receive feedback and adapt the pumping real-time would be extremely useful, specially in biomedical applications, and would represent a real breakthrough.

One step in this direction was made by Seibel *et al.*, who reported a programmable planar DCEO pump, implemented in a closed loop with a mass flow sensor [88]. The device was powered with a potential of only 40 V, but could generate maximum pressures of only 65 Pa and flow-rates of 10 nL/min. The pump was fabricated in a glass substrate, using rib structures

made of SU-8 to guarantee a higher pressure capability by realising a parallel configuration of narrow channels. Moreover, the fabrication process was compatible with CMOS post-processing technology.

Since the first DCEO micropumps were implemented, the scientific community has made significant advances in and improvements to this strategy of pumping liquids. Nowadays, it is possible to perform DCEO with relatively low voltages and strategies have been developed to pump a wide range of liquids with different properties. Nevertheless, there remain problems such as electrolysis and gas generation which are more difficult to overcome. A solution might come from a recent work by Erlandsson *et al.*, who used PEDOT:PSS electrodes to generate DCEO flows with voltages as large as 100 V without observing electrolysis [89]. We will investigate one possible approach to integrating such electrodes in microfabricated systems in Chapter 7.

2.4.2 AC and TW electro-osmotic pumps

Electrolytic reactions can be reverted, to a certain extent, by inversing the polarity of the applied voltages. In fact, using an AC potential to power a pump designed for DCEO will eliminate the effects of electrolysis, as long as the products of the reaction remain close to the electrodes and the counter-reaction is fast enough to consume them completely. But this will also have the effect of bringing the net generated flow-rate to zero, unless some flow rectification [90] or asymmetry of the generated force is introduced.

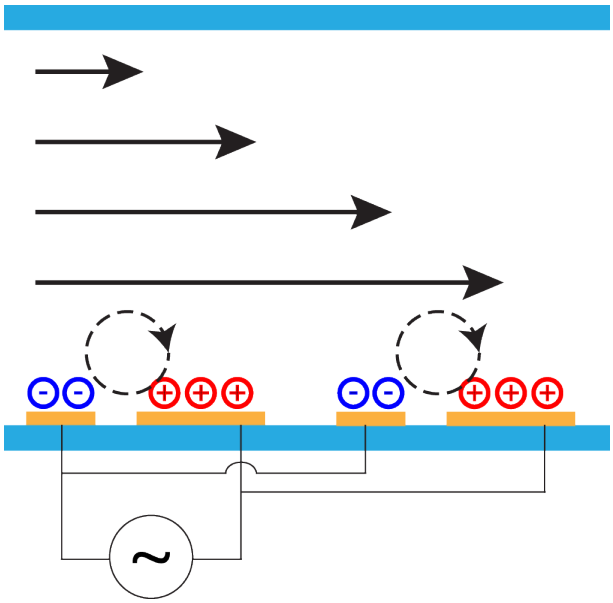

Figure 2.8: Velocity generation in AC electro-osmotic devices. The charge layers are induced by the same applied field that sets them in motion. The liquid is pumped from the small towards the large electrodes and the generated velocity is proportional to the square of the applied potential.

Innovative pump and electrode designs allow alternative voltages to generate non-zero flow-rates. AC and travelling-wave (TW) electro-osmotic micropumps started being developed after the observation that an alternating potential applied to a pair of planar electrodes in contact with a liquid could cause the latter to move [77, 91]. We shall see that this approach to pumping has some limitations. However, it does avoid electrolysis and gas generation, and requires much smaller electrical potentials.

Powering DC pumps with AC voltages

Among the first EO pumps exploiting AC potentials to be realised, we should mention the design suggested by Mutlu *et al.*, who used the fact that under certain conditions liquids have non-linear responses to the injection of an electric current [92]. In fact, they powered their pump with an AC current having zero time-average but different positive and negative values, and an asymmetric duty cycle. The voltage response of the liquid was non-linear and resulted in an electric field (and force) with a non-zero time-average. For injected currents smaller than 1 μA and voltage responses smaller than 5 V oscillating at 2 Hz with 30% duty-cycle, the device was able to pump DI water at up to 14 $\mu m/s$.

Geometry can also offer ways of providing the system with some asymmetry. Brask *et al.* presented a pump with Pd electrodes, coupled to a system of rectifying valves, connected in a sort of hydraulic Wheatstone bridge [93]. Having a design similar to DCEO devices, this pump required the application of a square wave of 60 V_{pp} with a period of 40 s to generate liquid motion. Thanks to the valve system, they were able to generate a maximum flow-rate of 5 $\mu L/min$ and pressures as high as 50 kPa, while avoiding the generation of gas bubbles.

Novel micropumps presented by van der Wouden *et al.* provide the asymmetry necessary to generate a net flow through a synchronous control of the zeta potential and the potential applied across the channel [94]. These two potentials are set by synchronous AC signals and their coupling allows the generation of a net flow in the channel. With an applied signal of 220 V and 1 kHz, the devices were able to generate flow-rates of 2.4 nL/min.

Examples of commercial electro-osmotic pumps also exploit a design with the electrodes at the two ends of the channel, and generate the motion of the liquid by applying AC voltages in order to avoid electrolysis. The devices developed by Mishchuk *et al.* [95, 96] have been industrialised by Osmotex SA (Alpnach, Switzerland) and can generate flow-rates ranging from a few nL/min to a few mL/min, as well as pressures as high as 41 kPa [97].

Figure 2.9 shows the absolute value of the velocity generated by the Osmotex M8000 pump with solutions of KCl at 0.01 mM and 1 mM, for an applied square-wave potential of 100 mV and 50 mHz. The liquid is pumped very rapidly at every change of the polarity of the applied voltage, then its velocity decreases until the next polarity change. While a peak velocity of 103 $\mu m/s$ is generated with KCl at 0.01 mM, the average value is as low as only 15.4 $\mu m/s$.

If powering pumps designed for DCEO with AC potentials successfully addresses the issues

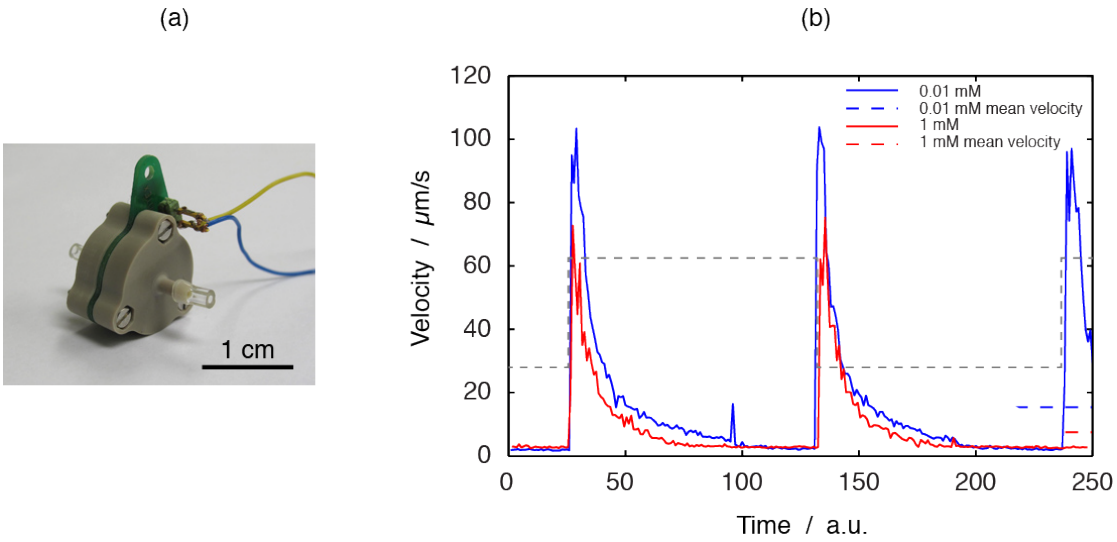

Figure 2.9: Characterisation of the absolute value of the velocity generated by the Osmotex M8000 pump with KCl solutions at different concentrations for an applied potential of 100 mV and 50 mHz. The shape of the applied square wave is given for reference.

related to electrolytic reactions, in many cases it still fails to provide an effective low-voltage and low-power actuation. The family of devices commonly referred to in the literature as AC electro-osmotic micropumps allow for a dramatic reduction of the applied potentials by patterning closely-spaced asymmetric electrodes.

AC potentials on planar electrodes

Asymmetry is the key to pumping liquids with AC electric fields. The first and simplest way of achieving a net ACEO force has been the fabrication of co-planar electrodes of different widths. Simple designs of ACEO pumps include planar electrodes patterned on the bottom side of channels that can have a wide range of shapes. For example, circular micropumps were presented by Debesset *et al.*, who fabricated a close circular channel made of a stack of glass/laminate/glass with Au/Cr electrodes [98]. Their devices were able to generate flow-rates of 10.5 nL/min for an applied voltage of 1.8 V_{RMS} at 5 kHz. Studer *et al.* used Ti/Pt electrodes and PDMS channels to fabricate a device with a similar structure and recirculating flow, which could achieve velocities of 400 $\mu m/s$ at an applied signal of 4 V_{rms} and 1 kHz [99].

Since the relative size of the large and small electrodes in the array sets the direction of the pumping force, flow reversal can only be achieved by applying much larger potentials or much smaller frequencies than the optimal value [100, 101]. Some groups suggested addressing this issue using configurable electrodes, such that the pumping direction can be chosen in real-time [102, 103]. The basic idea is to split the pair of asymmetric electrodes into three or more identical ones, and dynamically define the asymmetry by choosing which electrodes are powered with the same potential. An example of implementation of this idea is the work

of Huang *et al.*, who patterned Au electrodes on glass substrates and were able to generate forward and backward pumping, as well as clockwise and counterclockwise vortices in a PDMS channel [104] by applying a different set of voltages to the same group of electrodes. Their pumps were able to generate 80 $\mu m/s$ of forward velocity in the middle of the channel, using a signal of 16 V_{pp} and 2 kHz.

The pumping force can either be generated by using stationnary AC potentials on arrays of asymmetric electrodes, or travelling waves (TW) on arrays of identical electrodes. Experiments on AC and TW electro-osmotic pumping were conducted by García-Sánchez *et al.* using glass channels bonded to substrates with arrays of Au microelectrodes [105]. Their ACEO pumps were able to generate maximum fluid velocities of 4 $\mu m/s$ at 12 V_{pp} and 10 kHz, whereas the TWEO devices could produce slightly larger flow velocities of up to 38 $\mu m/s$ for an applied potential of 2 V_{pp} and 600 Hz.

More recently, a similar study was carried out by Yang *et al.* on configurable arrays of identical Au electrodes [106]. By properly choosing the potential on each electrode, they could achieve ACEO velocities of 35 $\mu m/s$ at an applied potential of 4.5 V_{pp} and 1 kHz, and TWEO velocities of up to 160 $\mu m/s$ for a travelling wave of 1.25 V_{pp} and 800 Hz. Xie *et al.* developed TWEO micropumps with poly-Si electrodes patterned on silicon nitride[107]. By applying a three-phase potential of 8 V_{pp} and 30 Hz, they were able to pump ethyl ethanol at a velocity of 250 $\mu m/s$.

Innovations of AC electro-osmosis

Researchers have also investigated ways of innovating planar ACEO micropumps. Some have demonstrated the possibility of fabricating devices at a lower cost, while others have focused their efforts on the implementation of new geometries to improve the generated flow-rates and pressures. Hansen *et al.* realised an all-polymer micropump using poly(3,4-ethylenedioxythiopene) (PEDOT) as the electrode material [108]. PEDOT was patterned on PMMA substrates by reactive ion etching (RIE) and the channels were fabricated in polyurethane, then bonded to the substrates with electrodes. Such pumps, filled with a solution of KCl at 0.1 mM, were able to generate velocities as high as 150 $\mu m/s$ and pressures of 4 Pa with an applied signal of 5 V_{rms} and 10 kHz.

Innovative geometries mainly include 3D electrode structures with a step-like profile. Unlike planar ACEO devices, all electrodes have the same width and the asymmetry required for pumping is provided by the 3D electrode profile. Not only is the pumping performance improved by such structures, but they also guarantee that the pumping direction can be reverted under no condition [109] . Hilber *et al.*, for example, fabricated Ti electrodes on glass substrates [110]. The metal was deposited on the top and bottom of 1.8-μm-deep grooves, in order to obtain a step-like profile for the electrodes. Channels were realised with SU-8 on separate wafers and subsequently bonded to the substrates with electrodes. Velocities of 250 $\mu m/s$ were measured directly above the electrodes when the channel was filled with DI

water and a potential of 3 V_{pp} and 700 Hz was applied.

An alternative strategy to fabricate step-like electrodes is to realise 3D insulating structures on a wafer, then have them tilted for metal evaporation, in such a way that the shadowing effect of taller structures allows the deposition of well-defined, separated electrodes [111]. Huang *et al.* used this approach to fabricate Cr/Au electrodes on glass substrates with SU-8 3D structures [109]. With an applied signal of 3 V_{pp} and 1 kHz, they were able to generate velocities of 1.2 mm/s on the electrode surface and an equivalent pressure of about 1.3 kPa, by using a high-resistance channel shaped like a serpentine.

Similar step-like electrode structures were also fabricated by Senousy *et al.*, exploiting the self-shadowing effect of 3D SU-8 structures, which were tilted at 50 ° during metal evaporation [111]. The velocity generated on the electrode surface was about 260 $\mu m/s$ with DI water filling the channel, and the device powered with a signal of 2 V_{pp} and 500 Hz. Guo *et al.* also reported 3D stepped electrodes. On one hand, they pumped very diluted saline solutions with step-like electrodes [112], achieving velocities as high as 500 $\mu m/s$ for an applied signal of 6 V_{pp} and 5 kHz. On the other, they fabricated interdigitated electrodes with T-shaped structures formed on top, which were able to pump the same liquid at 90 $\mu m/s$ when the same potential was applied [113].

Generating the ACEO force in 3D

Unlike previous examples, where the extent of the electrodes off the bottom surface of the channel was small compared to the total height of the channel, Rouabah *et al.* implemented a device based on 3D carbon electrodes extending over the entire cross-section [114]. They were able to pump a 0.1 mM solution of phosphate buffer saline at up to 120 $\mu m/s$, by applying a potential of 19 V_{pp} and 1 kHz. This represents an increase of the average generated velocity of more than 400% with respect to the planar devices, with electrodes on only one side of the channel. This huge improvement is linked to the significant increase in the contact surface between the electrodes and the liquid.

Improvement of velocity generation can also result from a 3D arrangement of planar electrodes. Chen *et al.* realised a pump based on ITO electrodes, insulated from the liquid by a parylene and teflon layer [115]. One large electrode was patterned onto the top surface of the channel and one slightly smaller was defined on the bottom wall. Upon application of an electric field, the liquid moved back and forth, following circular patterns in the portion of the channel with the electrodes. Even though no net flow exits this region, the electrodes are centimetres wide and the liquid can be moved over long distances. They measured velocities of about 1.2 mm/s on the electrode surface, when DI water was pumped with an applied potential of 340 V_{rms} and 140 kHz. Unfortunately, such a high voltage induced a high power consumption and heated the liquid at 42 $^{\circ}C$.

2.5 Comparison and summarising tables

Several other devices, not described in our review, have been developed and reported in the scientific literature. We have nonetheless offered a comprehensive list of the various and relevant approaches that researchers have investigated to implement electro-osmosis in the most effective and efficient ways. After surveying and learning about previous work, it is important and necessary to organise the information and compare the obtained results, in order to draw a conclusion on which approach best fits the objectives of this work.

Mechanical pumps, as well as devices that manipulate discrete droplets or use large electric or magnetic fields, can clearly not cope with the requirements of an implantable medical device. This is the reason why we did not include detailed examples about such micropumps. On the other hand, all kinds of electro-osmotic actuation are potentially interesting for our purpose, provided that we find a means of avoiding gas generation and the use of high voltages.

The following tables summarise the performances of the EO pumps that were presented. Table 2.1 shows the comparison of DC electro-osmotic micropumps. The indication of the channel materials and the nature of the buffer that was pumped is important in order to define the nature of the solid-liquid interface, which influences the formation of the electric double layer and therefore the flow generation. On the other hand, the value of the applied potential and the distance between the electrodes allow the appreciation of the strength of the electric field in the channel, while the fluidic performances of the devices can be directly assessed by referring to the generated flow-rates and pressures.

AC electro-osmotic pumps are more difficult to compare, since the actuation mechanism can be implemented in dissimilar and distinct ways. We have chosen to present separately the devices that exploit AC actuation on the same designs as DC electro-osmosis (Table 2.2), the conventional planar ACEO micropumps (Table 2.3) and the ACEO devices with improved design (Table 2.4). Because AC electro-osmosis depends on the metal-liquid interface on the electrode surface, the tables report the electrode instead of the channel material. Most papers about ACEO only report the measured velocity on the surface of the electrodes, while fewer indicate the average velocity in the channel; since the difference between the two values can be considerable, a flag indicates which one is reported. All parameters presented in the tables were either stated in the reference publications, or deduced from the data about the geometry of the devices. Although relevant for our study, the information about the power-conversion efficiency of the presented micropumps was not provided in the publications, nor could it be deduced from other data.

From the comparison of the tables for DC and AC electro-osmosis, we can assess the performances of the reviewed pumps according to their fluidic performances (i.e. flow-rate and pressure), the requirements in terms of potential and electric field, as well as the kind of buffer they were tested with.

Flow-rate and pressure generation are more effective in DCEO micropumps, which generate

values that are often three orders of magnitude (or even more) larger than for ACEO devices. The different geometries and cross-sections of the channels that were investigated can partially explain such contrasting performances. Another explanation comes from the analysis of how and where velocity is generated in DC and ACEO devices and will be discussed in Chapter 3.

The electric field present in DCEO devices is smaller than in ACEO pumps. DC electro-osmosis is therefore more efficient, as lower electric fields generate larger flow-rates and pressures.

The magnitude of the applied potential, on the other hand, is usually a hundred times smaller in ACEO devices than in DCEO pumps. This means that, for a similar current flow, the power consumption will be smaller in ACEO pumps. Furthermore, according to the application, the use of very large voltages may be dangerous or harmful.

Only diluted electrolyte solutions were used for the tests of ACEO micropumps, whereas DCEO devices could pump more concentrated buffers. When it comes to pumping medical or biological fluids, it is very important that the pumps can work properly with concentrated solutions, and this aspect will be investigated in the experimental part of this thesis.

Travelling-wave electro-osmotic pumps can generate larger velocities than ACEO devices, whilst using lower applied potentials. On the other hand, they are more complicated to implement and require a longer fabrication process.

Table 2.1: Summary and comparison of the DCEO pumps reviewed in Section 2.4.1. Some parameters were not reported in the cited works and have been derived from the operating conditions, when possible.

Reference	Channel	Buffer	Potential (V)	Electrode distance (mm)	Electric field (V/cm)	Flow rate (nL/min)	Pressure (Pa)
[80]	Pyrex	$Na_2B_4O_7$, 10	750	83	90.4	984	490
[30]	Glass	DI H_2O, 3 $\mu S/cm$	$3 \cdot 10^3$	1	$30 \cdot 10^3$	$2.5 \cdot 10^3$	$140 \cdot 10^3$
[81]	Silica	DI H_2O, 3 $\mu S/cm$	$2 \cdot 10^3$	54	370.4	$4.8 \cdot 10^3$	$2.3 \cdot 10^6$
[82]	Silica	NaH_2PO_4, 2	$5 \cdot 10^3$	200	250	$1.7 \cdot 10^3$	$10 \cdot 10^6$
[83]	Silica	NaH_2PO_4, 2	$4 \cdot 10^3$	50	800	$1.5 \cdot 10^3$	$24 \cdot 10^6$
[84]	Glass	NaH_2PO_4, 50	$3 \cdot 10^3$	50	600	$2 \cdot 10^3$	-
[85]	Quartz	1/10 PBS	10	3.2	31.3	415	$1.73 \cdot 10^3$
[86]	Silica/Alumina	$NaCl$, 2	370	5	740	$170 \cdot 10^3$	$1.6 \cdot 10^6$
[87]	Alumina	$Na_2B_4O_7$, 2.5	40	4	100	$142.5 \cdot 10^3$	-
[88]	Glass/SU-8	DI H_2O	40	0.5	800	10	65

Table 2.2: Comparison of the materials and performances of pumps having a similar design to DCEO devices, but powered with AC potentials.

Reference	Electrode	Fluid	Frequency (Hz)	Potential (V_{pp})	Electrode distance (mm)	Peak electric field (V/cm)	Flow rate (nL/min)	Pressure (Pa)
[92]	Au	-	0.8	8	0.1	400	3.4	-
[93]	Pd	$Na_2B_4O_7$, 20 mM	0.025	60	3.5	85.7	$5 \cdot 10^3$	$50 \cdot 10^3$
[94]	-	$NaCOOH$, 5 mM	15	400	15	133.3	2.4	600

Table 2.3: Comparison of the materials and performances of ACEO pumps with planar electrodes. The data about velocity also indicate whether the value was measured on the electrodes (E), in the middle of the channel over the electrodes (M) or outside the electrode region (P). According to the position where the velocity was acquired, a correction factor was applied to obtain the average value and the flow-rate (1/4 for E, 1 for M and 2/3 for P).

Reference	Electrode	Fluid	Frequency (Hz)	Potential (V_{pp})	Electrode gap (μm)	Peak electric field (V/cm)	Velocity ($\mu m/s$)	Flow rate (nL/min)	Pressure (Pa)
[98] AC	Cr/Au	KNO_3, 0.1 mM	$5 \cdot 10^3$	5.1	5	$5.1 \cdot 10^3$	(E) 50	7.5	-
[99] AC	Pt	KCl, 0.1 mM	$1 \cdot 10^3$	11.3	4.5	$12.6 \cdot 10^3$	(P) 400	34.8	66.9
[104] AC	Au	-	$2 \cdot 10^3$	16	20	$4 \cdot 10^3$	(M) 80	576	1.7
[105] AC	Au	KCl, 13 $\mu S/cm$	$10 \cdot 10^3$	20	10	$10 \cdot 10^3$	(M) 12	-	-
[105] TW	Au	KCl, 13 $\mu S/cm$	600	5.7	20	$1.4 \cdot 10^3$	(M) 80	-	-
[106] AC	Au	KCl, 0.1 mM	$1 \cdot 10^3$	4.5	10	$2.3 \cdot 10^3$	(M) 35	800	$20 \cdot 10^{-3}$
[106] TW	Au	KCl, 0.1 mM	800	1.25	10	625	(M) 160	$3.6 \cdot 10^3$	$89 \cdot 10^{-3}$
[107] TW	poly-Si	C_2H_5OH	30	8	3	$13.3 \cdot 10^3$	(E) 270	-	-
[108] AC	PEDOT	KCl, 0.1 mM	$10 \cdot 10^3$	14.1	5	$14.1 \cdot 10^3$	(P) 150	30	116

Table 2.4: Comparison of the materials and performances of ACEO pumps with 3D or alternative-shape electrodes. The data about velocity also indicate whether the value was measured on the electrodes (E), in the middle of the channel over the electrodes (M) or outside the electrode region (P). According to the position where the velocity was acquired, a correction factor was applied to obtain the average value and the flow-rate (1/4 for E, 1 for M and 2/3 for P).

Reference	Electrode	Fluid	Frequency (Hz)	Potential (V_{pp})	Electrode gap (μm)	Peak electric field (V/cm)	Velocity ($\mu m/s$)	Flow rate (nL/min)	Pressure (Pa)
[110] AC	Ti	DI H_2O	700	3	5	$3\cdot10^3$	(E) 250	90	-
[109] AC	Cr/Au	DI H_2O	$1\cdot10^3$	3	5	$3\cdot10^3$	(E) $1.2\cdot10^3$	45	233.4
[111] AC	-	DI H_2O	500	2	6	$1.7\cdot10^3$	(E) 260	81	0.9
[112] AC	poly-Si	$NaCl$	$5\cdot10^3$	6	4	$7.5\cdot10^3$	(E) 500	-	-
[113] AC	poly-Si	$NaCl$	$5\cdot10^3$	6	4	$7.5\cdot10^3$	(E) 90	-	-
[114] AC	C	PBS, 0.1 m	$1\cdot10^3$	19	20	$4.8\cdot10^3$	(P) 120	118	5.7
[115] TW	ITO	DI H_2O	$140\cdot10^3$	959	128	$37.5\cdot10^3$	(E) $1.2\cdot10^3$	-	-

2.6 Conclusion: ACEO meets most of the requirements

The review of the state of the art of microfabricated pumps has clarified the reasons motivating the present research and justifying the choice of the ACEO actuation. Mechanical pumps suffer from the complicated fabrication processes, the intrinsic fragility of the moving components and the large magnitude of the electric and magnetic fields required for their actuation. This can also result in excessive heating of the operating environment. Furthermore, approaches exploiting capillarity, electrowetting or surface acoustic waves are inadequate to gas-free working conditions. Electrohydrodynamic or magnetohydrodynamic devices also fail to provide low-power fluid actuation, and in some cases even affect the chemical nature of the pumped liquids.

On the other hand, electro-osmosis can be implemented with simple and fully integrated designs. Using AC fields largely addresses the issues related to gas generation, and the geometry of the electrodes enables low-voltage operation. Moreover, electro-osmosis has the potential to pump liquids having a wide range of conductivities [30]. As summarised in Table 2.5, ACEO pumps have many advantages over their DC counterparts, such as the ability to generate reasonable liquid velocities by using low or very low potentials, to avoid electrolysis and gas generation, as well as to adapt to the shape of the channel by having electrodes all along its path. Nevertheless they lack the ability to cope with large external pressures and tend to generate relatively lower flow-rates.

Table 2.5: Qualitative comparison of the characteristics of DC and AC electro-osmosis

	DCEO	ACEO
Flow rate	++	+
Backpressure	++	−
Low voltage	−	++
Electrolysis	−	++
Adapt to shape	+	++

In spite of the difficulty of withstanding high backpressures and the rare examples where AC electro-osmosis can increase the temperature of the working liquid, or induce gas generation by electrolysis, due to extreme operating conditions (large voltages, very low or very high frequencies), this actuation principle appears to be the most suitable for implantable systems. Moreover, the potential of AC electro-osmosis for biological application has recently been shown by the implementation of electrode arrays for the delivery of biological cells and reagents [116]. We prefer ACEO to TWEO micropumps because of their simpler fabrication and operation; moreover, the approaches investigated in the present work to improve the performances of ACEO devices can be applied as such to TWEO pumps. The following chapters will show how it is possible to increase the flow-rate generation and the pressure capability of ACEO pumps with simple designs and fabrication techniques.

3 Theory of Electro-Osmosis and Design Considerations

Electro-osmosis is a remarkable phenomenon and one that is surprisingly effective at pumping liquids. The source of the pumping force relies on a layer of charges that is usually several thousand times smaller than the diameter of the channel in which the liquid is set in motion. This would be like having a traffic jam on a motorway and making all the cars move simply by pulling on a hair, which is lying on the side of the road. Microscale physics allows for this kind of effect to take place. The theory of electro-osmosis describes such phenomena and allows us to understand and master them.

3.1 Introduction

The remarkable force that can be generated in the electric double layer can produce observable effects thanks only to the reduced dimensions of the system and the viscosity of the liquid. As a matter of course, the magnitude of the electric force responsible for electro-osmosis depends on the nature of the liquid and the solid surface, as well as on the characteristics of the applied electric field.

In Chapter 2, we also showed that DC electro-osmosis is much more effective than AC electro-osmosis at generating high pressures. This behaviour depends on the geometrical distribution of the EO forces. The first part of this chapter will describe the details of how DC and AC electro-osmotic flows are generated. It will be clear that the extent of the electric double layer around the channel has a strong influence on the average value of the generated velocity. We will draw on this conclusion to suggest a simple way of implementing an improved ACEO micropump.

When it comes to pumping and, in particular, to ACEO, the geometry of the device influences the overall pumping performance in more than one way. Not only are the extent of the electrodes and their aspect ratio crucially important, but the flow-rate that the device can generate is also influenced by the number of electrode pairs and the shape and size of the connections to the external fluidic network. These issues will be discussed at the end of

the chapter. Finally, an electrical model of the ACEO pump will be presented to aid the understanding of the influence of electrical properties on the fluidic performances.

3.2 The electrical double layer

Consider a microchannel filled with an aqueous solution of an electrolyte at a concentration c_0. When the solid wall and the liquid come into contact, chemical reactions occur at the solid-liquid interface. As a consequence, electric charges build up on the surface of the solid and give rise to a non-zero electrical potential, usually called the zeta potential (ζ), which attracts oppositely charged ions from the solution towards the wall [117].

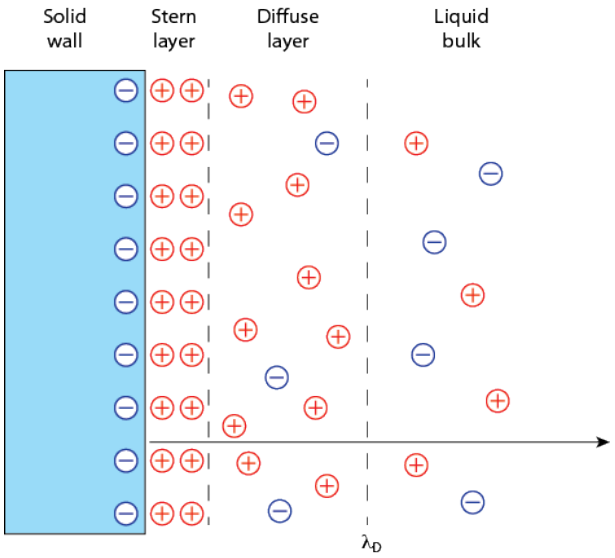

Figure 3.1: Schematic view of the charge distribution and the electric double layer that forms in front of a glass wall. The Stern and diffuse layer are highlighted.

For a glass channel, the following reaction takes place between the silica molecules on the surface and the water molecules in the solution [118]

$$H_2O + SiO_2 \rightleftarrows 2SiOH^-.$$

Thus, the wall becomes negatively charged and positive ions accumulate in front of it, giving rise to a local non-zero charge density. At the thermodynamic equilibrium, as illustrated in Figure 3.1, the volume next to the wall is occupied by a very thin and compact layer where only positive ions are present, called the Stern layer, and a thicker diffused layer where positive ions are the majority. The whole region with non-zero charge density is called the electrical double layer (EDL).

A simple model for the the double layer

A simple approach to model the EDL is to regard ions in a dilute solution as an ideal gas. Therefore, considering that far away from the wall, the ion concentration approaches c_0 and the electrical potential 0, the concentrations c_+ (of positive ions) and c_- (of negative ions) can be written as a function of the distance $\vec{r}$ from the wall. Their expression is derived from that of the chemical potential [1] and gives the following distribution for the charge density in front of the wall

$$\rho_{el}(\vec{r}) = Z_i e[c_+(\vec{r}) - c_-(\vec{r})] = -2Z_i e c_0 \sinh\left[\frac{Z_i e}{k_B T}\psi(\vec{r})\right], \tag{3.1}$$

where Z_i is the ionic valence of the species in solution and $\psi_T = k_B T/e$ the thermal voltage.

Charge density and electrical potential in a volume are related by the Poisson equation, which states that given a charge density $\rho_{el}(\vec{r})$ in a volume, the potential will vary as $\epsilon\nabla^2\psi(\vec{r}) = -\rho_{el}(\vec{r})$ [119]. After substituting the expression for the charge density in this law, we obtain a differential equation for the potential, called the Poisson-Boltzmann (PB) equation:

$$\epsilon\nabla^2\psi(\vec{r}) = 2Z_i e c_0 \sinh\left[\frac{Z_i e}{k_B T}\psi(\vec{r})\right]. \tag{3.2}$$

In the case of a charged wall, only the x direction (going from the wall towards the bulk) is relevant, the system being invariant along the other two dimensions. The boundary conditions for the PB equation are that the potential should be equal to ζ on the wall, i.e. $\psi(0) = \zeta$, and it should be equal to 0 in the bulk of the liquid, i.e. $\psi(\infty) = 0$.

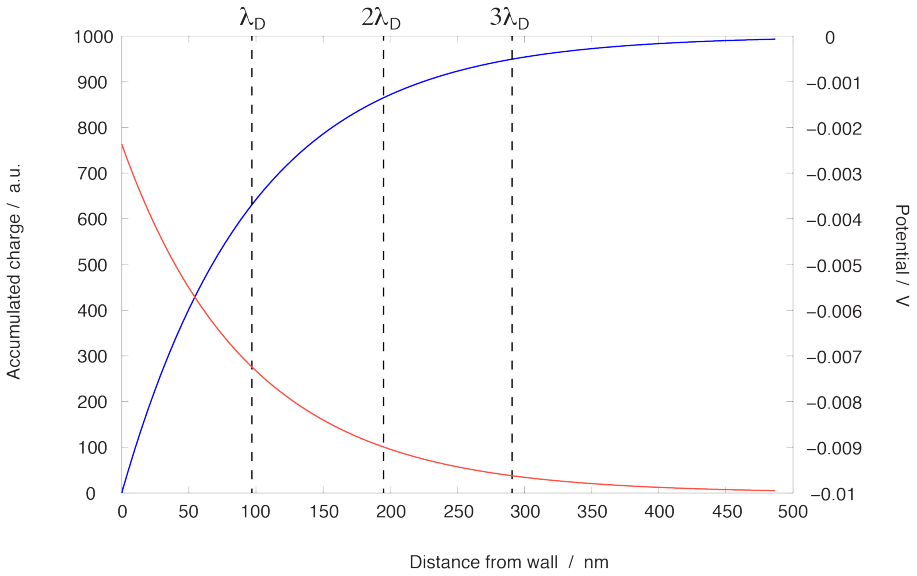

Figure 3.2: Potential (blue) and charge (red) distribution in the EDL, for a small zeta potential (linear regime), according to the Poisson-Boltzmann model.

When the zeta potential is much smaller than the thermal voltage, the PB equation can be linearised and solved analytically. For a simple 1:1 electrolyte, i.e. a salt with only one positive and one negative ion such as KCl, the potential is given by [1]

$$\psi(x) = \frac{4k_BT}{Z_i e} \tanh^{-1}\left[\tanh\left(\frac{Z_i e\zeta}{4k_BT}\right)\exp\left(-\frac{x}{\lambda_D}\right)\right]. \tag{3.3}$$

Here we introduce the quantity

$$\lambda_D = \sqrt{\frac{\epsilon k_B T}{2Z_i^2 e^2 c_0}}, \tag{3.4}$$

which is called the Debye length and which approximates with good accuracy the thickness of the EDL. An example of the potential and charge distribution for a solution of KCl 0.01 mM in contact with a glass wall is given in Figure 3.2. Typical values of λ_D range between a few nanometres (high concentration buffer) to 100 nm (low concentration buffer) [120].

The modified Poisson-Boltzmann model

As soon as the zeta potential becomes a few times larger than the thermal voltage, as is the case for AC electro-osmosis, the linear regime approximation is no longer valid. In fact, because of the increased wall potential, many more ions will be attracted towards the wall and their local concentration will be defined by their finite dimensions. This is called the steric limit and the behaviour of the electrolyte can no longer be accurately described by the same models used for the linear regime[121, 122].

When a highly non-linear regime is reached, i.e. $\zeta \gg \psi_T$, the solution close to the wall ceases to be diluted and the equations describing the relationship between the potential distribution and the ion concentration need to be redefined. If a is the size of one ion, the concentration shall saturate at the maximum value $c_{max} = a^{-3}$ [123]. Therefore, the extent of the condensed layer, where ions are closely accumulated, will increase. The concentration of ions close to the wall is described by the modified Boltzmann distribution [121]

$$c_\pm = \frac{c_0 \exp(\mp ze\psi / k_B T)}{1 + 2\nu \sinh\left(\frac{ze\psi}{2k_B T}\right)^2}, \tag{3.5}$$

where $\nu = 2a^3 c_0$ is the ratio between the concentration of the solution and the maximum allowed concentration, and is called the packing parameter.

Substituting this expression for the charge distribution in the Poisson law gives the modified Poisson-Boltzmann (MPB) equation relating the charge density to the potential in the system. Such an equation can hardly be solved analytically, but it has been integrated to find the total charge density [121] and can be simulated with the finite element method (FEM) to approximate the potential and charge distribution [124]. Figure 3.3 shows an approximated

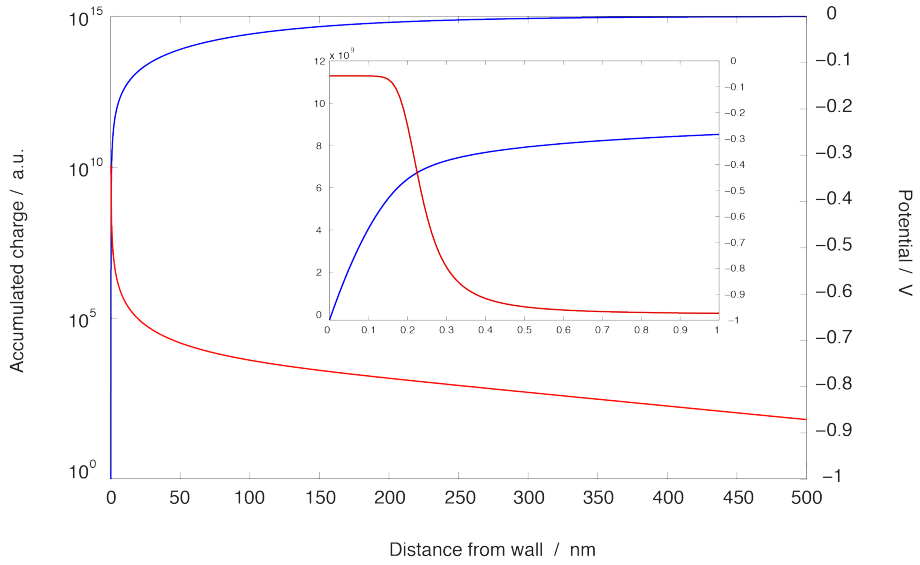

Figure 3.3: Potential (blue) and charge (red) distribution in the EDL, for a large zeta potential (highly non-linear regime), according to the modified Poisson-Boltzmann model.

solution for a solution of KCl at 0.01 mM in contact with a wall, to which a potential of 1 V has been applied. The overall length of the double layer is larger than for the linear regime.

3.3 DC electro-osmosis

Aqueous solutions can be effectively pumped by applying an electric force to the charges accumulated in the EDL. In the case of DC electro-osmosis (DCEO), the system is operated in the linear regime, since the potential on the channel walls is the intrinsic zeta potential of glass in water. Therefore, Equation 3.2 holds, as well as all approximations derived from it.

The pumping potential V_0 is usually applied across the entire length L_c of the channel and the DCEO force that develops in the EDL is $F_{dceo} = \rho_{el} V_0 / L_c$. Such force acts on the ions in the EDL, which in turn drag the surrounding liquid. Finally, the generated motion is transmitted to the bulk of the liquid by viscosity, thanks to the laminarity of flows on the microscale.

In the very small time elapsing between the moment at which the potential is turned on and the moment at which a full electro-osmotic flow is developed, the velocity profile across the channel evolves as illustrated in Figure 3.4, which shows the result of a Lattice-Boltzmann simulation [125] performed following examples found in the literature [126, 127, 128] and described in Appendix A.1. The steady-state profile generated by DCEO is flat and the velocity is constant across the whole of the channel section, except within the EDL, where it becomes smaller and reaches 0 on the wall itself.

Given the properties of the liquid and the applied pumping potential, the electroosmostic

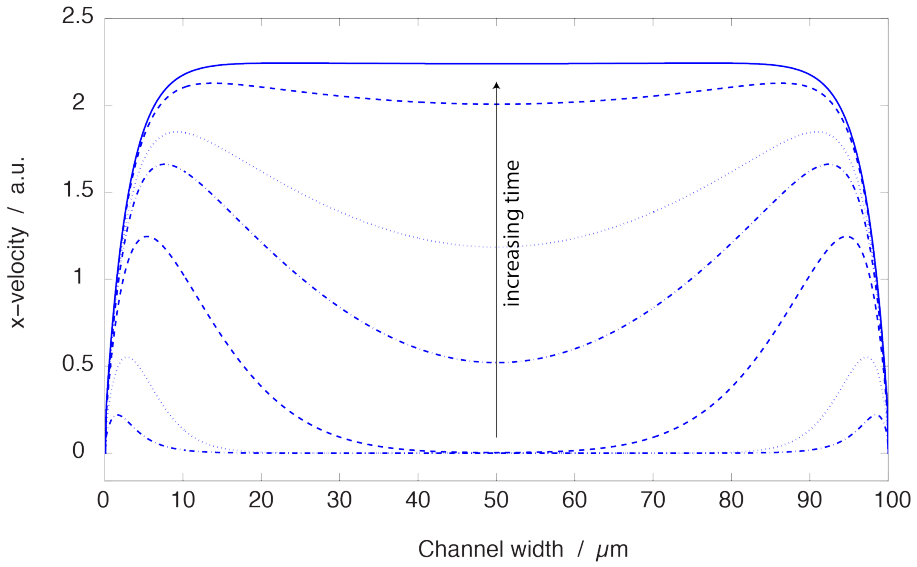

Figure 3.4: Lattice-Boltzmann simulation of the onset of a DC electro-osmotic flow. The vertical arrow indicates the direction of increasing time.

velocity is defined by the Helmholtz-Smoluchowski relation [1] as

$$v_{eo} = \frac{\epsilon\zeta}{\eta\lambda_D}\frac{V_0}{L_c}, \tag{3.6}$$

where ϵ and η are respectively the electric permittivity and the viscosity of the solution. Because the velocity is constant over the cross-section of the channel, DCEO flows can easily stop or overcome contrary pressures. Because the Navier-Stokes equations in low-Reynolds-number regimes are linear, the overall flow profile in the presence of a backpressure is given by the superposition of the electro-osmotic and pressure flows ($v_{tot} = v_{dceo} - v_{\Delta p}$), which both have a maximum velocity in the middle of the channel, as shown in Figure 3.5.

As seen in Chapter 2, DCEO is able to generate flow-rates as high as 1.5 mL/min [86] and electro-osmotic pressures as large as 3 MPa [82]. The effectiveness of DCEO depends weakly on the temperature and is expected to increase with the reduction of the salt concentration and the capillary radius [81]. On the other hand, velocity generation by electro-osmosis encounters strong limitations when the diameter of the channel is comparable to the thickness of the electric double layer [129, 130]. In such conditions, a non-flat velocity profile is generated instead of the plug-like profile that is observed in larger microchannels [131].

Electrolysis

One major issue connected to the operation of DCEO pumps is the generation of gas through the process of electrolysis. When a direct current passes through an aqueous solution of an electrolyte, it can result in the separation of the species present in the solution, in particular

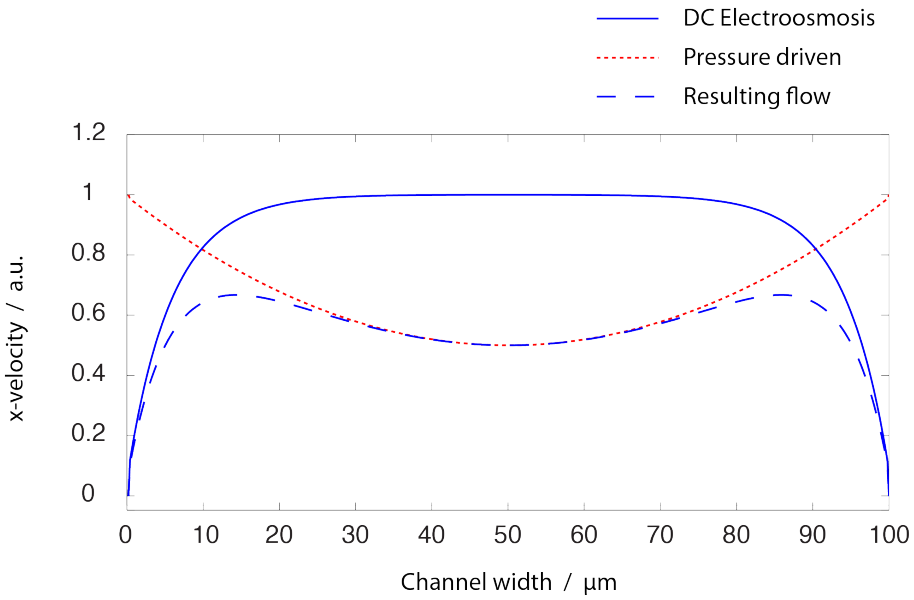

Figure 3.5: Superposition of a DCEO (solid blue) and a pressure-driven flow (red) in a microchannel: the resulting flow profile (dashed blue) is positive.

water, into their elementary constituents [132].

When only pure (DI) water is present, hydrogen will be reduced at the negative electrode following the reaction $2H^+ + 2e^- \rightarrow H_2$ and oxygen will be oxidised at the positive electrode, according to the reaction $2H_2O \rightarrow O_2 + 4H^+ + 4e^-$. In order to take place, each of these reactions require a certain potential on the corresponding electrode. Since the amount of product of the reactions is proportional to the total charge given to the system (1^{st} law of Faraday), their speed will be limited by the current flowing through the circuit [133]. The electrolysis of DI water, which is a very poor conductor, will therefore be very slow.

The addition of an electrolyte to the solution increases the conductivity and will accelerate the reactions of electrolysis. Nevertheless, the ions of the electrolyte will compete with hydrogen and oxygen to obtain (respectively give) electrons from (respectively to) the electrodes. In a solution of KCl, which was used to test the devices presented in this thesis, the two half-reactions occurring at the electrodes are the reduction of hydrogen, as described above, and the oxidation of chlorine, following $2Cl^- \rightarrow Cl_2 + 2e^-$ [132], which prevails on the half-reaction producing oxygen.

Electrolysis commences when a minimum potential, related to the standard potential of the reaction by the Nernst equation, is applied to the electrodes and will accelerate as the applied potential increases [133]. While the minimum required potentials are typically in the order of $1-2\ V$ [134], DCEO uses extremely high voltages and therefore gives rise to a constant electrolytic activity.

A possibility to avoid electrolysis, and the generation of gases within the pump, is to use an

alternating potential to induce the EO flow. If an AC voltage is applied to the electrodes in the same symmetric configuration as for DCEO, the net velocity generation will be zero. It is therefore necessary to introduce a certain degree of asymmetry to be able to pump liquids in a constant direction using AC voltages.

3.4 AC electro-osmosis

Instead of allowing the EDL to form spontaneously according to the intrinsic properties of the solid-liquid interface, the phenomenon can be controlled through the application of an external voltage on the wall. This potential usually exceeds the thermal voltage by a large factor, and brings the system into a strongly non-linear regime, where the charge distribution is governed by the MPB equation.

Typically, for AC electro-osmosis (ACEO), pairs of electrodes are patterned on a flat substrate, onto which a pre-fabricated channel is bonded. Therefore, most pumps have their electrodes on the bottom side of the pumping channel [27]. The EDL and the pumping force are both generated by the applied potential, at the interface between the electrodes and the solution.

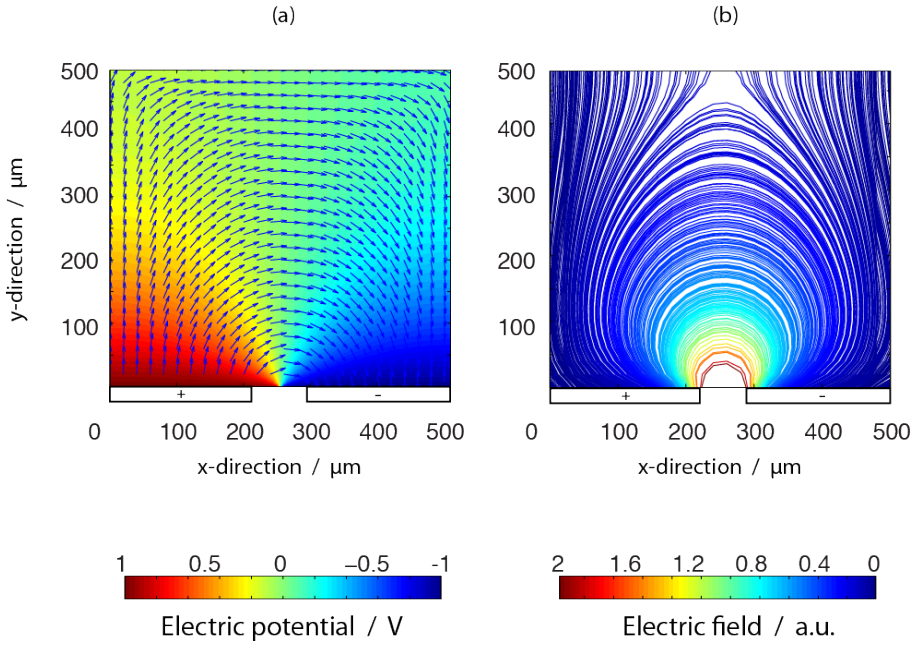

Figure 3.6: Simulation of the potential distribution in a solution of conductivity 2.1 mS/m in contact with a pair of symmetric electrodes separated by a gap of 10 μm. The applied voltage is 1 V on the left-hand electrode and -1 V on the right. The surface plot of the potential is given with the arrow plot of the electric field (a), which has lines with a circular shape (b).

On the surface of each electrode, the perpendicular component of the electric field will contribute to the formation of the EDL, whose charge density will be proportional to the applied potential, whereas the component parallel to the electrode and the channel will

induce a force $F_{aceo} \sim \rho_{el} V \sim V^2$ on the accumulated charges. This force is the AC electro-osmotic force: since a positive voltage will attract negative charges and vice versa, it will always point towards the same direction, from the gap towards the outer part of the electrode [135]. Others have explained the ACEO force by referring to a gradient in charge density that forms above the electrodes: regions close to the electrode edges are screened at a faster rate and accumulate a higher charge density than those far from the gap. The gradient would then set the ions in motion [108].

If the electrodes were the same size, there would be no net pumping. On the other hand, when the electrodes are asymmetric, there will be a net flow generation and the large electrode will determine the direction of such flow [78].

For a given system constituted by a small (S) and a large (L) electrode, separated by a gap (G), the applied potential will be in the form $V_S = -V_L = V_0/2 \cdot \sin 2\pi f t$ and will induce in the system an electric field having a rounded shape and going from one electrode to the other, as illustrated by the COMSOL simulations in Figure 3.6.

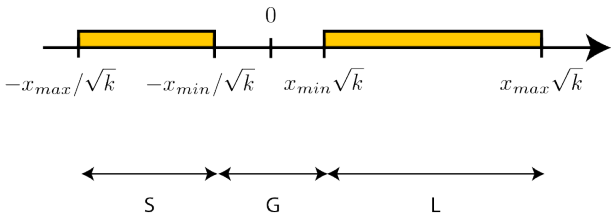

Figure 3.7: Coordinate system used for the computation of the average velocity generated on the electrode surface by AC electro-osmosis.

According to Brown *et al.* [136], given the geometry of the device, it is convenient to define a coordinate system as in Figure 3.7, where the origin is located within the gap and each electrode is included between the coordinates $x_{\min}$ and $x_{\max}$. The velocity generated on one electrode can then be evaluated as a function of the magnitude V_0 and the angular frequency $\omega = 2\pi f$ of the applied potential, as well as of the position along the electrode. This expression for $v(x)$ should be integrated and averaged to obtain the mean generated velocity over one electrode

$$v_{aceo} = \frac{1}{x_{\max} - x_{\min}} \int_{x_{\min}}^{x_{\max}} \frac{v_0}{x} V_0^2 \frac{(\omega x/\omega_0)^2}{(1+(\omega x/\omega_0)^2)^2} \mathrm{d}x, \tag{3.7}$$

where, for given width-ratio $k = L/S$ of the electrodes and viscosity η of the solution, v_0 and ω_0 are constants defined as

$$v_0 = \frac{\epsilon}{2\eta\sqrt{k}(1+k)^2} \tag{3.8}$$

$$\omega_0 = \frac{2\sigma_0 \lambda_D}{\pi\epsilon}. \tag{3.9}$$

It is important to underline that both the electric field and the induced charge density in the EDL oscillate over time. Therefore, the continuous flow that is proportional to the constant product of charge density and electric field, and has a non-zero time average, should be superimposed to an alternating motion at the same frequency as the applied potential, which has not been observed so far in experiments [137, 138, 139].

The average velocity generation described by Equation 3.7 can be simulated in Matlab [140], in order to evaluate the influence of the electrode size and the buffer concentration on the velocity generation. The script used for the simulation is given in Appendix A.2 and accounts for the parameters relating the value of the velocity generated on the electrode surface to the velocity observed in the middle of the channel distant from the electrodes, as explained in Section 3.6.

Figure 3.8 show the simulated velocity for electrodes having the same L/S ratio, but different sizes: the generated fluid motion clearly increases for smaller electrode sizes. On the other hand, as the graphs obtained for buffer concentrations going from 0.01 mM to 10 mM and shown in Figure 3.9 illustrate, the frequency of optimal velocity generation is expected to shift towards lower values when the buffer concentration is increased. On the other hand, the simulations fail to account for the influence of the buffer concentration on the magnitude of the generated velocity, as it will be discussed in Chapter 6.

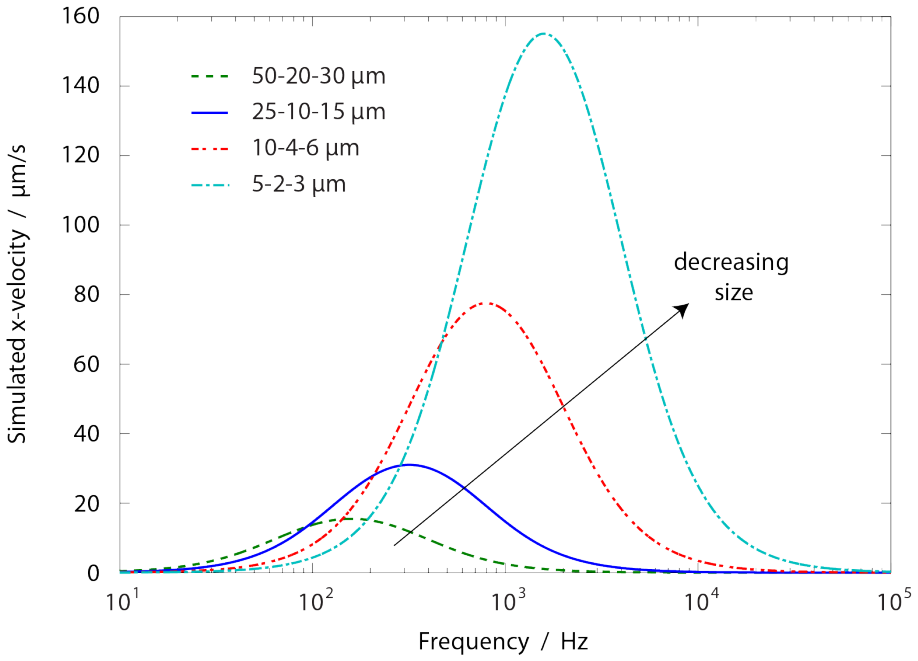

Figure 3.8: Simulated velocity generated by AC electro-osmosis in the middle of the channel distant from the electrodes, using Equation 3.7. The graphs are shown for different sizes of the electrodes (indicated as *large electrode-gap-small electrode*).

Basic electrode configurations, such as the one described in Figure 3.7, give rise to a liquid flow where the velocity has its maximum value on one side of the channel. Moving away from

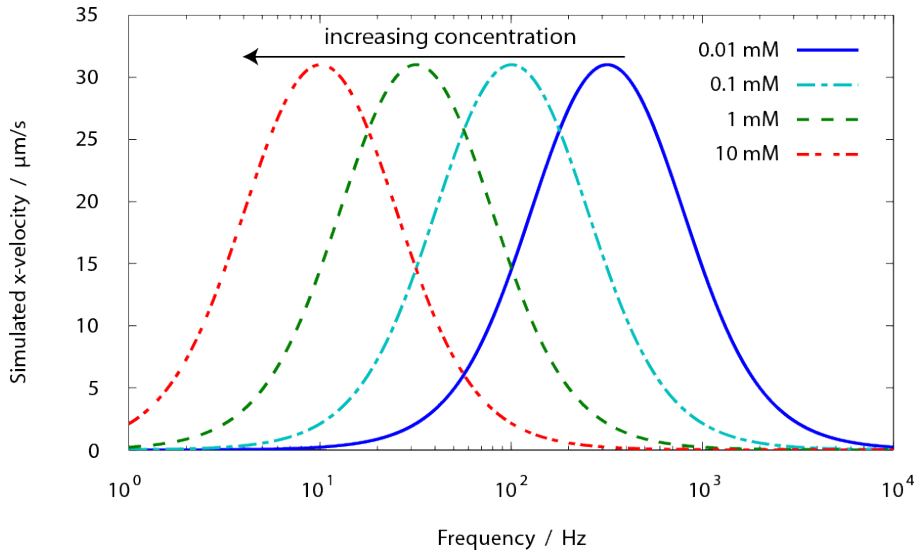

Figure 3.9: Simulated velocity generated by AC electro-osmosis in the middle of the channel distant from the electrodes, using Equation 3.7. The graphs are shown for buffer concentrations between 0.01 mM and 10 mM.

the electrode surface, the velocity will decrease until reaching a zero value on the other walls (where no electrodes are present), as illustrated in Figure 3.10. This flow pattern is called, in the literature, a Couette flow [1]. Unlike DCEO, where the velocity is maximum and constant over the entire cross-section, ACEO lacks the effectiveness to stop backpressures. In fact, when a pressure-driven flow opposes one generated by ACEO, the overall velocity in the channel will be $v_{tot} = v_{aceo} - v_{\Delta p}$ and will be easily dominated by the pressure-driven flow, which has its maximum in the middle of the channel, where the velocity of the ACEO flow is already much reduced.

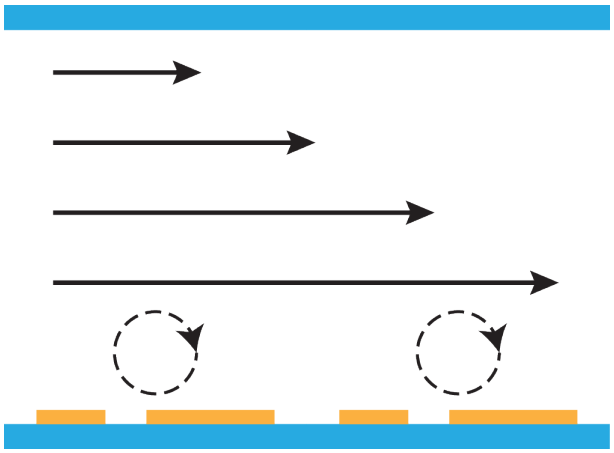

Figure 3.10: Typical velocity profile generated by AC electro-osmosis. The liquid moves with maximum velocity just above the electrodes, while no motion can be observed next to the walls without electrodes.

Reduced power consumption

In DCEO systems, large potentials are applied across the whole length of the channel in order to obtain a large electric field. On the other hand the electrodes for ACEO are closely spaced, and the application of small potentials is sufficient to generated large electric fields and pumping forces within the liquid. As summarised in Table 3.1, a voltage of 1 kV applied across a length of 1 cm induces the same field as 1 V applied across 10 μm.

Table 3.1: Typical values of the applied potential and resulting electric field in DC and AC electro-osmotic devices.

	Voltage (V)	Electrode distance (mm)	Electric field (V/m)	Current flow (μA)	Power consumption (μW)
DCEO	10^3	10	10^6	10	10,000
ACEO	1	0.01	10^6	100	100

Geometry allows ACEO to exploit lower voltages. At the same time, the average generated velocity depends on the square of the applied voltage: again, small values of the applied voltage may be sufficient to induce a large enough liquid motion.

By using lower potentials, ACEO also consumes less power than DCEO. In fact typical values of voltages and currents encountered in systems exploiting DC electro-osmosis are in the range of the kV and of the tens of μA [30, 141], which corresponds to a power consumption in the order of $W_{el} = V \cdot I \approx 1\ kV \cdot 10\ \mu A = 10\ mW$. On the other hand, as presented in Chapter 6, the current levels in ACEO micropumps are in the order of 100 μA, while the applied voltages are usually of a few V. Therefore, typical power consumption in ACEO systems is in the order of $W_{el} = V \cdot I \approx 1\ V \cdot 100\ \mu A = 100\ \mu W$, which is 100 times smaller than for DC electro-osmosis.

Electrolysis

While using AC potentials allows the elusion of the effects of electrolysis [93], using small voltages contributes to strongly limiting this phenomenon. In fact, with AC electro-osmosis the reactions of electrolysis either do not take place, because the voltages are too small, or are reverted at every half-cycle, when the polarity of the potential switches, and there is usually no net gas generation.

Nevertheless, it is possible to find working conditions, depending on the concentration of the buffer, and the frequency and magnitude of the applied AC potential, at which electrolysis occurs and gas is generated. Such conditions include very low frequencies and/or very high potentials [142] and may represent important limitations to the operation of ACEO pumps.

3.5 Emulating DC electro-osmosis

Several works have addressed the issue of the limited flow-rate and pressure capability of AC electro-osmosis. The simulations performed by Burch *et al.* showed that up to 60% velocity increase could be obtained by using a partial 3D electrode design, in which one electrode is thicker than the other [143]. This principle was implemented in some of the improved ACEO micropumps that we presented in Chapter 2, and the enhancement of the pump performance relies on a different spatial distribution of the velocity generation. Unlike the planar design, where the liquid on the surface of each electrode moves in opposite directions, the 3D-stepped design localises the counterflows in the vertical space between the low and tall electrode surface, in such a way that it cannot hinder the overall flow in the channel.

On the other hand, Rouabah *et al.* fabricated and tested 3D electrodes made of carbon [114], which were as high as the channel depth, and showed that the velocity could be increased by about 440%. In this case, the huge increase of the average generated velocity is obtained by increasing the electrode surface in contact with the working liquid, thus increasing the total surface where the ACEO force is generated.

Indeed, any approach that can improve the magnitude of the generated velocity and the flow-rate also increases the pressure capability of the pump, since $\Delta p = R_{hyd} \cdot Q$. Nevertheless, using 3D structures has the main drawback of requiring complicated fabrication technologies and of occupying a portion of the channel cross-section, thus reducing the space where the liquid can flow.

This thesis presents a different approach to improving ACEO velocity generation. The effectiveness of DC electro-osmosis arises from the fact that the pumping force is generated in the double layer of charges present on the whole surface of the channel. Therefore the walls, which usually slow down the passage of a liquid, do not have any decelerating effect on it. Unlike DC electro-osmosis, in a basic ACEO configuration velocity is generated only on one side out of four, and the walls where there are no electrodes will slacken the motion of the fluid in the channel.

Is it possible to generate an ACEO force on the whole surface of the channel, therefore emulating DC electro-osmosis? Intuitively, if the electrodes are extended all around the channel, the pumping force will be induced on its entire perimeter and a plug-like flow, such as in DCEO, shall be generated.

Theoretical proof

We can ideally approximate ACEO velocity generation as a Couette flow (or a superposition of more Couette flows) where a constant non-zero slip-velocity is imposed on one or more sides of the channel [144]. By doing so, it is possible to verify analytically and through simulations the validity of our assumptions.

When a rectangular microchannel, as in Figure 3.11, is considered in a low-Reynolds-number regime, the velocity field $\vec{v}(x,y,z) = v(y,z)\vec{e}_x$ does not depend on the x coordinate. Moreover, if we consider the problem at steady-state, the velocity will not depend on the time either. For these reasons, and if we assume that no external forces are applied to the liquid, the Navier-Stokes equation is reduced to

$$\eta \nabla^2 v(y,z) = 0. \tag{3.10}$$

The boundary conditions for such a problem will be that the slip-velocity on each side of the channel is either 0, on the sides without electrodes, or a constant v_{aceo}, on the sides with electrodes, as summarised in Table 3.2. The particular solution to the problem when the velocity is non-zero only on one side of the channel (at $z = 0$) is given by [145]

$$v(y,z) = \sum_{n=1}^{\infty} \frac{2v_{aceo}(1-\cos(n\pi))}{n\pi} \sin\frac{n\pi y}{W} \frac{\sinh\frac{n\pi(H-z)}{W}}{\sinh\frac{n\pi H}{W}}. \tag{3.11}$$

Similar solutions can be found when the same problem is solved with the constant velocity imposed, in turn, on the other sides of the channel. Because we are working in a regime where the Navier-Stokes equation is linear, the solutions for the two-side-electrode design (respectively all-around-electrode) are then given by the superposition of two (respectively all) of the solutions to the simpler problems with only one boundary condition. Softwares such as Matlab [140] allow for computing and plotting numerical approximations of these complex series, as detailed in Appendix A.3. Figure 3.12 shows the approximated velocity profiles over the cross-section of the channel when velocity is generated on one, two or all sides.

It is interesting to compute the average velocity over the channel cross-section for the examples

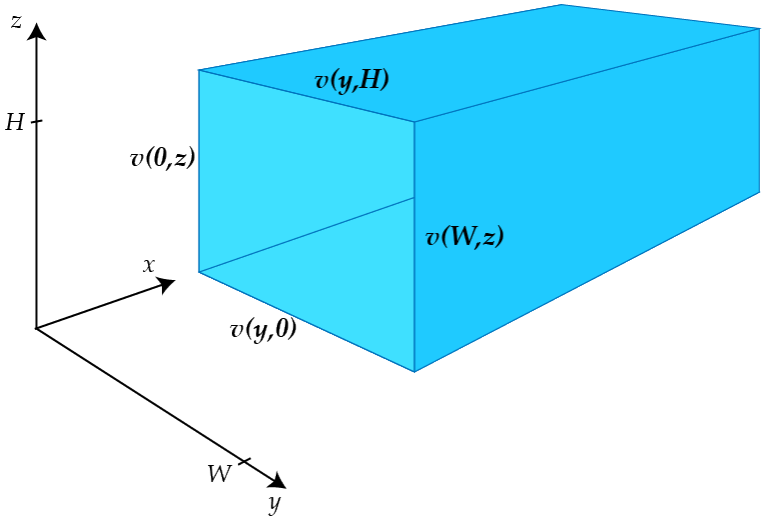

Figure 3.11: Channel structure considered for the theoretical analysis and simulation of multi-side ACEO flows.

Table 3.2: Boundary conditions for the Navier-Stokes equation, for the one-side- (1SE), two-side- (2SE) and all-around-electrode (AAE) configurations.

	1SE	2SE	AAE
$v(y,0)$	v_{aceo}	v_{aceo}	v_{aceo}
$v(0,z)$	0	0	v_{aceo}
$v(y,H)$	0	v_{aceo}	v_{aceo}
$v(W,z)$	0	0	v_{aceo}

given in Figure 3.12 and plot it against the ratio of the length over which velocity is generated to the total perimeter of the channel. This confirms that we can obtain a plug-like flow by patterning electrodes and generating velocity on all sides of the channel and that the mean generated velocity is proportional to the ratio between the perimeter of the channel covered by electrodes $\mathscr{P}_{el}$ and the total perimeter of the channel $\mathscr{P}_{tot}$

$$v_{ave} = \frac{\mathscr{P}_{el}}{\mathscr{P}_{tot}} v_{aceo}. \tag{3.12}$$

Side-effects of the all-around design

While multiplying the average velocity generation of the pump, the other effect of extending the length of ACEO electrodes is to increase the current consumption of the device. In fact, the current density J across the electrodes will remain constant, while the area becomes larger; therefore, the total current $I = J \cdot A = J \cdot w \cdot \mathscr{P}_{el}$ will grow proportionally to the perimeter of the channel covered by electrodes.

3.6 Influence of the geometry

The extent of the electrodes around the channel is not the only geometrical parameter that has an influence on the performances of ACEO.

Extent of electrodes along the channel

It is also important to carefully choose the length of the portion of channel where electrodes are patterned. In fact, regardless of the kind of velocity profile that is generated above the electrodes, the flow will have a parabolic, or Poiseuille [1], profile in the portion of the channel where no electrodes are present, and at the inlet and outlet. It can be shown [144] that the maximum velocity of such a profile depends linearly on the ratio of the length of the channel with electrodes to the total length of the channel. The maximum Poiseuille velocity is given by

$$v_{pois} = \frac{\beta}{\alpha} \frac{L_{el}}{L_{tot}} v_{aceo}, \tag{3.13}$$

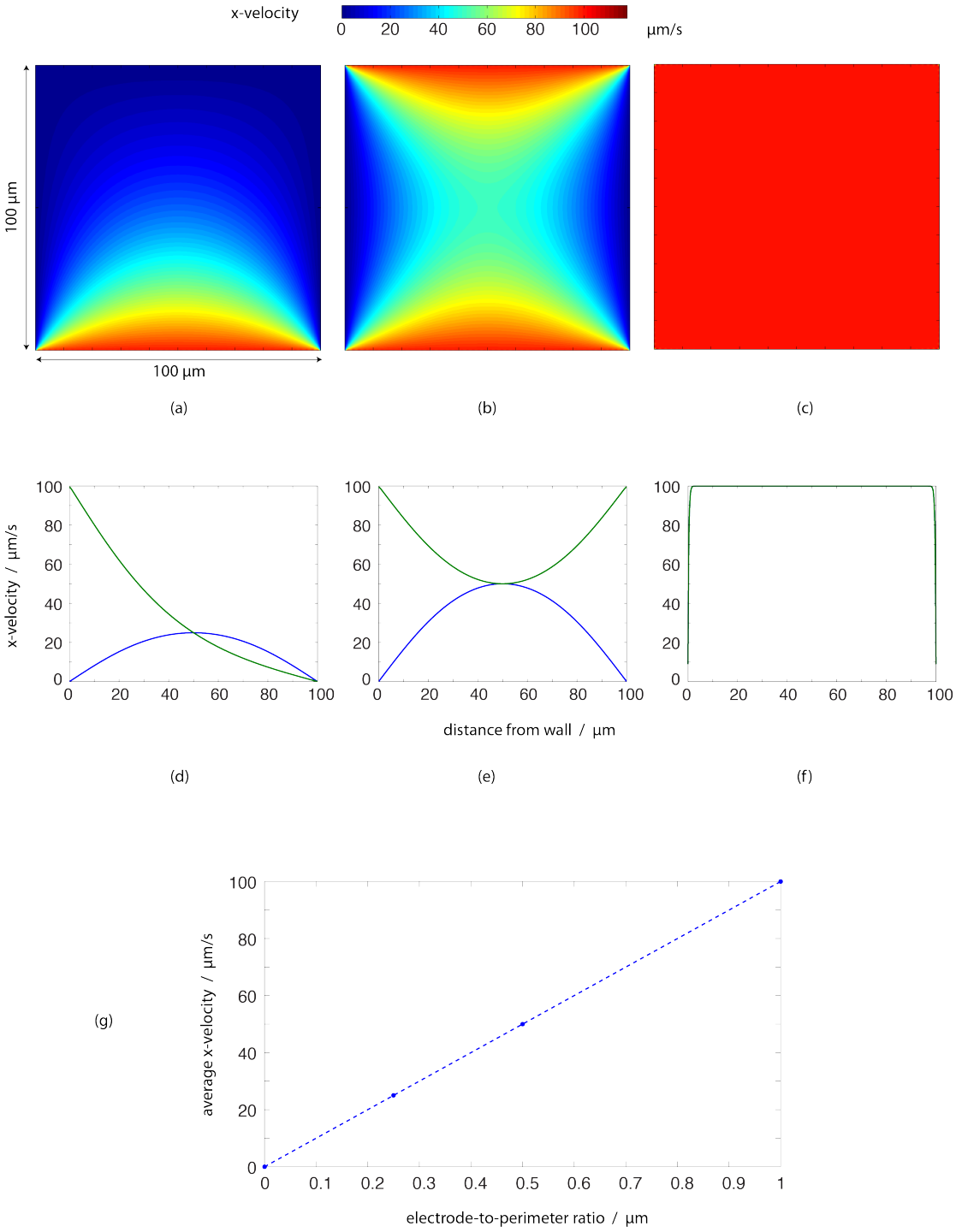

Figure 3.12: Simulated flow over the channel cross-section when the velocity is generated on one (a), two (b) or all (c) walls. The flow profile along vertical and horizontal cut lines is also given for the 1SE (d), 2SE (e) and AAE (f) cases, alongside the dependance of the average velocity on the extent of the electrodes around the channel (g).

where α is a coefficient that accounts for the shape of the channel cross-section, $\beta = \mathscr{P}_{el}/\mathscr{P}_{tot}$ accounts for the average velocity of the ACEO flow, L_{el} is the extent of the electrodes along the channel, L_{tot} the total length of the channel and v_{aceo} the velocity generated on the electrodes. The higher the number of electrode pairs that are patterned along the channel, the larger the average velocity, and flow-rate, at the outlet will be. The design choice of maximising the ratio L_{el}/L_{tot} to increase the generated flow-rate is only limited by the increment of the current consumption, which is proportional to the total number of electrode pairs.

Flow recirculation

Another geometrical effect is that the external connections can induce flow recirculation within the pumping channel, when the outlet is smaller than the main channel. This effect can be explained by looking at the hydraulic resistances in the system. If the outlet is smaller than the channel, its hydraulic resistance will be larger and a portion of the liquid will circulate back in the upper part of the channel, where it encounters a smaller resistance.

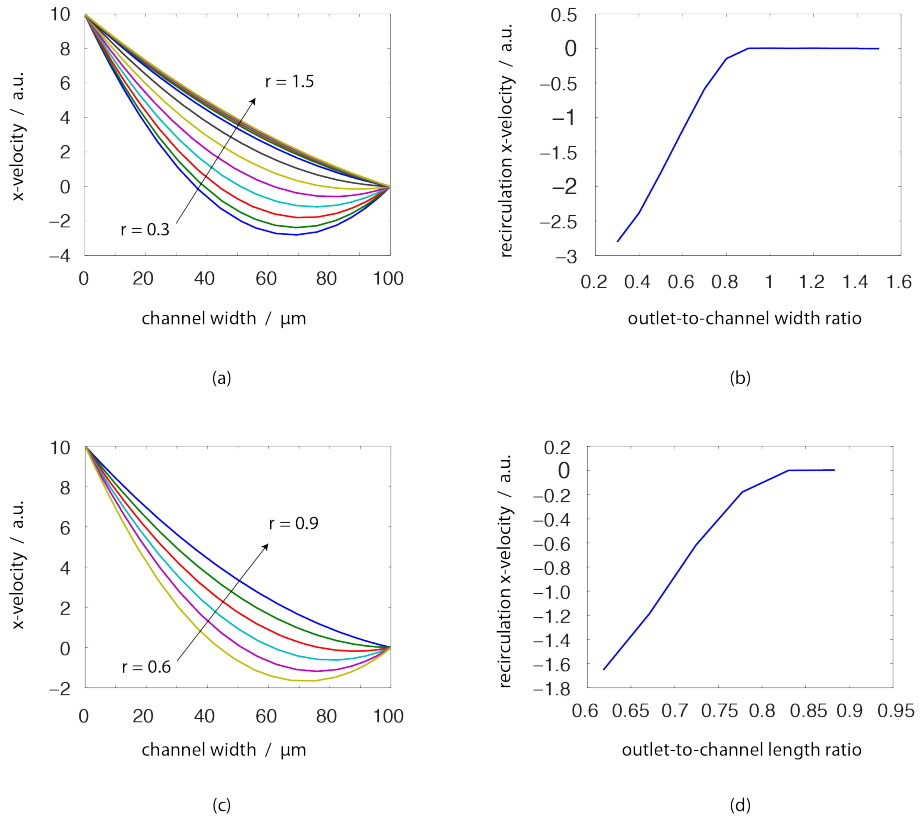

Figure 3.13: Simulated velocity profiles in the channel above the electrodes. The dependence on the ratio between the width of the channel and outlet (a,b) as well as on the ratio between the length of the channel and outlet (c,d) are shown.

Results of COMSOL simulations, shown in Figure 3.13 and carried out representing ACEO velocity generation as a non-zero slip-velocity on one side of the channel, clearly show this phenomenon. For given values of the total length of inlet and outlet, and of the length of the channel, it is possible to find the minimum ratio between the depths of the channel and the outlet that avoids recirculation, thus maximising the flow-rate that exits the system. As Figure 3.13 shows, for the structure considered in the simulations, the criterion to avoid recirculation is that the outlet should be at least 80% as large as the channel.

Preliminary observations that we carried out with basic ACEO prototypes also confirm this analysis of the importance of the relative size of the channel and the external fluidic connections, specially for devices with electrodes on only one side of the channel [146]. When electrodes are present on two or more walls, this effect becomes less important.

Formation of rolls and circular flow patterns

So far, we have modelled ACEO flows as ideal Couette flows, where the maximum velocity is generated on one, or more, sides of the channel. This approximation is good enough to describe multiple phenomena involving the general performances of the pump. Nevertheless, because the electrodes lie on the same plane, the shape of the applied electric field is circular [77] and the motion of the liquid immediately above the surface of the electrode will follow such a shape. Rolls that can be as wide as the size of the large electrode [98, 105] will form next to the walls.

When the large electrode is as wide or wider than the channel depth, the rolls will occupy the entire cross-section of the channel, above the electrode. At first, one might think that in such a configuration the liquid flow may be hindered. However, as Olesen *et al.* explain [147], the vertical confinement of the ACEO flow should result in an increase of the mean velocity in the portion of the channel free of electrodes.

3.7 Electrical models for ACEO

As has been said, electro-osmotic pumping is based on the force generated by the application of an electric field to a layer of charges. While in DCEO the applied potential gives an electric field that falls entirely on the ions of the electric double layer, in ACEO only a part of the applied field exerts a force on the EDL [135], depending on the overall impedance of the device. The optimal frequency at which the device should be operated will also depend on the impedance of the system. It is therefore important to understand how the properties of the system influence such an attribute.

In response to the oscillations of the applied AC potential, the thickness and charge distribution of the EDL will indeed change over time. Nevertheless, it is possible to define an electric model at a specific instant, when the EDL is fully developed. In such conditions, the double

layer can be considered as a capacitor and the ACEO force will be proportional to the potential drop across such a capacitance. We can also consider the bulk of the liquid as a circular resistor going from one electrode to the other, as suggested in Brown's work [136], to derive the model of the system that is illustrated in Figure 3.14. This is the simplest approximation, as it only accounts for the phenomena that occur within the channel, and the values of the specific capacitance and resistance are given by [136]

$$C_{EDL} = \frac{\epsilon}{\lambda_D} \tag{3.14}$$

and

$$R_{bulk} = \frac{\pi(L+S)}{2\sigma\sqrt{LS}} \left[\ln \frac{L+G+S}{G}\right]^{-1}, \tag{3.15}$$

where L, G and S are respectively the widths of the large electrode, the gap and the small electrode.

If such a simple model can be effective at describing the interactions within the channel, it fails to describe the behaviour of the complete system. As Gregersen *et al.* pointed out [144], a more complete model should account for the charging resistance of the EDL, arising from the injection of current due to the electrochemical reactions at the electrode. It must also include the intrinsic resistance and the mutual capacitance of the electrodes, and may include the impedance of the external elements connected to the pump (e.g. cables and instruments), as illustrated in Figure 3.15. The simulations of the two models for a solution of KCl at 0.01 mM

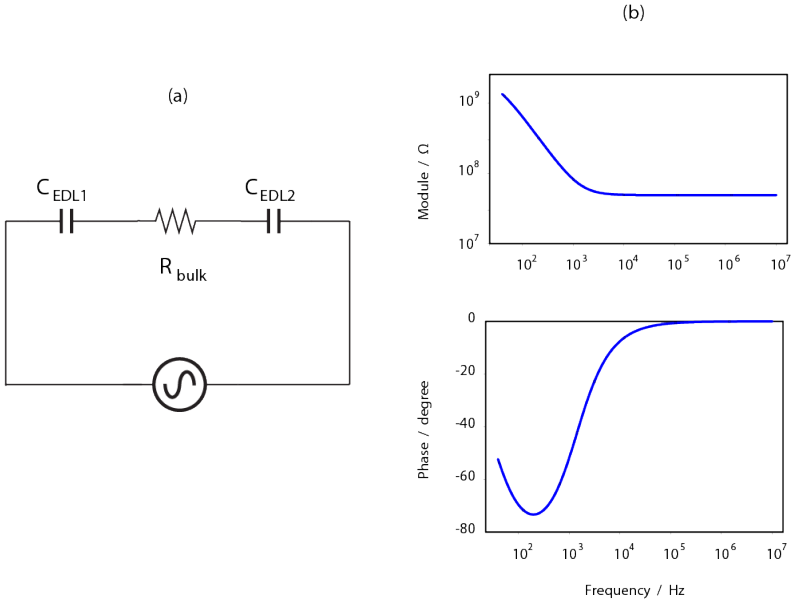

Figure 3.14: Equivalent electric circuit for a pair of asymmetric electrodes in contact with an electrolyte solution (a), according to [136], and total impedance of the circuit (b) simulated, for a solution of KCl at 0.01 mM, with the parameters given in Table 3.3.

show that the effects of the added elements only intervene at very high frequencies, which are normally not used in AC electro-osmosis.

The electric models of the ACEO pump help understanding the behaviour of the system and show the influence of the electrodes and of the external connections on the functioning of the device. The impedance of elements external to the device can shift the optimal pumping frequency. Moreover, according to the relative importance of the impedances in the circuit, at a given frequency, there will be a different potential drop on the EDL and therefore a different value of the ACEO force.

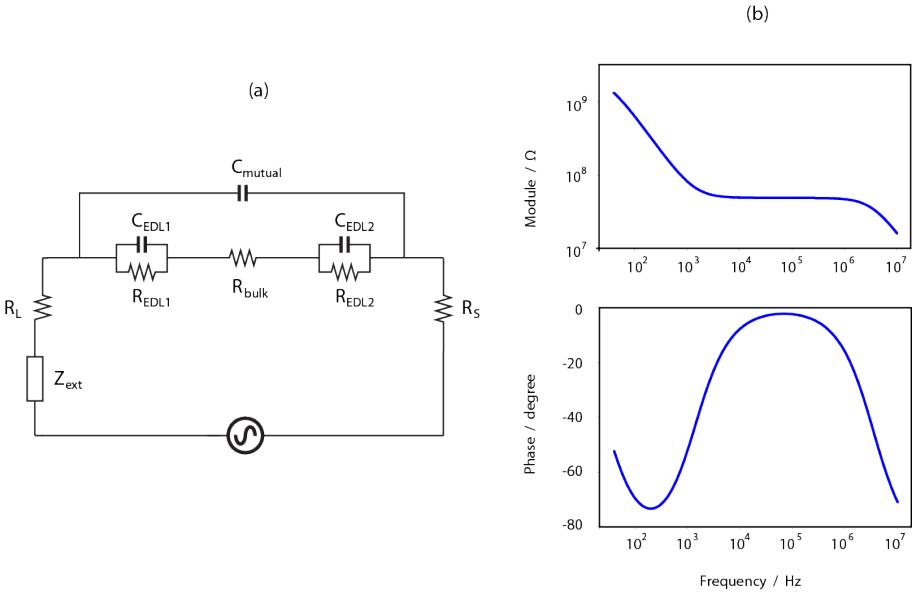

Figure 3.15: Electric model of ACEO electrodes, accounting for the EDL charging resistance as well as the intrinsic impedance of the electrodes (a), according to [144], and total impedance of the circuit (b) simulated with $Z_{ext} = 0$, for a solution of KCl at 0.01 mM, with the parameters given in Table 3.3.

Table 3.3: Parameters used for the simulation of the equivalent circuits presented in Figure 3.14 and Figure 3.15. All values were computed from the standard properties of solutions, water and metals, as reported in [134].

Quantity	Symbol	Value
Liquid bulk resistance	R_{bulk}	49 $M\Omega$
Pt electrode resistance	$R_L + R_S$	80 Ω
Large electrode EDL capacitance	C_{EDL1}	6.5 pF
Large electrode EDL charging resistance	R_{EDL1}	750 $M\Omega$
Large electrode EDL capacitance	C_{EDL2}	3.9 pF
Large electrode EDL charging resistance	R_{EDL2}	1.5 $G\Omega$
Electrode mutual capacitance	C_{mutual}	940 aF

3.8 Conclusion: the important parameters

Exploring the theoretical aspects of AC electro-osmosis has allowed thorough understanding of the challenges and opportunities that this technique of pumping liquids offers. Using alternating fields eliminates the issues connected to electrolysis and gas generation within the pump. If, on one hand, the buffer concentration has a strong influence on the formation of the double layer and the pumping performance of the device, on the other there is much room for the improvement of the generated flow-rate through the design of the geometry of the device. The efficient functioning of ACEO pumps will also be influenced by the intrinsic impedance of the electrodes and of the surrounding electric circuit. Using insulating substrates and good conducting materials for the electrodes will limit undesired effects.

A careful design of an AC electro-osmotic pump shall consider and account for:

- the width-ratio of the electrodes (Small:Gap:Large), which will determine the distribution of the electric field and the ACEO force in the channel;
- the perimeter of the channel covered by electrodes ($\mathscr{P}_{el}/\mathscr{P}_{tot}$), which influences the average velocity over the cross-section above the electrodes;
- the length of the portion of the channel having electrodes (L_{el}/L_{tot}), which impacts the liquid velocity in the portions of the channel without electrodes;
- the total power consumption of the device, which depends on the total extent of electrodes in contact with the liquid;
- the size of the inlet and outlet connections with respect to the channel, which can determine the recirculation of the liquid;
- the choice of the materials for fabrication, which influence the impedance of the system and the effectiveness of the device.

The following chapters will deal with the fabrication and characterisation of AC electro-osmotic pumps with electrodes patterned on one, two or all sides of the channel. Design choices will be made and justified in the light of the theoretical considerations developed in this chapter.

4 Experimental Methods

Precisely defining the methods that one follows in designing and conducting experiments is of primordial importance. Not only does it allow tests and analyses to be carried out in the most accurate fashion, but it also enables the scientific community to repeat and verify the results of those investigations. Furthermore, the comparison of the performances of two or more devices can only be meaningful when an appropriate and common frame is set, specifying the quantities that one refers to as well as the experimental conditions in which such quantities are measured.

4.1 Introduction

Characterising the performances of a micropump means measuring the properties of the flow that it generates, as well as its power consumption. A complete characterisation should include:

- the maximum flow-rate Q_{max},
- the equivalent maximum pressure capability Δp_{max},
- the power consumption W_{el},
- the power-conversion efficiency η_{conv}.

Some of these properties can be measured directly in simple ways, while others are more effectively evaluated using theoretical relationships. Important information also comes from the measurement of the electrical impedance of the device and allows us to relate its fluidic performance to the intrinsic properties of the system constituted by the pump and the liquid. For the devices presented in this thesis, only the impedance of the system, the current flow and the liquid velocity in the pumping channel have been measured directly. All other relevant quantities have been deduced from these three measurements, drawing on the theory of microfluidics.

More specifically, given the measured value v_{ave} of the average velocity in the channel in conditions of zero backpressure, and the data of the geometry, i.e. the area of the cross-section S and the hydraulic resistance R_{hyd}, the flow-rate and pressure capability of the pump can be obtained through Equations 2.1 and 2.2. On the other hand, given the known value V_{rms} of the applied AC potential and the measured current flowing in the system I_{rms}, the power consumption is expressed by

$$W_{el} = V_{rms} \cdot I_{rms} \tag{4.1}$$

and the conversion efficiency can be computed using Equation 2.4. As the reviews of the state of the art and theory in the previous chapters have shown, flow generation in an electro-osmotic micropump strongly depends on the liquid to be actuated. It is therefore important to clearly state the composition of the buffer solutions used for the tests. This is the first topic that will be discussed here.

The following sections will cover the measurements of the impedance of the electrodes and the power consumption of the pumps, and describe the devices designed for this specific purpose, along with the instrumentation that was used. Finally, the last section will focus on the requirements to measure the generated liquid velocity. The strategies and setups used for the experiments will also be presented.

4.2 Sample solutions

All measurements were carried out with KCl solutions. Using a simple binary salt has the advantage of simplifying the theoretical computations. Moreover, such a molecule can only dissociate as $KCl \rightleftarrows K^+ + Cl^-$ and allows the concentration of positive and negative ions in the solution to be controlled precisely. Cl^- ions may undergo unwanted reactions with the electrode metal, but in normal working conditions the effect is neutralised by the AC potential.

Experiments were conducted with solution concentrations covering a wide range, from 0.01 mM up to 10 mM. As Table 4.1 shows, the mass of salt needed to directly prepare 100 mL of the solutions may be very small and can hardly be measured with good precision on a laboratory scale. Therefore, we first prepared 200 mL of a solution of KCl at 10 mM, which required 149.1 mg of salt, that were measured with a microbalance and diluted in DI water.

Table 4.1: Mass of KCl (74.55 g/mol) required for 100 mL of solution at a concentration c_n.

Concentration	$c_0 = 10\ mM$	$c_1 = 1\ mM$	$c_2 = 0.1\ mM$	$c_3 = 0.01\ mM$
Salt mass	74.6 mg	7.5 mg	745.5 μg	74.6 μg

Table 4.2: Preparation of the solutions at concentrations c_1 to c_3.

c_1	c_2	c_3
10 mL c_0 + 90 mL DI H_2O	10 mL c_1 + 90 mL DI H_2O	10 mL c_2 + 90 mL DI H_2O

Table 4.3: Measured conductivities of the prepared solutions before and after the addition the microbeads. All values of conductivity are given in $\mu S/cm$.

	KCl	KCl + beads
0.01 mM	2.5	18.7
0.1 mM	15.3	24.4
1 mM	147.1	161.6
10 mM	1416.0	1473.0

The buffer at $c_0 = 10\ mM$ was used as the base solution to prepare the less concentrated ones: 100 mL of solution at the concentration c_n were obtained by addition of 10 mL of the solution at the concentration c_{n-1} to 90 mL of DI water, as summarised in Table 4.2.

Finally, microbeads were added to the preparations in order to visualise the flow generated in the pumps. We used polymer microspheres from Molecular Probes, with a carboxylate-modified surface (F-8888). Choosing the size of the beads is crucial: they should be large enough to scatter light and be easily distinguishable from the background, in order to track their movements, but small enough to avoid unwanted interactions with the walls or clogging of the channel [148]. Bead sizes in the order of a few percent of the hydraulic diameter of the microchannel are usually considered to be suitable for the purpose [149]. The particles that we used were 2 μm in diameter.

Such microbeads are stored in a buffer of NaN_3 at 2 mM, which corresponds to a fairly high concentration of ions, compared to the test solutions that were prepared, and can significantly alter the electrical conductivity and other properties of the samples. Therefore, the volume of beads that is added to the test buffers should be small enough to avoid such effects, while being sufficient to allow a comfortable visualisation of the generated flow. We found that 20 μL of beads in 3 mL of KCl solution was a good compromise; this corresponds to a density of about $3.2 \cdot 10^7\ cm^{-3}$ of microbeads suspended in the test buffer. The conductivity of the sample solutions is nevertheless still modified by the addition of the beads, as Table 4.3 shows. The overall preparation of the solutions for the tests can be summarised as follows:

1. prepare 200 mL of KCl at 10 mM;
2. dilute the buffer at 10 mM into solutions at 1 mM, 0.1 mM and 0.01 mM;
3. mix 20 μL of beads to 3 mL of each of the prepared solutions.

4.3 Electrical measurements

Electrodes for AC electro-osmotic micropumps are built by replicating the basic design of one electrode pair a certain number of times. From an electrical standpoint, this is equivalent to the parallel connection of identical elements with the same impedance. Even though it

would be wrong to consider that such a parallel connection behaves exactly as one single element, considering that they will have a very close qualitative behaviour is a reasonable approximation. The characterisation of the impedance of the pumps has therefore been carried out on special prototypes with only one pair of electrodes. Such an approach simplifies the interpretation of the measurements and allows the analysis of the properties of the basic system constituted by one pair of metal electrodes in contact with the electrolyte solution.

Impedance of one electrode pair

Single-pair prototypes were characterised prior to the measurement of the fluidic performances of the pump, as the information about the impedance of the system provides an important insight into the parasitics potentially caused by the fabrication process, as well as an indication of the optimal pumping frequency of the device. Since here we only focus on the electrical behaviour of the prototypes, the impedance was tested with KCl buffers prepared following the procedure described in Section 4.2, but without the addition of microbeads.

Impedance measurements (module and phase) were carried out using the Agilent 4294A Impedance Analyser, connected to the single-pair prototype with crocodile clip-connectors, as shown by the diagram in Figure 4.1. Fluidic inlet and outlet should be connected together to keep the liquid still within the pump, and proper insulation must be provided to separate the prototype from metallic surfaces or objects that might contact the electrical inputs of the device under test and alter the measurement. Buffer solutions were tested in the order of increasing salt concentration and the prototypes were rapidly rinsed with DI water between successive tests. After the most concentrated buffer had been used, the device was rinsed thoroughly with DI water, in order to avoid salt deposits on the channel walls and the electrodes.

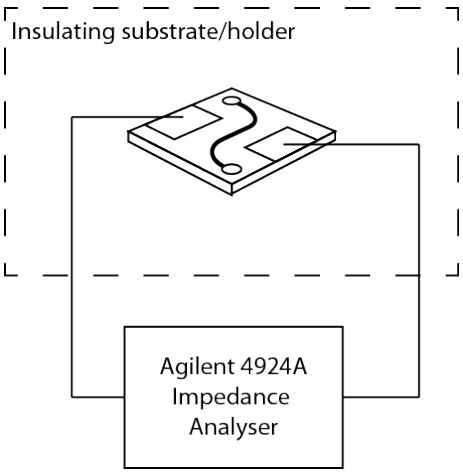

Figure 4.1: Diagram representing the setup used for the characterisation of the impedance of the prototypes with only one electrode pair.

The test protocol for the measurement of the impedance can be summarised as follows:

1. fill the single-pair prototype with the test buffer and connect inlet and outlet together;
2. connect the electrodes to the impedance analyser;
3. ensure electrical insulation of the device from the surrounding environment (e.g. by using a teflon support);
4. measure the module and phase of the impedance for frequencies smaller than 100 kHz;
5. empty the device and rinse it with DI water;
6. repeat the procedure with buffers of increasing concentration;
7. rinse the prototype thoroughly with DI water after the last measurement.

Power consumption

Further electrical measurements were performed on complete AC electro-osmotic micropumps with arrays of asymmetric electrodes. It is important to monitor the current consumption of the devices during operation, since such data provide information concerning the power consumption of the ACEO prototypes and may also be used as an indicator of the amount of electrochemical reactions occurring at the electrodes. For this test, the prototypes were powered with a Hewlett-Packard 33120A function generator and the RMS value of the current was measured with an Agilent 34411A digital multimeter, which was connected in

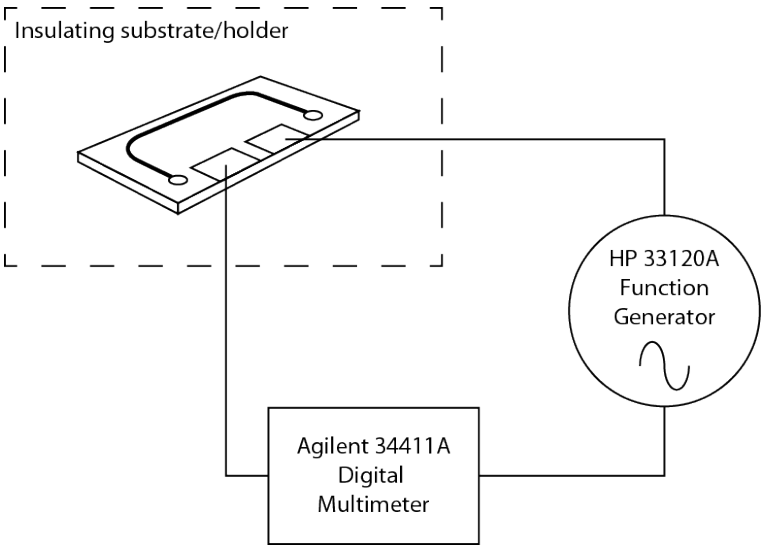

Figure 4.2: Diagram representing the setup used to measure the RMS value of the current flowing in the complete ACEO prototypes.

series to the micropump and the function generator, as shown in Figure 4.2. Again, care must be taken to ensure the electrical insulation of the device under test. The power consumption was measured simultaneously with the characterisation of the fluidic performance of the micropump.

4.4 Fluidic characterisation

A complete characterisation of the fluidic behaviour of the micropumps must include the evaluation of the generated flow-rate and pressure. As explained previously, only the liquid velocity generated by the pump was directly measured for the prototypes presented in this thesis. This was done by recording the motion of microbeads in the channel of the pump on a video and evaluating their velocity with a computer program. In order to obtain reliable and repeatable measurements, it is important to perform the tests at constant temperature and stable ambient conditions. Moreover, the absence of vibrations or other sources of motions that can influence the movement of the beads in the pump guarantees a correct interpretation of the experiments, and the observation of the fluid motion at a fixed point allows the comparison of different data sets.

Experimental setup and preparation of the devices

All experiments were carried out with the test solution described in section 4.2 and the system observed under an optical microscope with a magnification of 20 times. The motion of the microbeads in suspension in the channel was recorded either with a uEye SE USB digital camera from iDS Imaging Development Systems GmbH (Obersulm, Germany) or with the Phantom V210 high-speed camera from Vision Research (Wayne, NJ, USA). This optical system was set up on a stabilised table in a laboratory room with no windows and a stable temperature of 23 $^{\circ}C$.

The chips to test were placed and fixed upside-down on a custom-made holder and the observations carried out from the rear, with illumination coming from the bottom of the setup, as illustrated in Figure 4.3. The position of the chip was such that the camera recorded the motion of the beads in a portion of the channel free of electrodes. This choice was inspired by the work of Gregersen *et al.* and guarantees that the particles move under the exclusive influence of the generated flow-rate and that no electrical force acts on them [144].

We set up the electrical system for the tests on the same stabilised table as the microscope. The configuration included a Hewlett-Packard 33120A function generator and an Agilent 34411A digital multimeter, which were both connected in series to the ACEO micropump. An adapter was used to connect the coaxial output from the signal generator to the electrical contacts on the pump and the inputs of the multimeter.

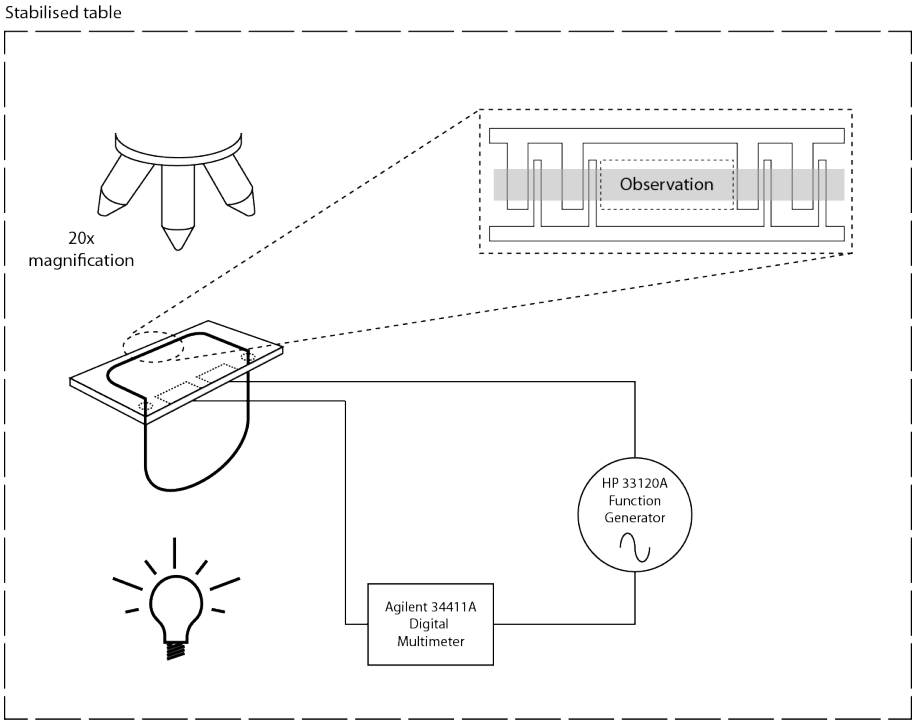

Figure 4.3: Diagram representing the setup used for the characterisation of the flow generated by the ACEO micropumps. The motion of the fluid and the RMS value of the current were acquired at the same time.

Test protocol

Before connecting the prototypes to the characterisation setup, the chips were rinsed with DI water and filled with the test buffer by means of a micro syringe, which can push the liquid into the channel at a very small pressure, avoiding the formation of air bubbles that could be trapped within the device and impede the flow of the liquid. After filling the ACEO micro pumps with the test buffer, we connected the fluidic inlet and outlet together with soft tubes. This expedient guarantees that the pressure at the inlet and outlet is the same and the pumps are tested in conditions of zero backpressure.

The devices were tested with the buffers discussed in Section 4.2 and its behaviour characterised to verify the dependence on both the magnitude and the frequency of the applied AC potential. First, the magnitude was kept constant at 3 V_{pp} (we found that with such a voltage, the pumps generated well-detectable fluid motion), while the frequency was varied in a range of a few decades around the optimal value estimated with the simulations shown in Section 3.4. The frequency was then set at the optimal value and the voltage varied between 1 V_{pp} and the value at which electrolysis started occurring, usually around 5 V_{pp}. Because an arbitrary periodic signal can be defined as the sum of sinusoidal functions (Fourier series), we tested our prototypes only with sinusoidal signals.

Buffers at low concentrations were tested before the more concentrated ones in order to minimise possible variations of the salt concentration due to salt deposits on the channel walls. Each time the parameters of the applied potential were changed, the pump under test was emptied, rinsed with DI water, dried with nitrogen and refilled with the test buffer. Such a procedure ensures that the microbeads are uniformly distributed in the channel and that the test is performed, for each set of parameters, under the same experimental conditions. The protocol followed for the fluidic characterisation of the pumps can be summarised as follows:

1. rinse the chip with DI water;
2. dry with N_2;
3. fill the prototype with the test buffer and connect inlet and outlet together;
4. place and fix the micropump on the holder for the microscope;
5. connect the electrodes to the function generator and the multimeter;
6. adjust the position of the pump under the microscope;
7. adjust the focal point of the microscope to be in the middle of the channel;
8. record the motion of the beads and the current consumption;
9. repeat the procedure with all the combinations of signal parameters and buffers;
10. rinse the micropump thoroughly with DI water after the last test.

Evaluation of the velocity by particle image velocimetry

The recorded videos were then computer-processed to obtain the relevant information about the fluid velocity generated by the pumps. Particle image velocimetry (PIV) is the strategy of using particles in suspension to visualise the motion of a fluid that would otherwise be invisible. As long as no force other than the flow of the liquid is exerted on the particles, such an approach also allows the estimation of their velocity, which can be considered equal to that of the liquid. For a given video, after defining the position and scaling of the reference axes, software like the Tracker [150] can follow the trajectory of the particles and evaluate their position and velocity in each frame of the movie. In order to speed the process up, it is usually necessary to enhance the contrast and reduce the size of the video files with video-processing software.

Since the microscope was focused in the middle of the channel and the camera recorded the motion of the beads far away from the electrodes, we observed a Poiseuille (or pressure-driven) flow [1] in the region where its velocity is maximum, as shown in Figure 4.4. Therefore, the Tracker evaluates the peak velocity of such parabolic flow. This information is sufficient to deduce the average velocity over the cross-section of the channel and the flow-rate that

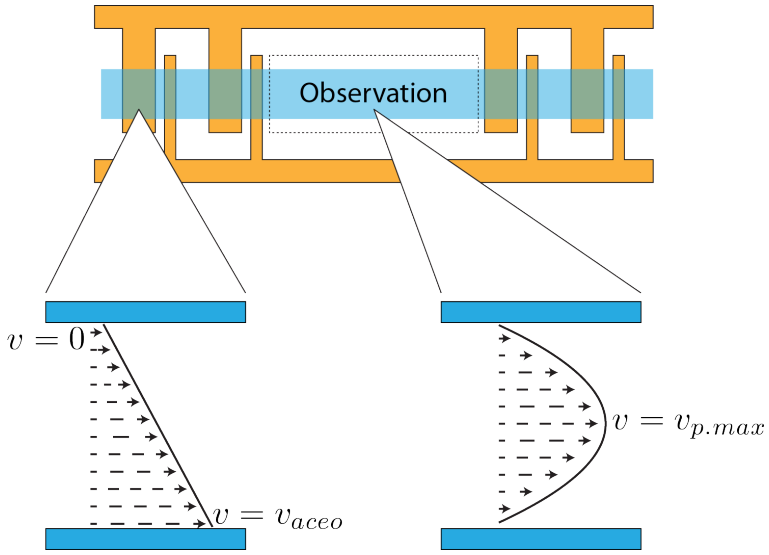

Figure 4.4: View of the velocity profiles generated by the ACEO pumps in the regions above (left) and distant from (right) the electrodes. The microscope being focused in the middle of the channel, PIV allows the estimation of the velocity $v_{p.max}$.

the pump has generated. It can also be used to estimate the value of the velocity generated on the surface of the electrodes [144]. After extracting the relevant information from each recorded video, the data were imported into Matlab [140] and processed using the scripts reported in Appendix A.4. We plotted the graphs of the dependence of the generated velocity on the frequency and magnitude of the applied signal, and evaluated the velocity increase obtained with the improved two-side- and all-around-electrode micropumps. The procedure to complete the characterisation of the pumps can be summarised as follows:

1. enhance contrast and reduce size of the recorded videos;
2. import the videos into the Tracker;
3. track the motion of the particle and save .txt files;
4. import data into Matlab;
5. compute errors;
6. plot the relevant graphs and statistics.

Uncertainty on the velocity measured with the uEye camera

Each analysed video is used to track the motion of a bead across the whole width of the frame. Given the framerate Fr, the Tracker evaluates the position x of such a bead in every frame,

then computes the velocity in the nth frame as

$$v = (x_{n+1} - x_n) \cdot Fr, \tag{4.2}$$

where we have used $Fr = \Delta t^{-1}$. The Matlab scripts used for data processing import the values of the velocity from the Tracker and estimate the mean velocity as

$$v_{mean} = \frac{1}{N} \sum_{n=1}^{N} v_n, \tag{4.3}$$

where N is the total number of frames in the video. The sources of uncertainty in such a procedure lie in the evaluation of the time elapsed between two frames and of the position of the bead, and are transmitted to the measured measured velocity according to the rules on the propagations of uncertainties [151].

The framerate for the experiments is automatically set by the camera at Fr = 21.7 fps. Because it varies slightly over time, as some frames are dropped due to bad acquisition, we consider an uncertainty on the framerate δFr = 1 fps, corresponding to a relative error $\sigma_{\mathrm{Fr}} = 4.6\%$. Since the time is computed as the number of elapsed frames divided by the framerate, the relative error on the time is also $\sigma_t = 4.6\%$.

On the other hand, the uncertainty on the position of the bead depends on the resolution of the camera. According to the calibration of the microscope, one pixel at a magnification of 20x corresponds to $\delta x = 0.3226\ \mu m$. The uncertainty on the difference $\Delta x = x_{n+1} - x_n$ is then $\delta_{\Delta x} = \sqrt{\delta_x^2 + \delta_x^2} = 0.4549$. The relative influence of such an error on the velocity measurement should be estimated with respect to the whole width of the frame, hence we consider $\Delta x = 1024$ pixels $\cdot\, 0.3226\ \mu m$/pixel $\approx 330\ \mu m$, since the velocity is evaluated using Equation 4.3. The relative error on Δx is then $\sigma_{\Delta x} = \delta_{\Delta x} / w_{frame} \approx 0.1\%$. We can compute the relative error on the velocity v_{mean} evaluated according to Equation 4.3 as

$$\sigma_v = \sqrt{\sigma_{\Delta x}^2 + \sigma_t^2} \approx 5\% \tag{4.4}$$

and we will use this value for the experimental analysis presented in the following chapters.

4.5 Conclusion: a consistent comparison of performances

The precise definition of the procedures to follow for the characterisation of innovative devices and the comparison of their performances to previously investigated approaches ensures that the analysis of the results presented in this thesis will be reliable and consistent. The protocols that have been defined were strictly respected for this research. The outcome will be assessed both with respect to the goals that were given at the beginning of the project, and relative to the performances of other ACEO micropumps reported in the literature.

A direct comparison of the generated flow-rates and pressures may be biased by geometrical

reasons, such as the dimensions of the device, which do not depend on the effectiveness of the electrode design. One effective way of comparing the performances of different devices is to look at the absolute liquid velocity they can generate. However, this information cannot always be clearly extrapolated from the publications.

Because the indication of the exact point in the device where the velocity was measured may be missing and since there can be huge variations of this quantity throughout the device, the comparison of the average velocity over the cross-section of the channel is usually a more consistent approach to assessing the performance of a micropump.

Nevertheless, much research reports innovative designs that enhance the performance of the device. It will be interesting to compare the relative improvement that different solutions provide. This approach also avoids the issue that for similar designs and fabrication techniques, large disparities in the generated flow velocity can arise from differences in the width-ratio of the electrodes.

In order to provide the reader with the most meaningful analysis of the measured performances, the next chapters will cite results from previously-published work according to the generated average velocity (whether stated clearly or deducible from the flow-rate). Should this information not be available, the generated fluid velocity (when clearly identifiable), or the flow-rate and pressure will be cited.

5 Planar AC Electro-Osmotic Micropumps

Cleanroom fabrication of planar structures is the easiest way of defining micrometre-size metal patterns and the most straightforward method of implementing AC electro-osmotic micropumps. Simple device structures enable us to gain important insights into the functioning of the devices and the influence of AC electro-osmosis on the liquid that it pumps. Moreover, planar designs also allow a preliminary experimental validation of the idea that increasing the extent of the electrodes around the channel will induce an improvement in the pumping performance.

5.1 Introduction

Simple prototypes provide an effective way to characterise many aspects of the experimental behaviour of AC electro-osmotic micropumps. Because the fabrication process is relatively rapid, it is possible to implement different designs and produce devices made with different materials in a reasonable time. The objective of this chapter is to test the behaviour of AC elecro-osmosis and to prove that the average generated velocity increases when the extent of the electrodes around the channel is increased, as well as to assess the suitability of non-conventional electrode materials for AC electro-osmosis.

Planar prototypes are a good way of implementing such experiments. In fact, one-side-electrode (1SE) and two-side-electrode (2SE) prototypes can be obtained starting from the same substrates onto which electrodes are patterned, as the following sections will show. While devices with electrodes on only the bottom side of the channel (1SE) are useful to observe the basic flow patterns that are generated, prototypes with electrodes on both the top and bottom sides (2SE) can generate larger velocities and provide a means of observing amplified phenomena.

This chapter will discuss the fabrication and characterisation of ACEO prototype micropumps with electrodes patterned on one and two sides of the channel. First, the impedance of the basic electrode pair will be considered as a function of the buffer concentration, and the

pumping performance of complete micropumps will be presented for dilute solutions (unless stated otherwise, all the results presented in this chapter were obtained using KCl solutions at 0.01 mM). Second, we will analyse the dependence of the generated flow on the frequency and magnitude of the applied AC potential, and show that the velocity of the liquid within the pump rapidly oscillates over time, whilst having a constant average value. Finally, the performances of one-side and two-side micropumps will be compared, in order to validate the basic assumption of this thesis.

5.2 Fabrication of the prototypes

Electrodes for the devices analysed in this chapter were fabricated by lift-off on Pyrex wafers. Starting from the same substrates with electrodes, the assembly of 1SE and 2SE prototypes differ in the way microfluidic channels are realised and bonded to the substrate with electrodes. Yet when the chips are ready, the strategies to provide them with electrical and fluidic connections are the same for both families of pumps.

5.2.1 Design of the devices

As discussed in Chapters 3 and 4, the design of the ACEO prototypes must take several parameters into account. The size and shape of the pumping channel influence the hydraulic resistance of the device, which in turn defines its pressure capability, as well as the area of the cross-section, which determines the generated flow-rate. A long channel with a small cross-section will be able to stand larger backpressures, at the cost of having a lower flow-rate. On the other hand, a large cross-section will decrease the pressure capability, while improving the generated flow-rate.

We would also like the rolls generated above the electrodes by AC electro-osmosis not to interact with the channel. Since such rolls can be as wide as the large electrode, another constraint for the design is that the channel must be larger than a few times the electrode width.

Concerning the electrodes, their size and the ratio of their widths are the main parameters that must be chosen. As shown in Section 3.4, at a constant width-ratio, smaller electrodes generate larger velocities. Whereas a large aspect ratio should also guarantee better performances, the width of the small electrode is limited by the resolution of the lithographic system and the large electrode is limited by the size of the rolls, as mentioned above.

In the effort to address the problem of the generally low pressure capability of ACEO pumps, the channel should be fairly long and the cross-section small, although this can be detrimental to the flow-rate generation. Considering that this last problem may be solved later by connecting several channels in parallel, it seems reasonable to design a channel of about 3 cm in length and with a cross-section of 100 μm by 100 μm. In turn, the height of the channel sets the

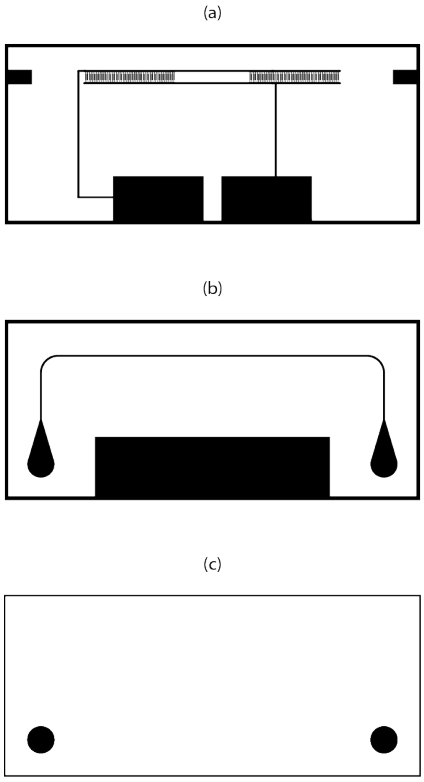

Figure 5.1: Lithographic masks for the fabrication of ACEO micropumps. The mask in (a) defines the array of asymmetric electrodes (large: 25 μm, gap 10 μm, small 15 μm). The mask in (b) is used to pattern the channel (about 3 cm long and 100 μm wide). The mask in (c) determines the shape and location of the access holes to the channel.

dimensions of the electrodes. Since we want to keep the same electrode design for electrodes that will be patterned on deep 3D surfaces, and in order to ease the lithographic process, the electrode widths should not be too small. A pattern constituted by a large electrode of 25 μm and a small one of 15 μm, separated by a gap of 10 μm seems a good choice. Such a basic pair is repeated 100 times along the channel with a spatial period of 100 μm. Figure 5.1 illustrates the designs of the channel and the electrodes, as defined on the masks for lithography.

5.2.2 Fabrication of the electrodes

Most publications report the use of gold as electrode material. They also observe a relatively strong interaction with the species in solution and a rapid degradation of the metal layer upon application of an electric potential [104]. Therefore, we consider that gold is not adapted to be used in a device designed for biomedical applications, where there should ideally be no interaction between the buffer and the electrodes. We chose platinum as the electrode material for the fabrication of our prototypes; such a metal is often used as an inert electrode in electrochemical cells [152] and guarantees that there will be little or no interactions with the buffer.

Another conductive material that may be of interest for ACEO prototypes is indium-tin oxide (ITO). Although ITO has a much smaller conductivity than platinum, it has the advantage of being transparent and allowing the observation, through the electrodes, of the phenomena occurring within the channel.

Both ITO and Pt were used for the fabrication of the micropumps presented in this chapter. Indium-tin oxide was deposited by sputtering, while the metal structures were obtained through the evaporation of a stack of a titanium adhesion layer and platinum, whose surface will be exposed to the liquid.

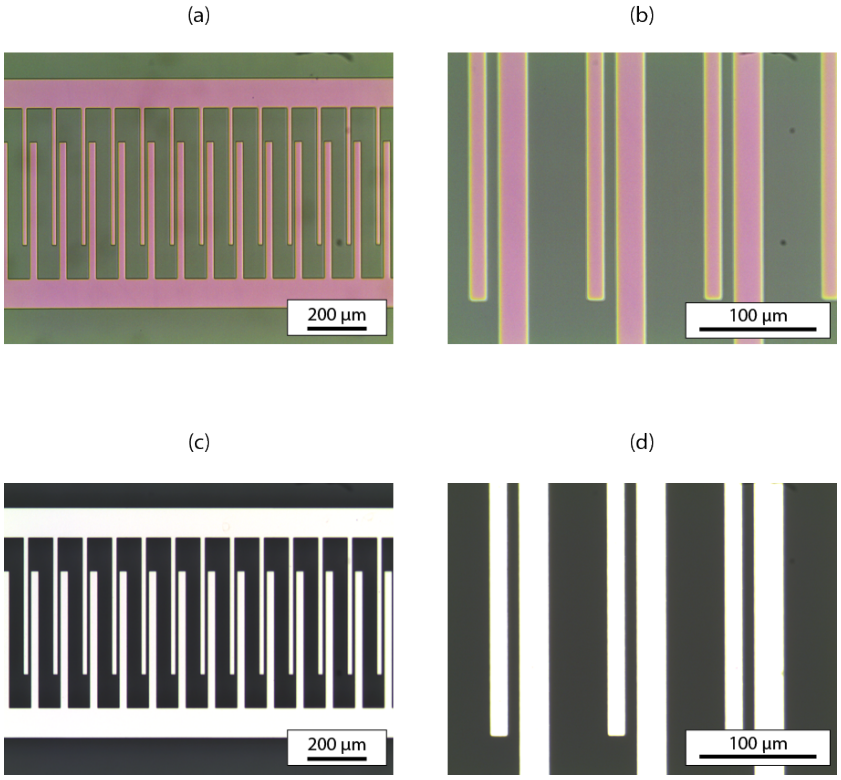

Figure 5.2: Fabricated electrodes after the lift-off process. ITO patterns are shown at a magnification of 5x (a) and 20x (b), along with Ti/Pt structures at 5x (c) and 20x (d) magnification.

The electrodes were realised by lift-off on Borofloat-33 Pyrex wafers, 500 μm in thickness, as illustrated in Figure 5.4 (steps 1-2). Prior to processing, the substrates were cleaned with a standard procedure including acetone, isopropanol, 100% nitric acid and deionised (DI) water. The lift-off process exploited image-reversal photoresist AZ5214 from AZ Electronic Materials (Stockley Park, UK), which has the advantage of being very easy to process as it is developed by AZ351B in a short time and is removed by acetone. Spin-coated wafers were illuminated once to transfer the pattern from the mask into the resist and a second time to obtain the image-reversal effect, before being developed.

Figure 5.2 shows pictures of the fabricated planar electrodes. ITO electrodes have a thickness of about 150 nm, while Ti/Pt ones are slightly thinner and measure only 120 nm. Processed wafers served as one side of the ACEO prototypes and were bonded to microfabricated channels to obtain the final devices.

5.2.3 One-side-electrode pumps

Among the wide range of possibilities for the fabrication of microchannels, using polymers is a very interesting option which reduces costs and usually allows for faster processing. Channels for one-side-electrode pumps were realised using UV-curable glue NOA81 from Norland Optical Adhesive (Cranbury, NJ, USA), which polymerises upon exposure to ultraviolet light. Such material is simple to handle and, in its polymerised form, presents a stable hydrophilic surface [153], which eases the process of filling the channels with liquid.

For the fabrication of the channels, a master mould was realised on a silicon substrate by deep reactive ion etching (DRIE). For this purpose, a laminated layer of dry photoresist (MX5050 from Dupont) acted as a 50-μm-thick etch mask, after being patterned by standard lithography. Such a master functioned as a mould for polydimethylsiloxane (PDMS), which in turn was used to cast the channels with NOA81 [154]. The intermediate step of fabricating a PDMS mould is necessary, because the UV-curable glue would stick on silicon and we would not be able to separate the structures after the polymerisation.

Prior to bonding the polymer chips to the substrates with electrodes, access holes to the channels were drilled in the chips made of UV-glue to be able to fill the device with the test solutions, and the chips cleaned with isopropanol and DI water. The electrode substrates were also cleaned with acetone, isopropanol and DI water. Both chips then underwent a short oxygen-plasma treatment to activate their surfaces. Finally, the channel and electrodes were aligned and bonded by putting them in contact and applying a light pressure (see Figure 5.4, step 3-1SE). Figure 5.3 shows pictures of the fabricated polymer channels and the bonded devices.

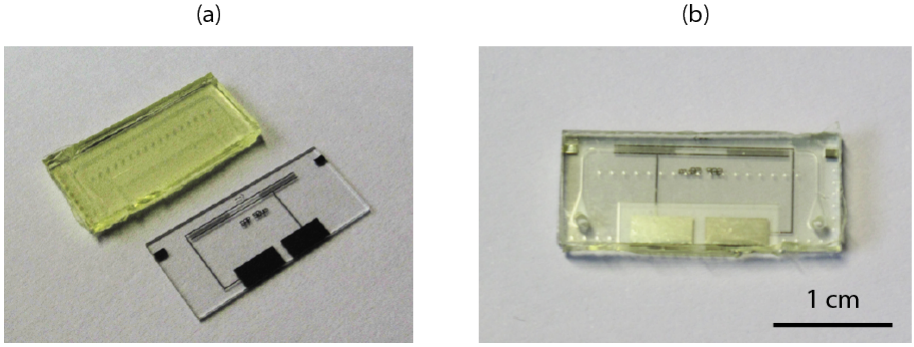

Figure 5.3: One of the fabricated microchannels in UV-curable glue is shown next to a glass chip with metal electrodes (a) and after bonding to the same chip (b).

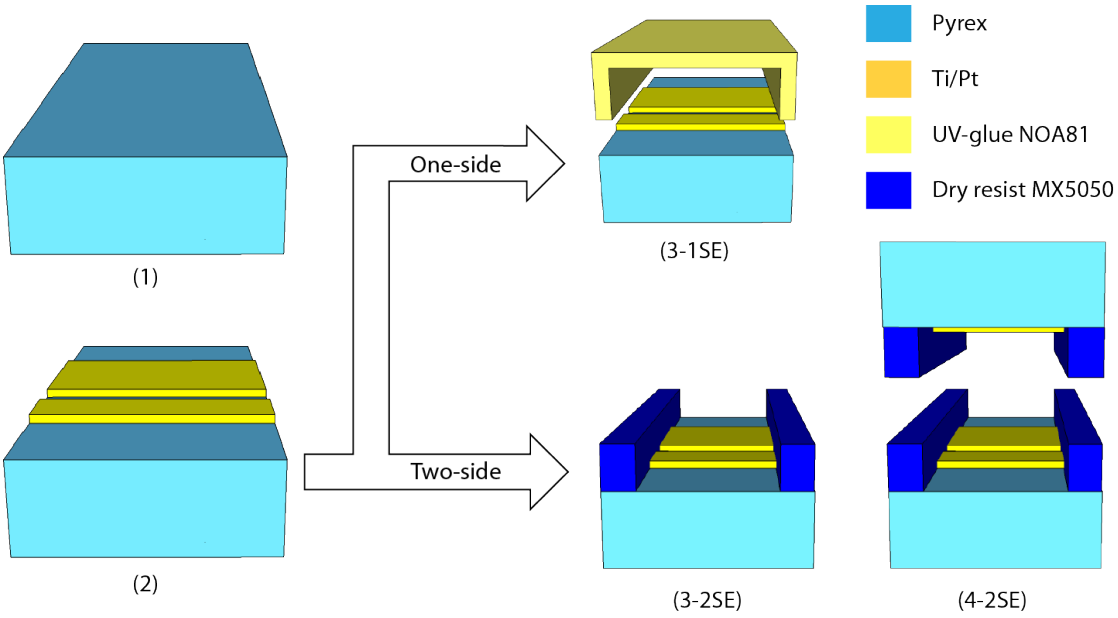

Figure 5.4: Fabrication process for the one-side and two-side prototypes. After patterning the electrodes (1,2), the one-side prototypes are realised by bonding a channel made of UV-glue (3-1SE) to the substrate with electrodes. The two-side devices are obtained by patterning channels into dry photoresist (3-2SE), then bonding together two structured wafers (4-2SE).

5.2.4 Two-side-electrode pumps

Prototypes with electrodes on two sides can be obtained by bonding together a first substrate with electrodes, a channel with two open sides and a second substrate with electrodes. Implementing such procedure with channels made of UV-curable glue requires the fabrication of very thin polymer chips (100 μm is the desired depth of the pumping channel), which are very delicate to handle. Moreover, because the top and bottom electrodes need to be aligned with a precision of a few tens of micrometers and the alignment and bonding should be carried out twice for the same chip, errors in the fabrication may be critical to the correct operation of the devices.

To address these issues and guarantee a good quality of the fabricated devices, the channel for the two-side-electrode micropumps was realised by patterning laminated photoresist with a thickness of 50 μm. For this purpose, the batch of wafers with electrodes was split into two groups: the first served as the bottom half of the devices, while access holes were opened in the second group by sandblasting. After that, the two groups were laminated with dry photoresist MX5050 from Dupont (Wilmington, DE, USA), onto which channels were defined by standard photolithography. Finally the wafers were aligned and put in contact with the MA6 Aligner from Süss MicroTec (Munich, Germany), and bonded with a home-made setup that heated the substrates to 120 $^{\circ}C$, whilst applying a force of about 1600 N for about 3 h, after which the wafers were left to cool down naturally. Patterning and bonding of the channels are illustrated in Figure 5.4 (steps 3-2SE and 4-2SE).

Compared to the fabrication of 1SE prototypes, this approach requires an additional lithographic step to open the access holes. However, it allows a much more precise alignment and rapid processing thanks to batch fabrication. Bonded wafers were diced before providing the single chips with electrical and fluidic connections.

5.2.5 Electrical and fluidic connections

The final processing step was the same for both kinds of prototypes. Stainless steel connectors from Distrelec (article no. 504239), which were 5 mm high and had a cross-section at the base of 0.34 mm^2, were glued on top of the access holes using 2-tone epoxy from Devcon (Danvers, MA, USA) with a process including two steps: first, very little glue was used to make the connector adhere to the substrate; second, after the glue had dried, a larger quantity was poured around the connector to ensure strong adhesion and good watertightness.

As for the electrical connections, they were realised using stripes cut from aluminium foils. These were either glued onto the contact pads of 1SE prototypes, or inserted between the two glass plates of 2SE devices at points where the laminated resist had been structured to leave free space. In both cases, Epotek H20E conductive epoxy from Epoxy Technology (Billerica, MA, USA) was used to secure the adhesion of the Al foils and a good electrical connection. Figure 5.5 shows the final devices, ready for the electrical and fluidic characterisation.

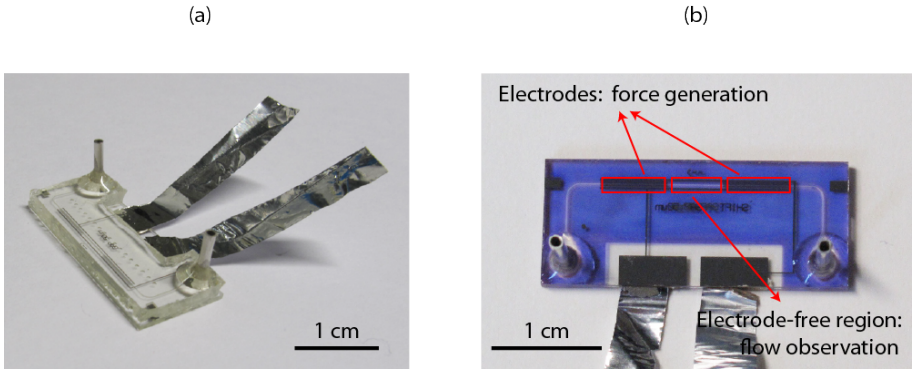

Figure 5.5: Fabricated one-side-electrode (a) and two-side-electrode (b) micropumps with electrical and fluidic connections. The regions of the channel where the fluid motion is generated and those where it is observed are highlighted in (b).

5.3 Electrical characterisation

Before proceeding to the characterisation of the flow-rate generated by the pumps, it is important to verify the electrical behaviour of the fabricated devices. We use the simulations of the impedance given in Section 3.7 for a KCl buffer at 0.01 mM as a reference to verify that no major parasitic effect is present. Moreover, impedance measurements also provide information about the power consumption of the devices. As detailed in Chapter 4, special

prototypes with only one pair of asymmetric electrodes were filled with KCl buffers at different concentrations and tested with an impedance analyser.

Dependence on the buffer concentration

We tested only one-side-electrode devices with Ti/Pt electrodes, to verify the evolution of the impedance with the concentration of the test buffer, as we consider that they constitute the most basic pumping unit and are representative of the whole group of fabricated devices. Figure 5.6 shows the measured module and phase of the impedance for 1SE devices and KCl buffer concentrations going from 0.01 mM up to 10 mM. The shape of the curves corresponds well to the theoretical model that has been given in Figure 3.15 and clearly shows that the impedance decreases as the concentration of electrolyte increases, which is reasonable since increasing the concentration of ions means increasing the conductivity of the solution. The solutions at 0.01 mM and 0.1 mM have similar impedances: as detailed in Chapter 4 such buffers have comparable conductivities, due to their very low electrolyte concentrations, and it is possible that their real concentration is less well-controlled than for more concentrated solutions.

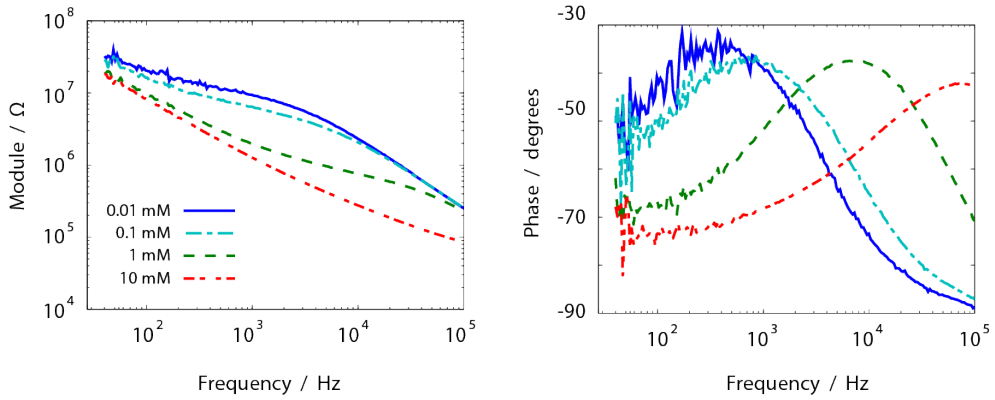

Figure 5.6: Measured impedance of one planar electrode pair in contact with a KCl buffer at different concentrations. The module (a) and phase (b) of the impedance are given.

On the other hand, the module of the impedance measured at 0.01 mM is larger than simulated, which is probably due to an underestimation of the liquid resistance. We can also observe that the non-resistive behaviour of the devices is influenced by the buffer concentration, in agreement with the fact that the capacitance of the double layer and the resistance of the liquid bulk change according to the concentration of ions.

One-side and two-side impedance

In order to evaluate the influence on the impedance of the extent of the electrodes around the channel, we considered 1SE and 2SE devices filled with a solution of KCl at 0.01 mM. The corresponding electrical measurements are shown in Figure 5.7. As expected, the impedance

of the 2SE prototypes is clearly smaller. As a matter of course, increasing the total surface of the electrodes facilitates current flow by increasing the available cross-section of the conductor, and therefore induces a decrease in the total impedance.

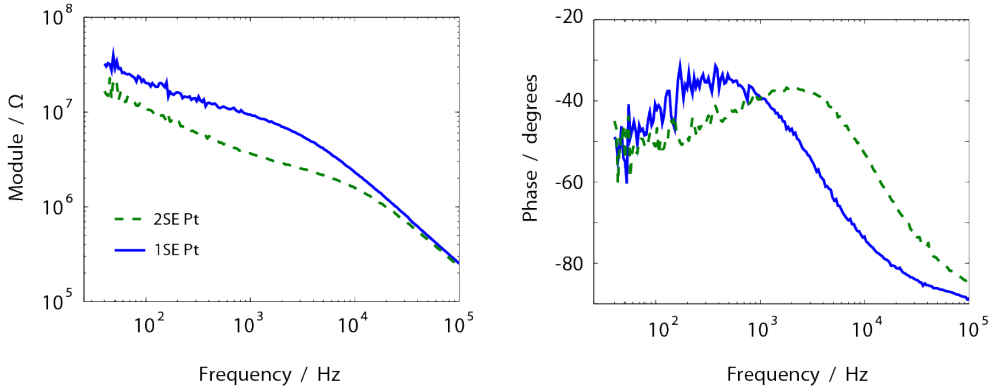

Figure 5.7: Characterisation of the impedance of one Ti/Pt electrode pair in contact with a solution of KCl at 0.01 mM. The measured module (a) and phase (b) are given for devices with electrodes on one or two sides of the channel.

The shape of the curves corresponds well to the theoretical simulations given in Section 3.7 and no major parasitics effects are observable. On the other hand, the impedance of the pumps is also influenced by the electrical path through the material the chips are made of. Because of the different materials used for the fabrication of the channels (NOA81 or MX5050), the non-resistive behaviour of the two kinds of prototypes is slightly different and may influence the velocity generation in the devices.

Platinum versus conducting oxide

Preliminary measurements of the sheet resistance of the deposited layers of Ti/Pt and ITO show that the latter is a worse conductor, exhibiting values around $14.68 \pm 0.3\ \Omega/sq$, while platinum layers have resistances ten times lower, around $1.71 \pm 0.03\ \Omega/sq$. It is therefore not surprising that the measured impedance is much larger for ITO electrodes than for metal structures, as Figure 5.8 shows. Whereas the impedance of the Pt electrodes corresponds to the models described in Section 3.7, ITO electrodes show strong capacitive behaviour, which will influence the effectiveness and magnitude of the velocity generation in the pumps.

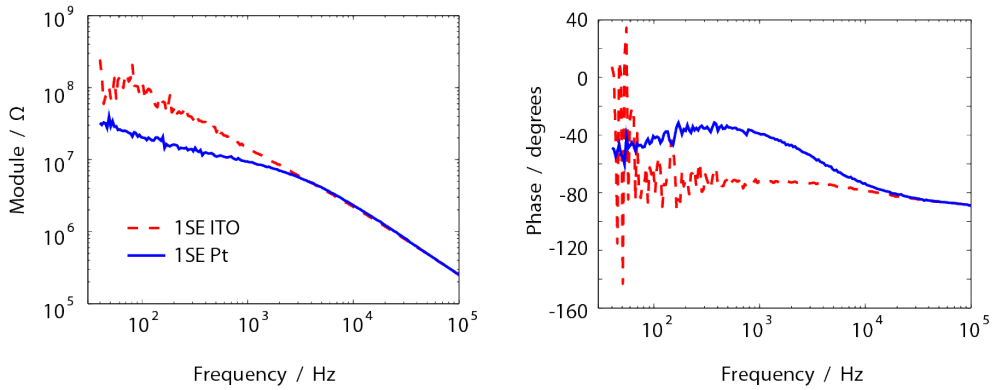

Figure 5.8: Characterisation of the impedance of one electrode pair in contact with a solution of KCl at 0.01 mM. The measured module (a) and phase (b) are given for devices with ITO or Ti/Pt electrodes on only one side of the channel.

Moreover, the impedance of ITO electrodes is much noisier than for Pt structures, showing that not only does the conductive oxide increase the resistance of the system, but it also contributes to the total impedance with parasitics that are not as relevant in the case of metal electrodes. Due to the relative importance of the capacitance of the ITO layer with respect to that of the EDL, it will be necessary to actuate the ITO pumps at higher frequencies. Operating the devices at higher frequencies will in turn increase the limit voltage at which electrolytic reactions will give observable effects.

5.4 Influence of the AC frequency

Characterisation of the complete ACEO prototype micropumps provides the experimental validation of the theoretical assumptions and gives important information about the performances that the devices can deliver. Indeed, the generation of velocity within an ACEO pump depends on both the magnitude and frequency of the applied AC potential, as well as on the electrolyte concentration of the test buffer.

This section discusses the influence of the applied frequency on the performances of the prototypes. In the first stage, the data will focus on the constant value of the forward generated velocity, measured distant from the electrodes in the middle of the channel (as explained in Chapter 4), after which the study will analyse the spectral content and the evolution in time of the generated motion. The effect of the voltage will be considered in Section 5.5 and the dependence on the buffer concentration will be addressed in Chapter 6.

5.4.1 Magnitude of the generated velocity

One-side-electrode prototypes with electrodes made of Pt and ITO have been tested to measure the evolution of the forward velocity that the pumps generate as a function of the

frequency of the applied AC potential. The devices having Pt electrodes were tested with a signal amplitude of 3 V_{pp}, while as much as 5 V_{pp} were necessary to obtain comparable flow velocities in the channels having ITO electrodes.

Figure 5.9 shows the data collected from the experiments and gives the comparison of the velocities generated by the Ti/Pt and ITO electrodes. As expected, the optimal frequencies for the two kinds of prototypes differ by more than one order of magnitude. Devices with Pt electrodes generate a maximum velocity of about 20.5 $\mu m/s$ for an applied signal of 3 V_{pp} and 150 Hz, whereas ITO electrodes produced a maximum velocity of about 6 $\mu m/s$ for an applied potential of 5 V_{pp} and 5 kHz.

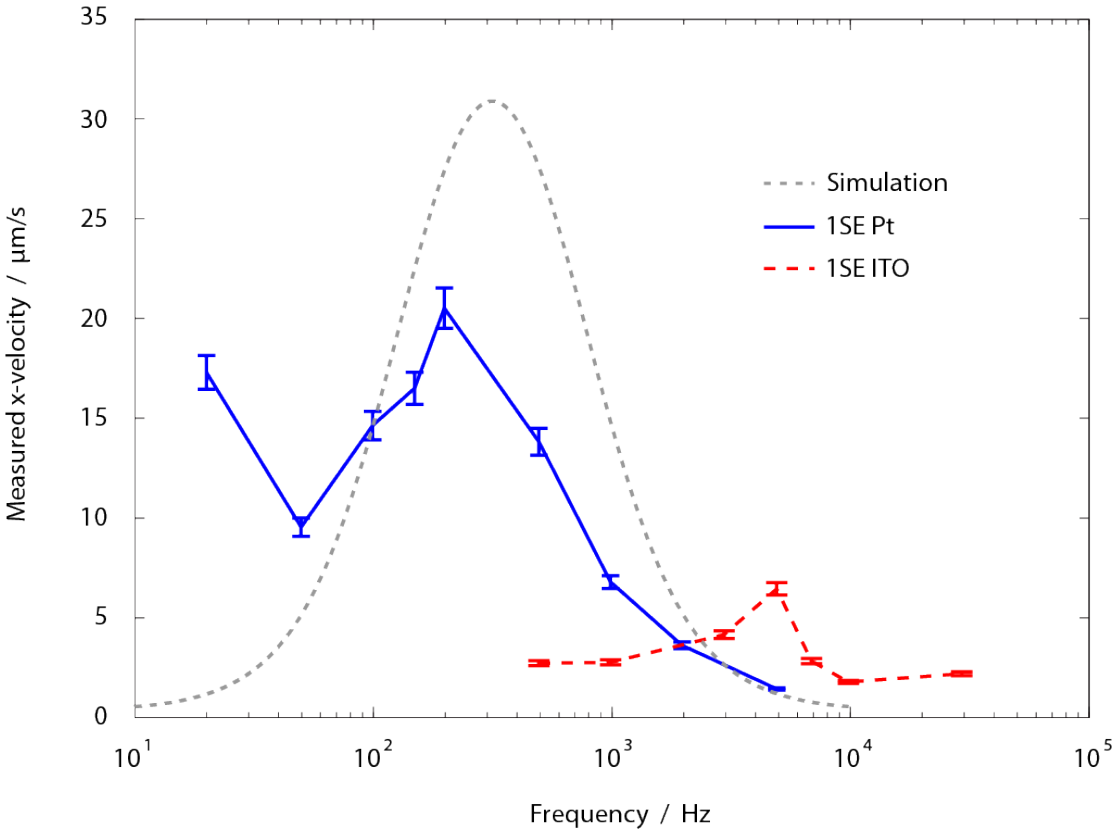

Figure 5.9: Dependence of the generated velocity on the frequency of the applied AC potential when the pumps are filled with a buffer of KCl at 0.01 mM. The graph shows the comparison between the performances of Ti/Pt pumps operated at 3 V_{pp} and ITO devices operated at 5 V_{pp}. The result of the simulations performed in Section 3.4 for a buffer concentration of 0.01 mM are given for comparison.

The curve obtained for devices with Ti/Pt electrodes is compatible with the velocity generation simulated in Section 3.4 for a buffer concentration of 0.01 mM, except for very low frequencies, where the velocity generation is influenced by the injection of charges in the liquid due to faradaic reactions [144], which is not accounted for in the model. On the other hand, the theoretical model fails to describe the velocity generation in devices based on ITO

electrodes, because it considers the electrodes to be ideally polarisable and only accounts for the behaviour of the EDL and the bulk solution.

Experiments confirm that the larger impedance of ITO electrodes has a detrimental effect on the performances of the ACEO micropumps. In addition to the shift in the optimal pumping frequency, the layer of ITO withstands a larger potential difference than platinum, thus reducing the electric field that falls on the electric double layer and the induced pumping force. This can explain why, when working with ITO, we need an almost double potential to generate only one third of the velocity.

5.4.2 Spectral content of the generated velocity

Most theoretical and experimental works focus on the constant time-average of the generated velocity and do not investigate how the instant velocity changes over time. Several works have studied the dynamic aspects of flows generated by the application of AC electric fields to DCEO designs [155, 156, 157, 158], but at our best knowledge the dynamic behaviour of ACEO pumps has not been the objet of research. Green *et al.* argued that a harmonic motion should be present in AC electro-osmotic flows, but that it was not observable in experiments [137, 138]. Nonetheless, the information about such behaviour can be very important when the pumps are used in experiments that rely on the transient behaviour of the fluid or of particles suspended therein. In order to investigate this aspect of AC electro-osmotic pumping, the motion of the microbeads in the pumps was recorded with a high speed camera.

Only devices with Pt electrodes were used, as they generate larger velocities which are easier to detect and allow for smaller measurement errors. Moreover, in order to respect the Nyquist criterion [159] and obtain reliable analysis of the phenomenon, the framerate at which the videos were acquired was adjusted in order to be always at least double the excitation frequency of the pumps. After applying the potential to the electrodes, data were recorded once the liquid motion had stabilised, which usually occurred within a few seconds from the beginning of the experiment.

After evaluating the velocity $v(t)$ for each frame of the recorded videos, spectra were obtained by computing the fast Fourier transform (FFT) $\mathbf{F}[v(t)]$ with Matlab [140]. Figure 5.10 gives the measured spectra for an applied potential of 3 V_{pp} and frequencies ranging from 20 Hz to 5 kHz. For excitation frequencies below the optimal value, clear peaks are observable at zero frequency, corresponding to the constant average velocity of the liquid, and at the excitation frequency, corresponding to small local oscillations of the fluid following the oscillations of the applied potential. For frequencies larger than the optimal value both peaks become less and less important, indicating that the pump generates increasingly lower velocities and that the beads used to visualise the motion of the fluid cannot follow very fast oscillations.

Not only may such oscillations influence the trajectory of particles suspended in the buffer during the experiments. Their existence also affects the power-conversion efficiency of the

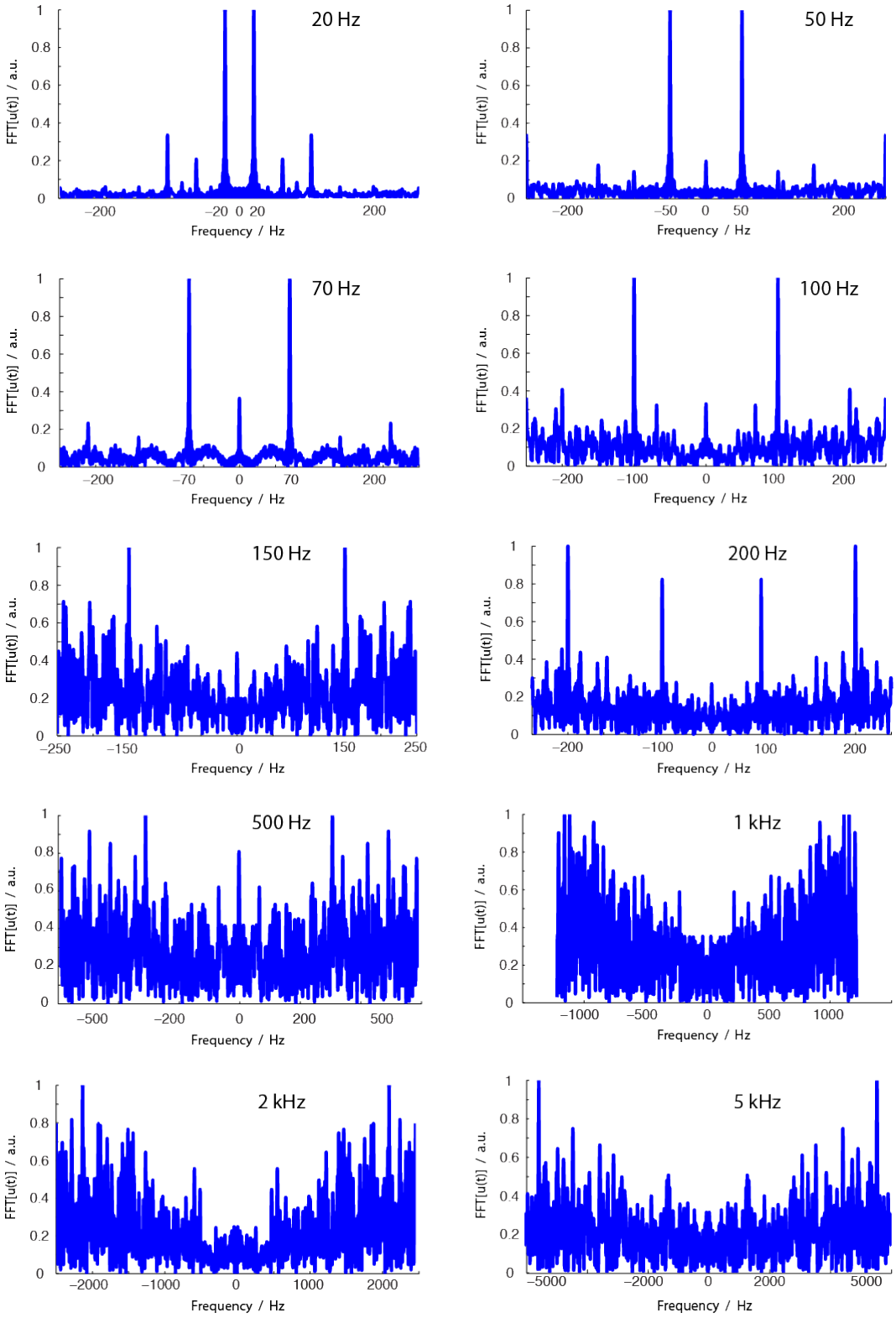

Figure 5.10: Spectra of the velocity generated by 1SE pumps working with a solution of KCl at 0.01 mM, operated at 3 V_{pp} and at frequencies between 20 Hz and 5 kHz.

pump, since the energy required to maintain the oscillations of the liquid does not contribute to the generation of the net forward motion and is therefore lost.

5.5 Dependence on the AC potential

The second important parameter that determines the properties of the generated flow is the magnitude of the applied voltage: according to the theory of AC electro-osmosis, as detailed in Chapter 3, the velocity should increase as the square of the applied potential. Experimental observations carried out on our prototypes confirm this behaviour for voltages lower than 5 V_{pp}, value at which we observed the formation of gas bubbles and the failure of the devices to generate constant velocities. Figure 5.11 gives the measured velocities at the optimal pumping frequency in the one-side- and two-side-electrode micropumps with Pt and ITO electrodes, along with a quadratic fit confirming that the velocity is proportional to the square of the applied voltage.

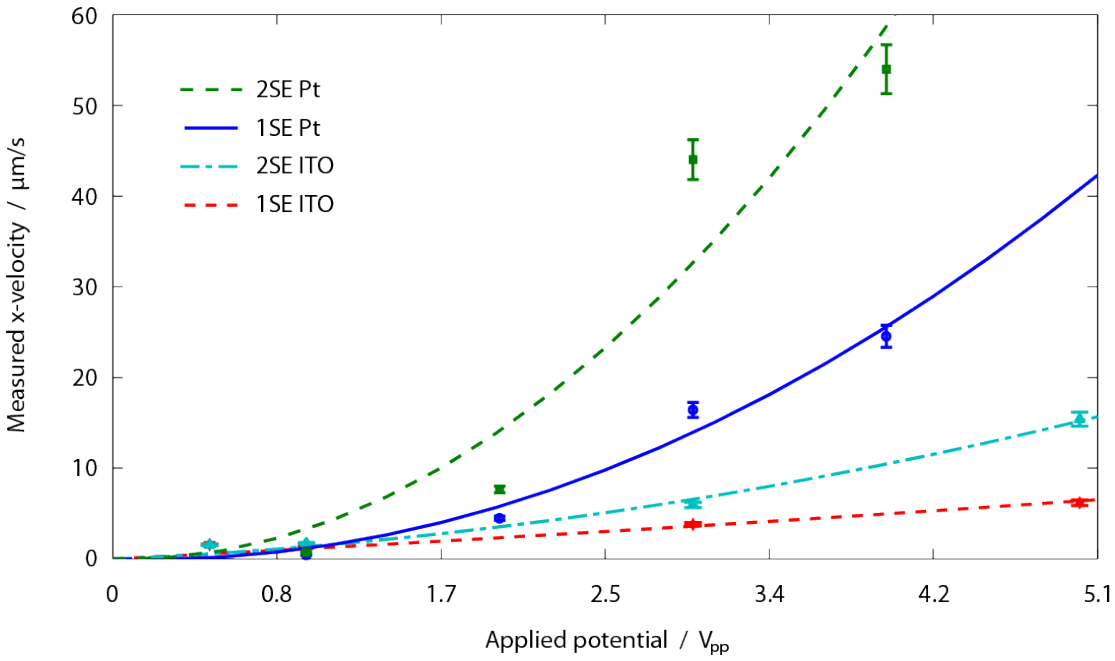

Figure 5.11: Dependence of the generated velocity on the magnitude of the applied AC potential, when the pumps are filled with a buffer of KCl at 0.01 mM. The graph shows the comparison between the performances of the pumps operated at their optimal frequencies: 150 Hz for Ti/Pt devices and 5 kHz for the ones with ITO. In order to show the dependence of the generated velocity on the square of the applied potential, the experimental points were fitted to quadratic functions (broken lines).

Similar to the results in the previous section, we find that Pt electrodes are much more effective at generating liquid velocity than structures made of ITO. As Table 5.1 summarises, 2SE Pt

pumps were able to generate as much as 53.9 $\mu m/s$ of liquid velocity at 4 V_{pp}, corresponding to a flow-rate of about 21.4 nL/min, whereas their ITO counterparts only generated 15.4 $\mu m/s$ at 5 V_{pp}, which is equivalent to a flow-rate of about 6 nL/min.

Table 5.1: Comparison of the best measured velocities generated by Ti/Pt and ITO 2SE pumps. The equivalent flow-rate for a cross-section of 100x100 μm^2 is also given.

	$c_0\ (mM)$	$V_0\ (V_{pp})$	$f_{opt}\ (Hz)$	$v_{2SE}\ (\mu m/s)$	$Q_{eq}\ (nL/min)$
Pt	0.01	4	150	53.9	21.4
ITO	0.01	5	$5 \cdot 10^3$	15.4	6.1

Generally speaking, the characterisation of the behaviour of the ACEO micropumps as a function of the applied voltage and frequencies shows that there is a good potential for the implementation of such devices in closed-loop configurations, where the generated flow-rate is regulated in real time, through the addition of a flow meter in the system. The capability to control the magnitude and frequency of the actuation potential with high precision, and the possibility of obtaining large changes in the generated velocity through small adjustments of the magnitude and frequency of the applied signal, show all the potential of ACEO pumps to guarantee a very fine and precise control on the generated liquid flow.

5.6 Improvement of performances

The main objective of the study presented in this chapter is to investigate the effect of increasing the extent of the electrodes around the channel on the average velocity generation. The comparison of performances of the devices that were characterised, given in Table 5.2, shows that two-side-electrode micropumps provide a huge amplification of the generated liquid motion.

Table 5.2: Comparison of the measured velocity increase generated by Ti/Pt and ITO 2SE pumps, with respect to the performances of 1SE devices.

	$c_0\ (mM)$	$V_0\ (V_{pp})$	$f_{opt}\ (Hz)$	$v_{1SE}\ (\mu m/s)$	$v_{2SE}\ (\mu m/s)$	$(v_{2SE} - v_{1SE})/v_{1SE}$
Pt	0.01	3	150	20.5	44.0	115%
ITO	0.01	5	$5 \cdot 10^3$	6.2	15.4	148%

Doubling the extent of platinum electrodes multiplied the generated velocity by a factor of about 2.1, whereas the two-side-electrode pumps with ITO electrodes generated a velocity about 2.5 times the value obtained with the one-side-electrode prototypes. The measurements prove that Pt is a better choice for the electrode material and that the velocity generation is directly related to the total surface of electrodes exposed to the buffer, confirming the theoretical assumptions made in Chapter 3.

5.7 Conclusion: towards all-around-electrode pumps

Simple prototypes able to generate liquid motion by AC electro-omosis were fabricated on Pyrex substrates with Pt and ITO electrodes. We showed that micropumps with the electrodes patterned on one or two opposite sides of the channel can easily be obtained and we characterised the fabricated devices with a dilute solution of KCl at 0.01 mM.

Comparing micropumps based on Pt with devices based on ITO demonstrated that metal electrodes are much more effective and can generate much larger liquid velocities at lower applied potentials. Comparing metal and conductive oxide also allowed the understanding of the crucial importance of realising electrodes with low impedance: the smaller the impedance of the electrode material, the larger will be the potential drop on the electric double layer and the channel. In turn, a larger potential drop will guarantee larger ACEO force and velocity generation on the surface of the electrodes. For these reasons, the family of prototypes that will be presented in the next chapter will be fabricated with only Pt electrodes.

Another important aspect of velocity generation through AC electro-osmosis, which has been highlighted in this chapter, concerns the oscillatory motion that is transmitted to the fluid by the oscillation of the applied electric fields. Such behaviour may affect experiments carried out on particles suspended in the liquid (e.g. separation techniques) and reduces the efficiency of the pumps by converting part of the consumed electric power into oscillatory motion that does not contribute to the net forward flow. However, the proper functioning of the pump as flow generator is not directly affected.

Experimental observations confirmed that increasing the extent of the electrodes around the channel ameliorates the flow-rate generated in ACEO pumps. Multiplying the electrode length by a factor 2 doubled the average velocity generation of the devices. This corroborates the thesis introduced in Section 3.5 that the average generated velocity is proportional to the extent of the electrodes around the channel, and motivates the fabrication of prototypes where the length of the electrodes is extended to the whole perimeter of the pumping channel.

6 All-Around-Electrode Micropumps

The reason why DC electro-osmosis is so effective at pumping liquids and standing large backpressures lies in the distribution of the electric double layer and the generation of the pumping force all around the channel. Patterning electrodes on all the walls of AC electro-osmotic micropumps is challenging, but it allows a similar distribution of forces and emulates the velocity generation of DCEO micropumps. The resulting flow profile has a much greater average velocity and the pump is able to stand larger backpressures.

6.1 Introduction

Scientific literature includes many examples of strategies to improve the performances of AC electro-osmotic micropumps. Such approaches are effective, but they require complex fabrication processes to produce 3D electrode structures, as illustrated in Chapter 2, and sometimes reduce the cross-section available for the transit of the liquid by realising tall structures in the middle of the channel [114]. A simpler approach is to increase the extent of the electrodes around the channel. We have shown in the previous chapters that this approach is theoretically correct and can be validated experimentally. Here we show that the reasoning can be pushed further and we present the fabrication of a device with electrodes patterned all around the channels.

The study will be limited to platinum, since it has shown better performances than ITO, as discussed in Chapter 5. After describing the fabrication process to obtain the all-around electrodes (AAE), this chapter will present the characterisation of the electrical impedance and fluidic performances of the prototypes. The maximum generated velocity will be compared to the values measured in the 1SE and 2SE devices to show that the experimental results correspond well to the theoretical predictions. Moreover, the behaviour of the AAE micropumps will be assessed as a function of the concentration of the test solution, and the power-conversion efficiency will also be evaluated.

6.2 Fabricating electrodes on deep channels

Realising ACEO micropumps with electrodes all around the channel requires only one additional processing step with respect to the fabrication of one-side planar devices. However, the order of the fabrication steps is changed and some actions are substituted by others. The channels will be fabricated prior to the deposition of electrodes, which will be patterned on the 3D topography of the structured wafers. We kept the same electrode design and chose Pyrex glass as the channel material. Since standard lithography cannot provide uniform exposure of photoresist over a high depth, special optics were required for the exposure. Moreover, spin-coating of the structured wafers was replaced by spray-coating for similar reasons.

6.2.1 Etching the channels

We used Borofloat 33 Pyrex wafers to fabricate half of the pump structure, then aligned and bonded two of them in order to obtain the all-around-electrode devices. First, a layer of 400 nm of poly-silicon was deposited on both sides of a new batch of pyrex wafers by low-pressure chemical vapour deposition (LPCVD). Such a layer is intended to be used as a mask for the etch of the channels with hydrofluoric acid [160]. The lithography for the channels was then performed with standard AZ1518 photoresist on the poly-Si surface, followed by reactive ion etch (RIE) of the poly-Si to open the channel features (see steps 1-2 in Figure 6.2).

Using only the poly-Si mask, 50-μm-deep channels were etched in 50% HF, after which poly-Si was removed in a bath of potassium hydroxide (KOH). Microscope pictures of the obtained channels are given in Figure 6.1 alongside the open poly-Si mask prior to the HF etch. For reasons connected to the adhesion of the poly-Si mask layer, the HF etch produced channels larger than expected (300 μm instead of 200 μm) and with walls at about 45° (see steps 3-4 in Figure 6.2). Although this was surprising, it eased the realisation of the electrode patterns.

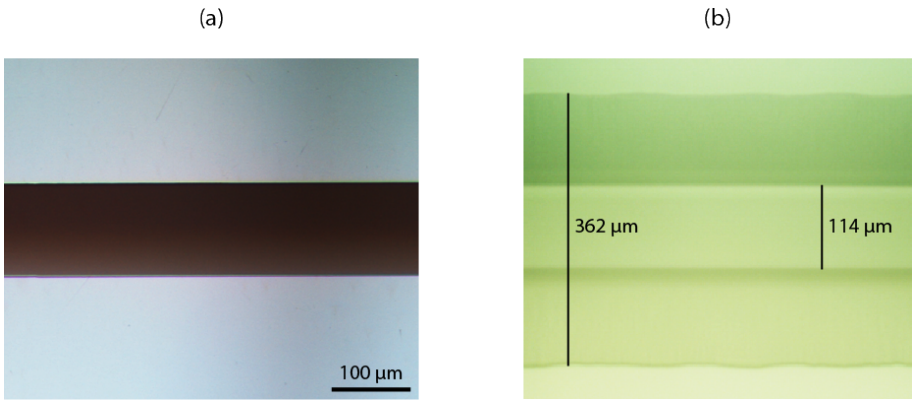

Figure 6.1: Poly-Si mask used for the etch with 50% HF (a) and resulting channel structure (b). Due to weak adhesion of the poly-Si mask, the etched channels are larger than designed.

6.2.2 Electrodes on 3D topography

Metal was patterned following the same design discussed in Chapter 5. Since the process to realise the final devices by joining two processed wafers includes a treatment at high temperature, tantalum was used as an adhesion layer instead of titanium, which tends to diffuse into Pt at large temperatures. According to previous studies [161], Ta should be able to stand high temperatures without diffusing into platinum; this is important because the metal in contact with the test solution needs to be Pt only.

Pyrex substrates with the structured channels were sent to Süss MicroTec (Munich, Germany) to be spray-coated and exposed. The negative resist AZ nLof 2070 was used to achieve conformal coating of the structures and was subsequently exposed with the mask aligner MA6 mounted with LGO optics. Such exposure tools allow the generation of straight and parallel illumination over several tens of micrometers, thus enabling an easy patterning of non-flat topographies. The precision of the lithography was very good and patterns were defined on the top and bottom surfaces of the channels with very little deviation.

Upon reception of the processed wafers and before performing the lift-off, the wafers were

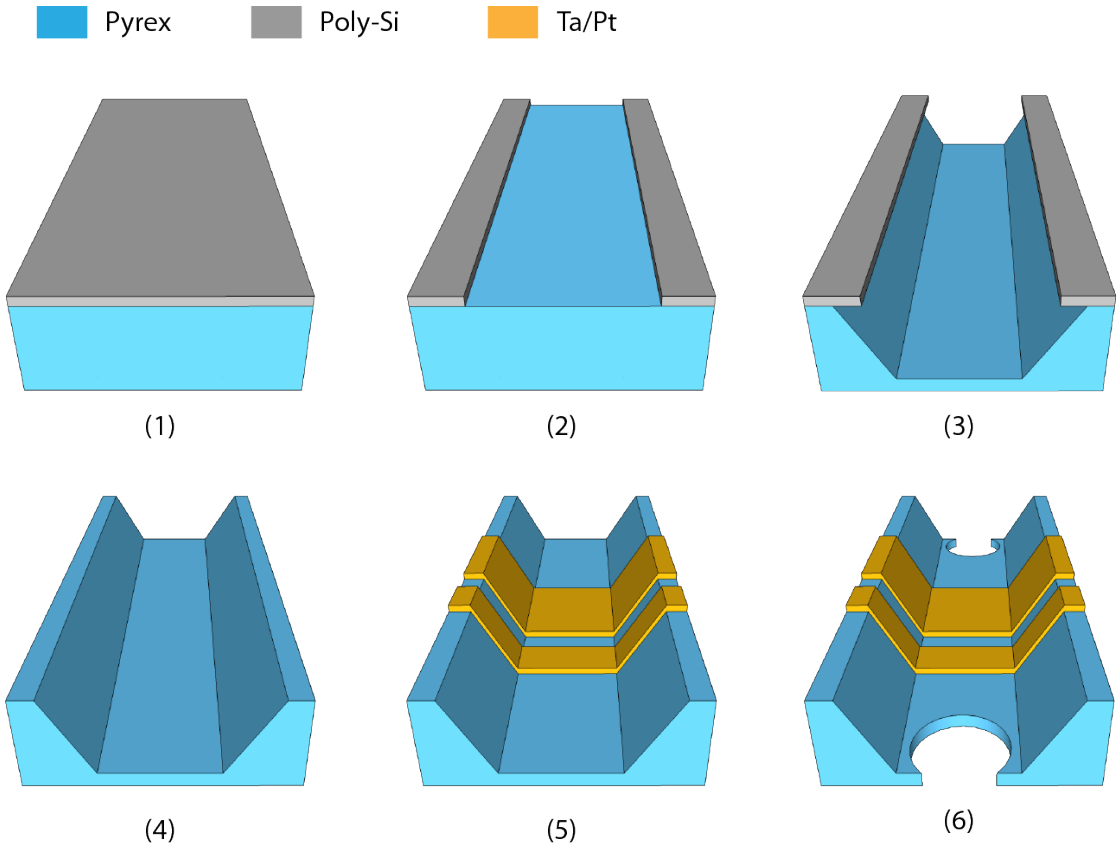

Figure 6.2: Fabrication process to pattern metal electrodes on pre-structured Pyrex wafers. Step (6) is performed on one half of the batch only.

dipped in a bath of buffered hydrofluoric acid (BHF) in order to etch about 120 nm of glass and leave small grooves that the metal would fill. Such a method ensures an ideal profile of the photoresist for the lift-off process and guarantees that the metal deposition does not affect the planarity of the wafers, which is necessary to successfully bond the substrates.

For the metal deposition, 20 nm of Ta were evaporated as an adhesion layer, followed by 100 nm of Pt. The lift-off was performed in acetone and gave excellent results. Figure 6.3 shows pictures of the patterned electrodes acquired with an optical microscope and the XL30 ESEM-FEG environmental scanning electron microscope from Philips (Amsterdam, The Netherlands). The top and bottom surfaces, as well as the sides of the channel, are uniformly covered by the metal layers. Electrodes are clearly defined and correspond well to the features designed on the masks.

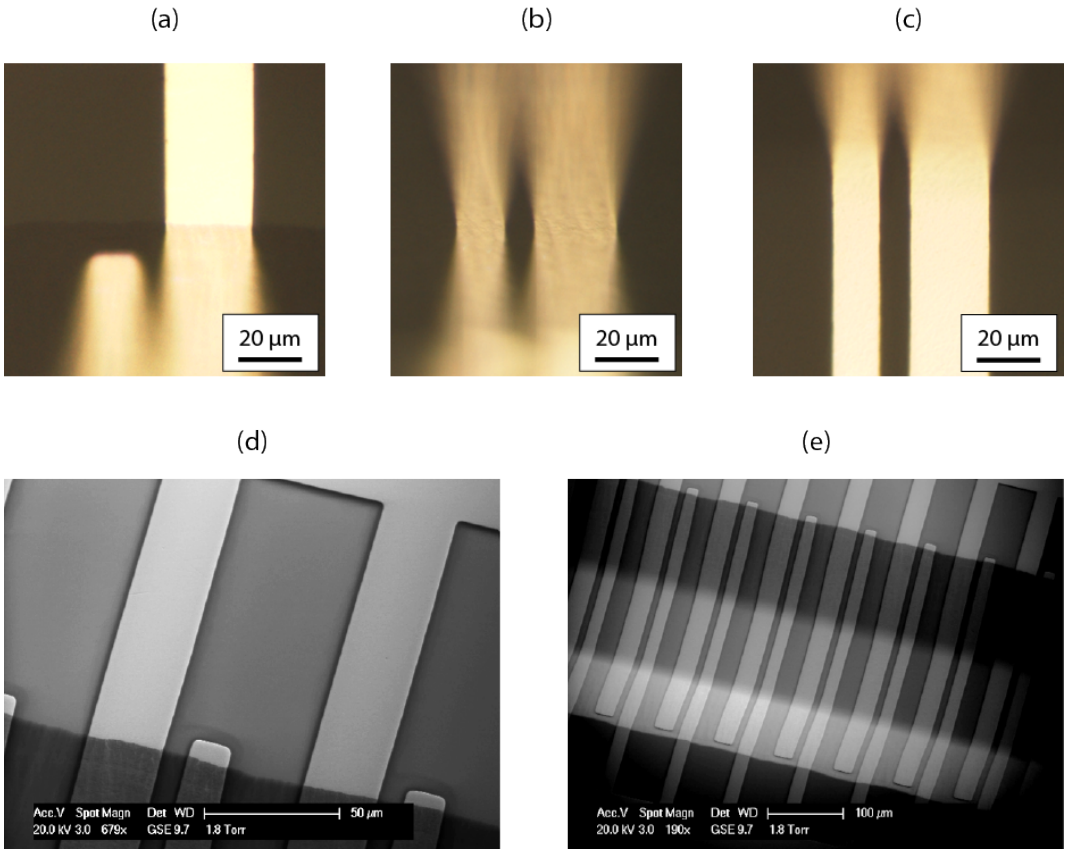

Figure 6.3: Pictures of the patterned electrodes on the top (a), side (b) and bottom (c) surfaces of the 50-μm-deep channels taken with an optical microscope at 20x magnification, alongside images of the top surface (d) and the whole channel (e) obtained with the ESEM. In (d) it is possible to observe the small grooves etched with BHF and used to deposit the metal.

6.2.3 All-around-electrode prototypes

The last steps to obtain the complete prototypes include opening the access holes to the channels, bonding the wafers together and dicing the single chips. As for the fabrication of the 2SE micropumps described in Chapter 5, access holes were realised by sandblasting half of the batch of wafers. After this, the substrates were cleaned using a procedure that includes oxygen-plasma, acetone, isopropanol, DI water and pure nitric acid, in order to prepare them for the bonding process. A summary of the process until this point is given in Figure 6.2.

Alignment of the wafers was performed by hand, exploiting metal features that were patterned for this purpose, and checked with an optical microscope before bonding. As illustrated in Figure 6.4, the electrical connection of the corresponding electrodes on the top and bottom wafer is ensured by contacting the large metal lines on the side. The channels were sealed by applying a small pressure and heating up to 655 $^{\circ}C$ for several hours. This last part of the process was performed outside the cleanroom, in a dedicated oven. Figure 6.5 shows a picture of the bonded wafer. The bonding process had a relatively low yield, which can be explained by the fact that the deposition of LPCVD poly-Si alters the overall planarity of the wafers, and that the Ta/Pt electrodes developed a significant stress during the high-temperature treatment, as it can clearly be seen in Figure 6.6. Consequently, the interface between the two bonding wafers was not as planar as expected, which influenced the yield of the bonding process. Moreover, such stressed electrodes tended to loose their adhesion on Pyrex during the fluidic tests, causing the failure of the devices.

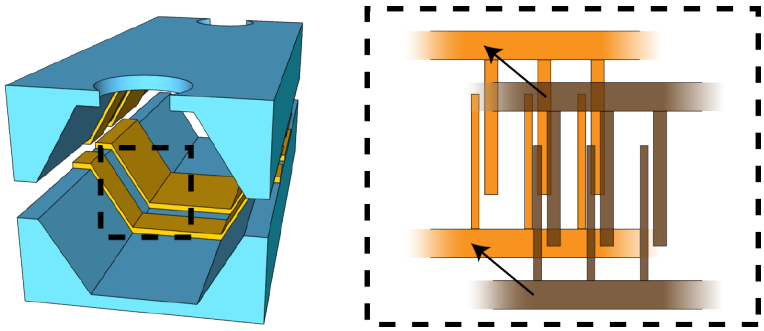

Figure 6.4: Schematic view of the alignment procedure to obtain the all-around electrodes. The larger metal lines on the sides of the channel are in contact after the bonding process and ensure the electrical connection of the corresponding electrodes (large and small).

Finally, single chips were diced and provided with electrical and fluidic connections, as explained in Chapter 5 for the two-side-electrode pumps. The final devices are shown in Figure 6.7. In order to tackle the degradation of the Ta adhesion layer, we defined an alternative sealing process that could be carried out at ambient temperature. In this case, wafers were diced before bonding, and the top and bottom chips were aligned by hand on a microscope slide. The devices were then sealed with 2-tone epoxy from Devcon (Danvers, MA, USA), which we poured around the chip to guarantee watertightness, whilst applying a light pressure on the stack in order to prevent the glue from diffusing between the two chips.

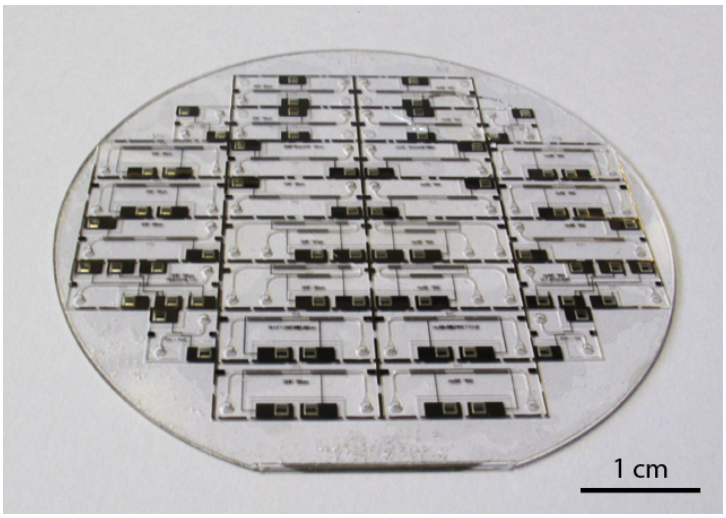

Figure 6.5: Wafer with the AAE pumps after the bonding procedure.

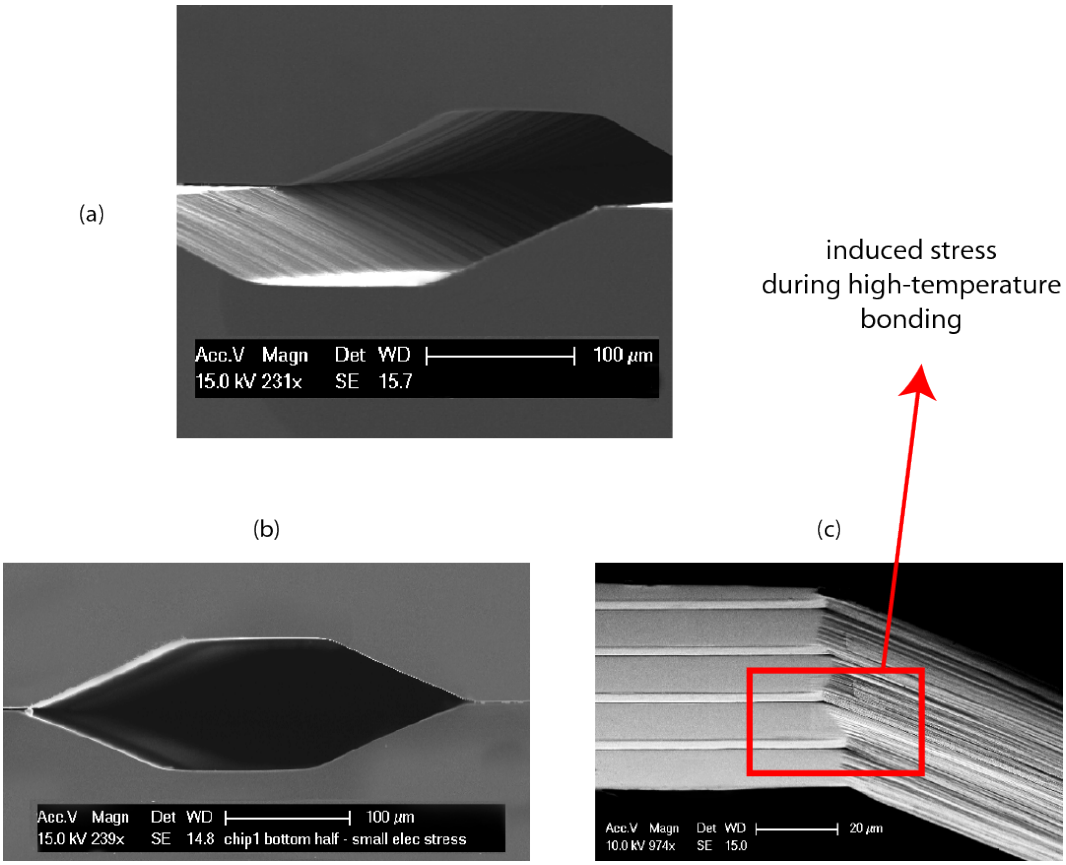

Figure 6.6: Images of the channels after bonding acquired with an ESEM. The electrodes clearly surround the whole channel (a), which has a "double D"-shaped cross-section (b). The stress induced in the electrodes by the bonding procedure can also be seen (c).

6.3 Characterisation of the improved micropumps

Experimental characterisation of the microfabricated all-around-electrode ACEO pumps proves that extending the surface of the electrode on all the sides of the channel allows for a dramatic increase in the generated liquid velocity. After analysing the impedance of the devices, this section will discuss the dependence of the generated flow on the properties of the applied signal as well as on the concentration of the test buffer.

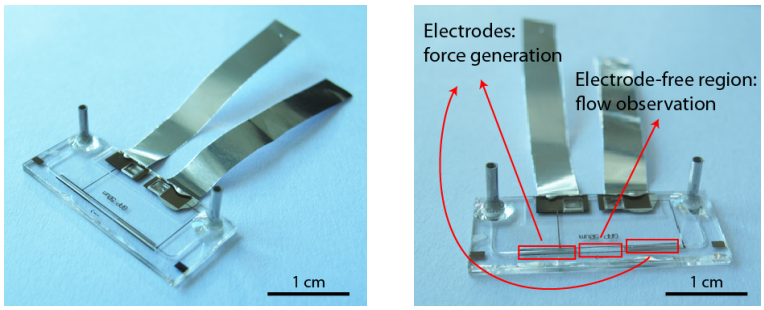

Figure 6.7: Fabricated all-around-electrode ACEO micropumps with electrical and fluidic connections.

6.3.1 Electrical impedance

As for the pumps presented in Chapter 5, it is important to characterise the impedance of the fabricated all-around-electrode micropumps. The reasons are the same: on one hand, information about impedance allows a preliminary check of the potential parasitics introduced by the fabrication process, while on the other it enables the evaluation of the power consumption and frequency dependence of the devices. Figure 6.8 shows the graphs of the measured module and phase of the impedance for the AAE prototypes at a KCl buffer concentration of 0.01 mM. The comparison with the curves of 1SE and 2SE devices is also provided.

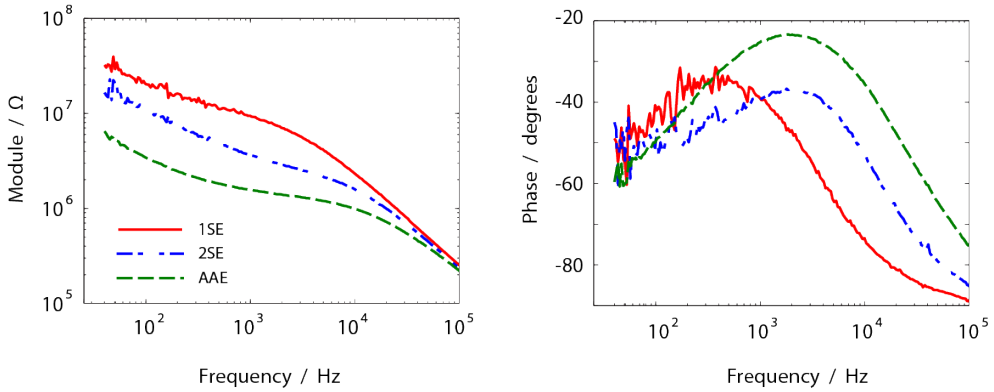

Figure 6.8: Characterisation of the impedance of one electrode pair in contact with a solution of KCl at 0.01 mM. The measured module (a) and phase (b) are given for 1SE, 2SE and AAE devices.

As we observed in Chapter 5 for the 2SE prototypes, the increased surface of electrodes in contact with the test solution leads to a lower impedance. This also means that the AAE prototypes will consume more power than simpler devices loaded with the same buffers. Again, the shape of the measured impedance is compatible with the theoretical simulations shown in Chapter 3, and shows that no major parasitic effect is present. Moreover, except for the 1SE devices, where there may be an influence of the UV-curable glue on the electric behaviour, the location of the first pole of the impedance is comparable for 2SE and AAE prototypes, showing that the frequency dependence of the prototypes is mainly determined by the design of the basic pair of asymmetric electrodes, while their extent around the channel influences the magnitude of the impedance.

6.3.2 Influence of the AC frequency

All-around-electrode micropumps were characterised following the same approach described in Chapter 5 to measure the dependence of the velocity generation on the frequency of the applied signal. The measurements were carried out at a potential of 3 V_{pp} and with a KCl solution at 0.01 mM, and the velocity observed in a portion of the channel distant from the electrodes, as explained in Chapter 4.

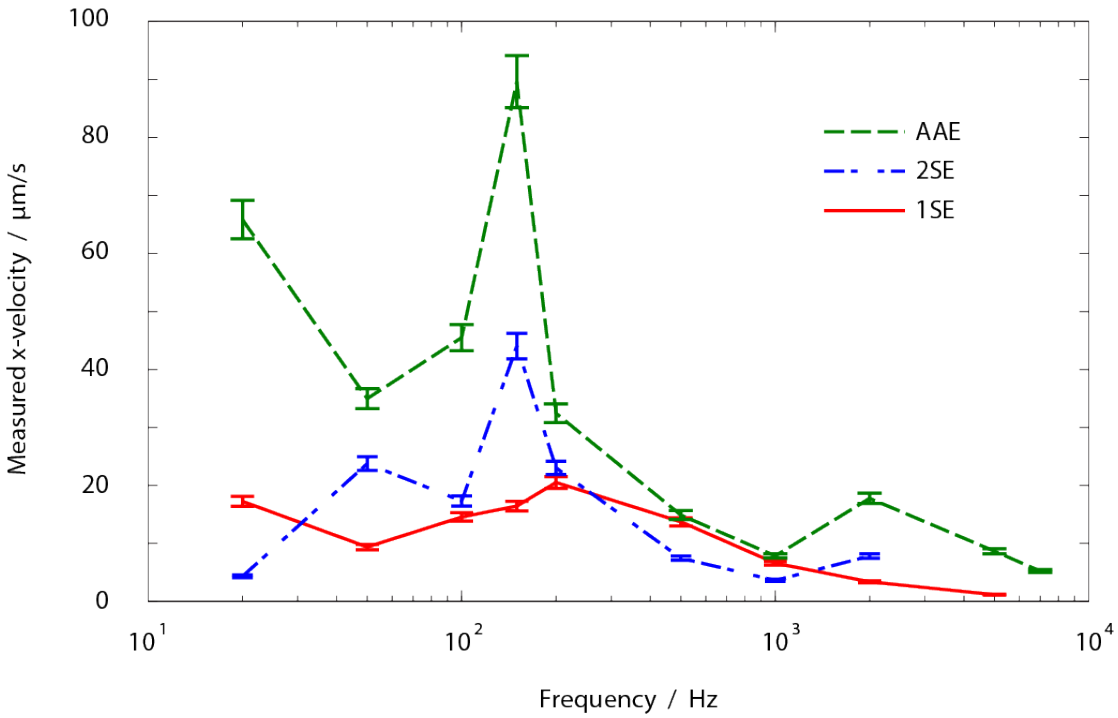

Figure 6.9: Dependence of the generated velocity on the frequency of the applied AC potential, when the pumps are filled with a buffer of KCl at 0.01 mM. The graph shows the comparison between the performances of 1SE, 2SE and AAE pumps operated at 3 V_{pp}.

Figure 6.9 shows the comparison of the measured velocity in 1SE, 2SE and AAE prototypes, as a function of the applied frequency. The optimal pumping frequency of AAE prototypes is about 150 Hz, the same as for the 2SE pumps, while the maximum velocity in 1SE prototypes was measured at a slightly higher frequency, around 200 Hz. This small deviation is probably the result of the difference in the impedances of the devices. The maximum measured liquid velocity that the AAE micropumps were able to generate was about 89.6 $\mu m/s$, which corresponds to a flow-rate in the channel of about 71 nL/min.

6.3.3 Dependence on the AC potential

Velocity generation increases as the square of the applied voltage, as illustrated by the curves in Figure 6.10, where the performances of the one-side and two-side devices are given for comparison. The graph shows the experimental points along with fitting curves, confirming the quadratic dependence of the velocity on the applied voltage. The experiments were carried out with AAE Pt pumps, operated at the optimal frequency with a KCl buffer at 0.01 mM; at an applied potential of 4 V_{pp} at the optimal frequency, the all-around-electrode devices were able to generate velocities of up to 105 $\mu m/s$, equivalent to flow-rates of about 84 nL/min.

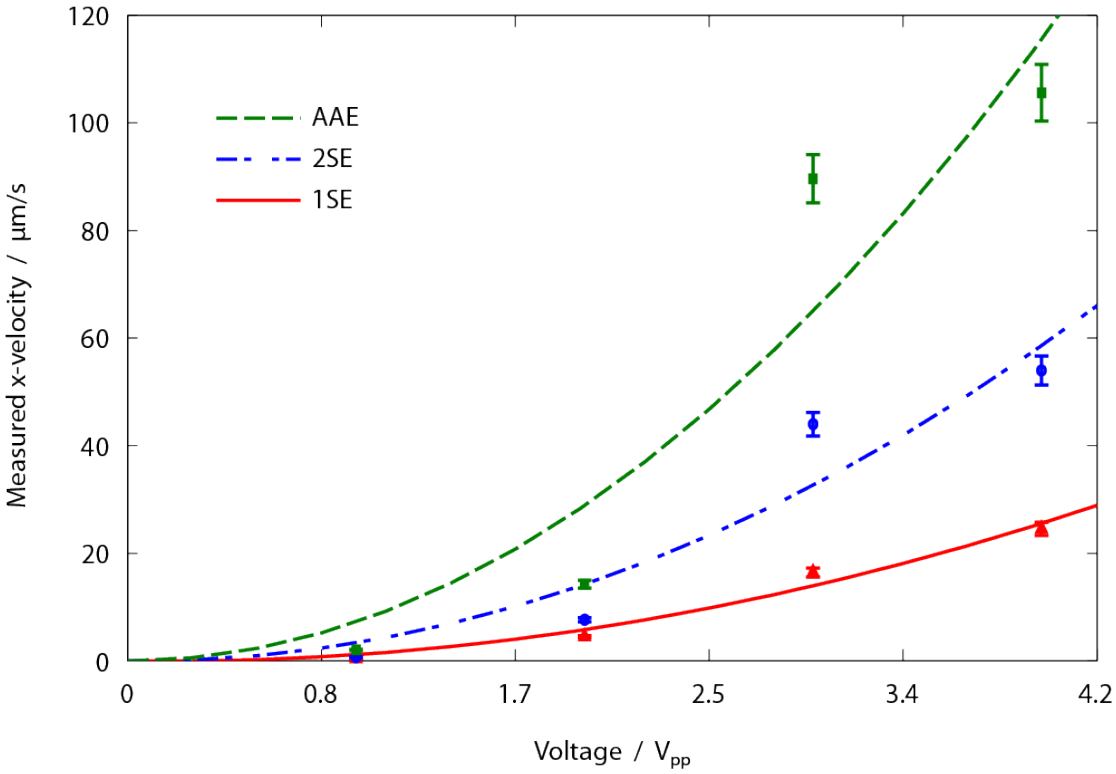

Figure 6.10: Dependence of the generated velocity on the magnitude of the applied AC potential, when the pumps are filled with a buffer of KCl at 0.01 mM. The graph shows the comparison between the performances of 1SE, 2SE and AAE pumps operated at the optimal frequency.

6.3.4 Influence of the buffer

Because the behaviour of ACEO micropumps depends strongly on the concentration of the test buffer and the generated velocity decreases rapidly with increasing values of electrolyte concentration, only all-around-electrode prototypes were tested to observe this effect. In fact, one-side and two-side pumps could generate little or zero velocity at high concentrations of the buffer, whereas the AAE devices maintained detectable liquid motion even at the highest concentrations that were tested. Moreover, we used lower potentials for these tests, since electrolysis and gas generation occur more easily in solutions with higher electrical conductivities.

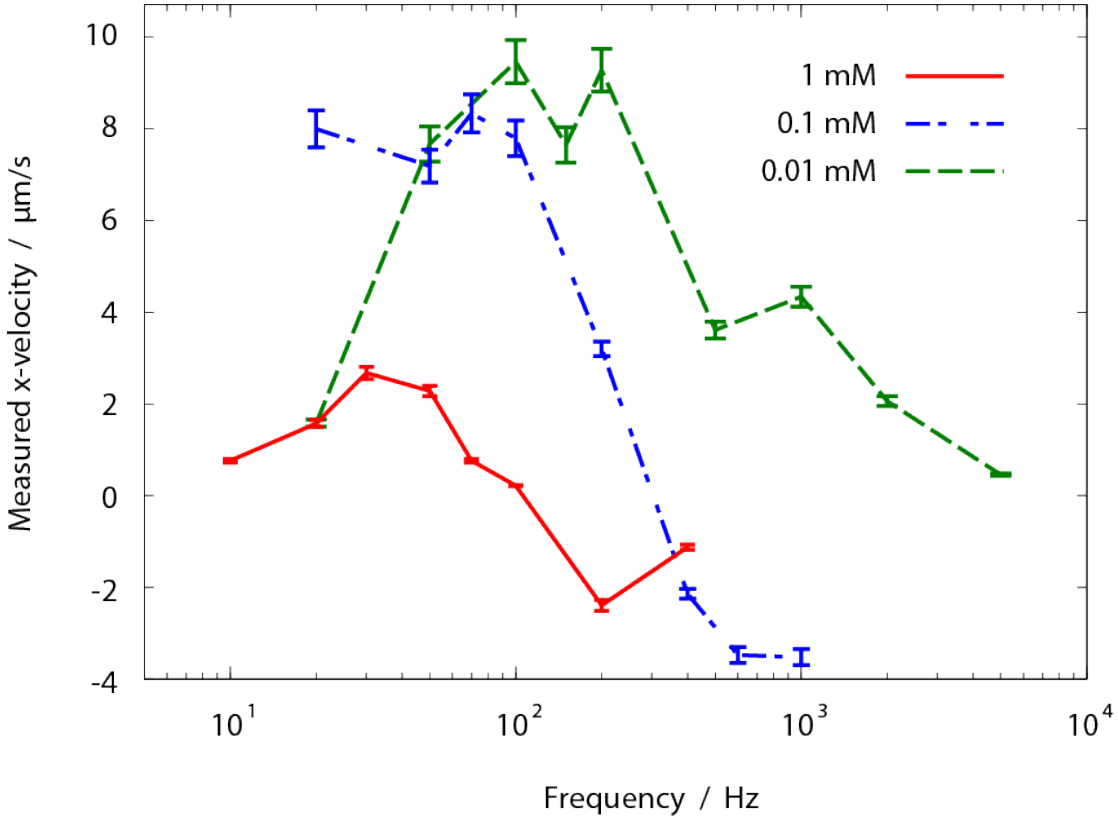

Figure 6.11: Dependence of the generated velocity on the concentration of the KCl solution. The graph shows the comparison between the performances of the AAE pumps operated at 2 V_{pp}. The optimal frequency shifts towards lower values when the buffer concentration is increased, in agreement with theory.

Figure 6.11 shows the frequency dependence of the measured velocities in the AAE micropumps with a potential of 2 V_{pp} and buffer concentrations between 0.01 mM and 1 mM. The optimal frequency shifts towards lower values as the concentration of the test solution is increased, in agreement with the simulations presented in Section 3.4. However, the formula used to compute the magnitude of the velocity does not account for the influence of the buffer concentration and the simulations fail to predict the linear decrease of the generated velocity.

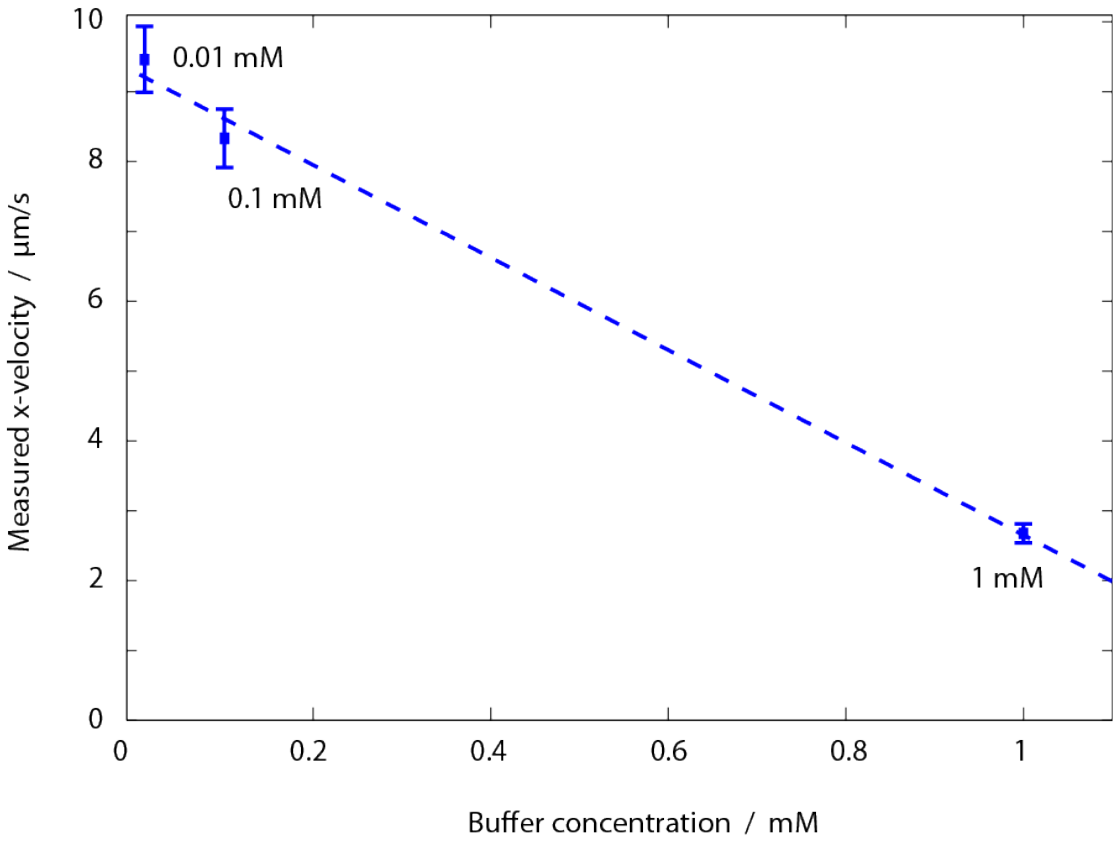

Figure 6.12: Maximum measured velocities in the AAE pumps for the different KCl concentrations and an applied potential of 2 V_{pp} at the optimal frequency (150Hz). The broken line shows the linear fit of the experimental data.

Figure 6.12 reports the maximum values of velocity measured at an applied potential of 2 V_{pp}. Equivalent flow-rates of about 20 nL/min were observed with the buffer at 0.01 mM, while the value reduces to only 4 nL/min for a solution at 1 mM and almost no motion could be detected at higher buffer concentrations, which are not reported in the graphs. Such a strong reduction of the flow generation capability at large solution concentrations is critical to the implementation of ACEO pumping with biomedical liquids, which usually have salt and electrolyte concentrations in the order of 10 mM or even larger. Nevertheless, there remains room for the improvement of the design of the electrode patterns and of the structure of the channel, which should allow for larger generated velocities and flow-rates.

6.4 Evaluation of performances

All-around-electrode micropumps were able to generate velocities much larger than those measured for the one-side and two-side devices. However, these absolute values are smaller than for many micropumps reported in the scientific literature. This difference can be explained by looking at the width-ratio of the electrodes for our pumps and for the devices from

other research: the considerations made in Chapter 3 led us to the design of structures where the sizes of the large and the small electrode differ by very little. On the other hand, most reported devices exploit electrode pairs having a width-ratio much larger, which allows for a greater velocity generation. Nevertheless, the focus of our work is on the improvement of the performances for a given electrode design and not on the absolute value of the generated velocity or flow-rate.

Increased velocity generation

Patterning electrodes on all the walls of the channel allows the increase of the generated velocity by a factor that varies linearly with the ratio $\mathscr{P}_{el}/\mathscr{P}_{tot}$. Figure 6.13 shows the plot of the velocity generated by the pumps when a potential of 3 V_{pp} was applied at the optimal frequency, versus the ratio of the perimeters of the electrodes and of the channel. The velocity in the AAE prototypes corresponds to about 4 times the value generated in the 1SE devices and about 2 times that of 2SE pumps, which is in very good agreement with the theory and simulations presented in Chapter 3.

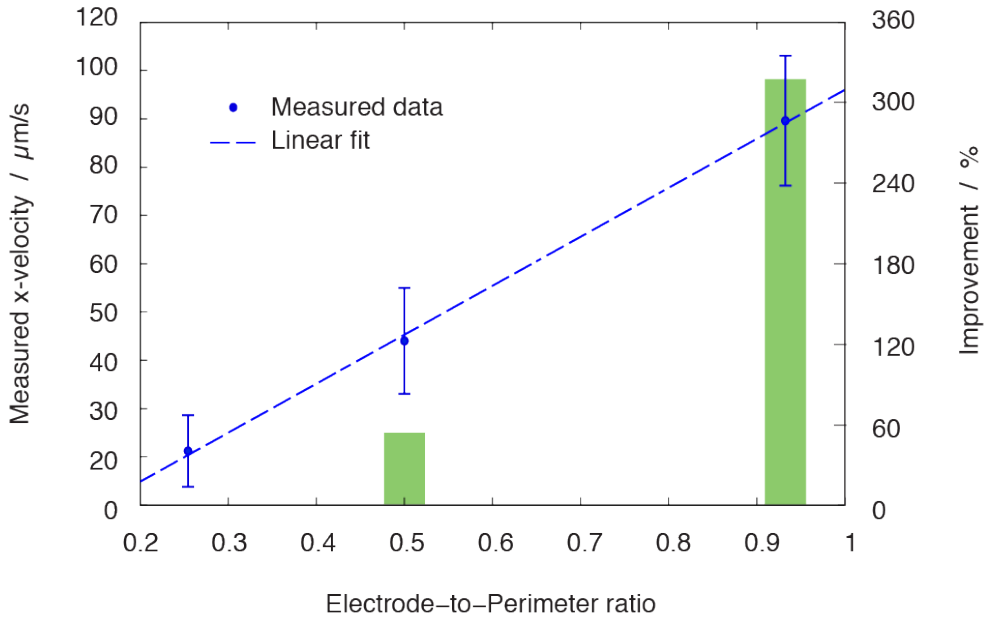

Figure 6.13: Measured velocities at the optimal frequency for an applied potential of 3 V_{pp} and a KCl concentration of 0.01 mM. The increase of the generated velocity with respect to the 1SE prototypes is also shown.

The relative increase of the generated velocity in AAE micropumps with respect to the 1SE devices was about 320% for an applied potential of 3 V_{pp} and grew to 360% when the applied voltage was of 4 V_{pp}. Such performances are also comparable with the results obtained by Rouabah *et al.* with 3D carbon electrodes [114], which gave a velocity increase of about 440% for an applied potential of 19 V_{pp}.

Power consumption and efficiency

It is also interesting to measure the power consumption of the AC electro-osmotic micropumps and evaluate their power-conversion efficiency. Figure 6.14 gives the minimum and maximum current consumption measured in the tested micropumps as a function of the extent of the electrodes around the channel, for an applied potential of 3 V_{pp}. The maximum value of the current that the AAE prototypes were drawing is about 530 μA_{rms}. Considering that a voltage oscillation of 3 V_{pp} corresponds to a magnitude of 1.06 V_{rms}, the power consumption of the tested micropumps, which is given by $W_{el} = I_{rms} \cdot V_{rms}$, was of about 562 μW.

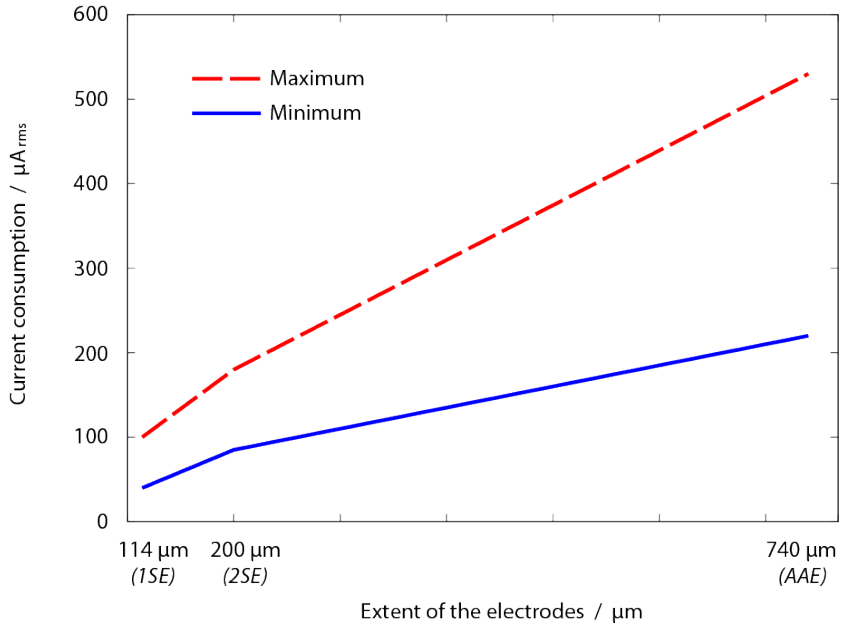

Figure 6.14: Minimum and maximum measured current flow in the tested AAE pumps as a function of the extent of the electrodes around the channel, for an applied potential of 3 V_{pp}.

Table 6.1: Comparison of the generated flow-rates, pressures and hydraulic powers, the consumed electric power and the power-conversion efficiency for the 1SE, 2SE and AAE micropumps.

	Q_{max} (nL/min)	Δp_{max} (Pa)	W_{hyd} (W)	I_{rms} (μA_{rms})	V_0 (V_{rms})	W_{el} (W)	η_{conv}
1SE	8.3	1.3	$4.6 \cdot 10^{-14}$	100	1.06	$106 \cdot 10^{-6}$	$4.3 \cdot 10^{-8}$
2SE	17.8	2.9	$2.1 \cdot 10^{-13}$	180	1.06	$191 \cdot 10^{-6}$	$1.1 \cdot 10^{-7}$
AAE	71.0	7.2	$2.1 \cdot 10^{-12}$	530	1.06	$562 \cdot 10^{-6}$	$3.8 \cdot 10^{-7}$

On the other hand, the AAE pumps were generating an equivalent flow-rate of $1.2 \cdot 10^{-12}$ m^3/s (71 nL/min) in conditions of zero backpressures, which correspond to a maximum pressure capability of 7.2 Pa. The generated hydraulic power is then given by $W_{hyd} = 0.25 Q_{max} \Delta p_{max}$ and is equal to $2.1 \cdot 10^{-12}$ W. Table 6.1 summarises the values of the generated hydraulic power

and the consumed electrical power for the 1SE, 2SE and AAE micropumps. The conversion efficiency η_{conv} is very low and much smaller than for DC electro-osmotic micropumps [30]. Several effects are responsible for such a low value of the efficiency. As has been shown in Section 5.4.2, much of the kinetic energy generated by the pumps is lost in oscillations that do not contribute to the net velocity of the liquid. Moreover, the rolls induced above the electrodes also require energy, without contributing to the net motion of the liquid.

6.5 Conclusion: more effective ACEO micropumps

Improved AC electro-osmotic micropumps, with a simple design and metal electrodes patterned on all the sides of the channel, allowed the emulation of a DC electro-osmotic flow, in agreement with the theory, and an increase in the generated flow-rate in the channel of about 360%, which corresponds to more than four times the value measured in 1SE devices. Our approach to ACEO pumping gives improvements comparable to other results published in the literature (440% velocity increase with 3D electrodes [114]), whilst relying on a simpler design and fabrication process.

The all-around-electrode prototypes were successfully fabricated using a process with only three lithographic steps, whereby an improved optical setup for the lithography enabled the realisation of well-defined metal structures on 3D surfaces and over a depth of more than 50 μm. Although the process was successfully implemented, we encountered some problems in the bonding procedure, probably due to the choice of Ta as the adhesion layer for the deposition of the Pt electrodes. We reckon that a stack of $Ti/Ta/Pt$ might be more adapted to the fusion bonding procedure, as Ti would avoid the interaction between Pyrex and Ta and Ta would prevent any diffusion of Ti into Pt.

The absolute value of the generated velocity needs to be improved in order to be able to use these pumps in real applications, which usually require much larger flow-rate and pressure capabilities. Nevertheless, the concept has been successfully demonstrated and the simple fabrication process that we developed may be applied with little or no modifications to the realisation of different electrode designs. Further improvement of the AAE ACEO micropumps must include channels with higher hydraulic resistance and electrode patterns with larger width-ratio.

7 All-Around-Electrode Micropumps on Flexible Polymer Foils

Cleanroom fabrication technologies are highly effective and allow the realisation of devices with a very high definition of the structures. But cleanrooms also represent a huge cost for MEMS producers. An approach that has been investigated for many years in order to address this issue is the fabrication of devices on plastic substrates and the use of polymeric materials and low-cost patterning techniques. A branch of science has stepped into the domain of microsystems and microelectronics, bringing new challenges and opportunities.

7.1 Introduction

All-around-electrode ACEO micropumps have proved to be a huge enhancement of the performances of simpler devices with planar designs. Nevertheless, in addition to the problem of the limited absolute value of the generated velocity, AAE devices realised on Pyrex substrates also present the disadvantage of requiring costly, though simple, processing in the cleanroom.

This chapter addresses the drawbacks of cleanroom fabrication that are connected to the costs of lithography and of the glass substrates, the low yield of the fusion-bonding procedure, and the low fabrication speed (due to the fact that only one wafer can be processed at a time). Using thin and flexible plastic foils answers the need for large-area low-cost substrates: Pyrex substrates cost about 28.- CHF a piece [162], whereas the price of a thin PET foil of equivalent area is usually less than 1.- CHF [163].

Furthermore, a process based on flexible plastic substrates can be adapted to systems for mass production such as roll-to-roll fabrication [164] or hot embossing [165], and integrated to the fabrication of devices called labs-on-a-foil [166]. This significantly simplifies the fabrication procedure and increases its yield. On the other hand, the high cost of state-of-the-art lithographic setups can be lowered by direct patterning of the structures through additive processes such as inkjet-printing.

Moving towards simpler, cheaper and larger-scale fabrication of AAE ACEO micropumps, we present a strategy to obtain electrodes that completely surround the channel by patterning

metal on very thin polyethylene terephthalate (PET) foils, and the realisation of asymmetric electrodes made of conductive polymer by inkjet-printing of poly(3,4-ethylenedioxithiopene) poly(stirenesulfonate) (PEDOT:PSS) on thicker PET substrates.

7.2 Metal electrodes on soft plastic substrates

The fabrication process to obtain the AAE pumps from Pyrex wafers included three lithographic steps, one of which required the use of special exposure optics. With bonding and DRIE, lithography is among the main sources of cost in MEMS fabrication [167], and reducing its use is an effective way of tackling the production costs of ACEO micropumps. The number of required lithographies is reduced to only one, when the metal electrodes are patterned on a very thin plastic substrate, which is subsequently folded and bonded.

Moreover, as stated before, bonding polymers is much simpler and cheaper than bonding glass [168]. Whereas the process described in Chapter 6 requires a total fabrication time (including machines and operators) of about 1 hour a chip, realising the pumps on thin PET foils allows for a dramatic reduction of processing time. The design presented in this section includes 8 chips and its fabrication requires less than 30 minutes a chip, which may be further reduced to about 5 minutes by developing a more automated process and using the same wafer design as for the Pyrex devices.

Deposition of the electrodes

PET foils from Dupont (Mylar 12 μm) were used as substrates for the deposition of asymmetric electrode arrays. Silicon wafers, to which the plastic substrates were attached with removable

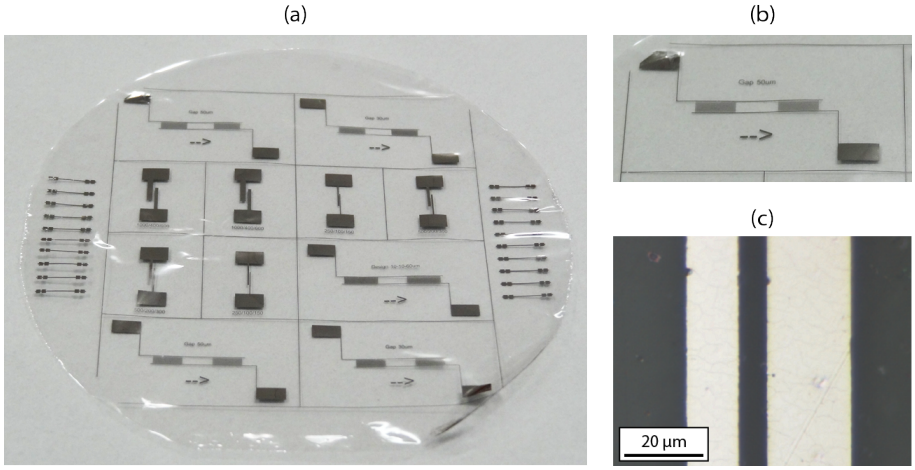

Figure 7.1: Cr/Pt asymmetric electrodes patterned by lift-off on 12-μm-thick PET foils. The wafer-size PET foil (a) is shown alongside the enlargement of one chip (b) and a picture taken with an optical microscope at 50x magnification (c).

Kapton tape, acted as support for the single lithographic step. PET foils were spin-coated with standard AZ1518 photoresist from AZ Electronic Materials, which was then patterned and used as a mask for the lift-off of the platinum electrodes. This time chromium was chosen as the adhesion layer, as we knew it to be effective on plastic substrates [169]. The resulting electrodes were a stack of 20 $nm\ Cr$ and 100 $nm\ Pt$ and are shown in Figure 7.1.

Polymer bonding

The next and final step to realise the all-around-electrode design on PET consists in folding the sheets with electrodes and bonding them with a heat and pressure treatment. In order to do this, we rolled the patterned foils around a 360-μm-wide capillary, which acted as a mould. The folded PET was then pressed between two pieces of Teflon and inserted in a custom-made bonding machine. The bonding procedure consisted in applying an initial force of about 1,800 N on the Teflon spacers, heating the system at 160 $°C$ for two hours and finally letting it cool down naturally overnight. The complete fabrication process is summarised in Figure 7.2, which also illustrates the bonding strategy.

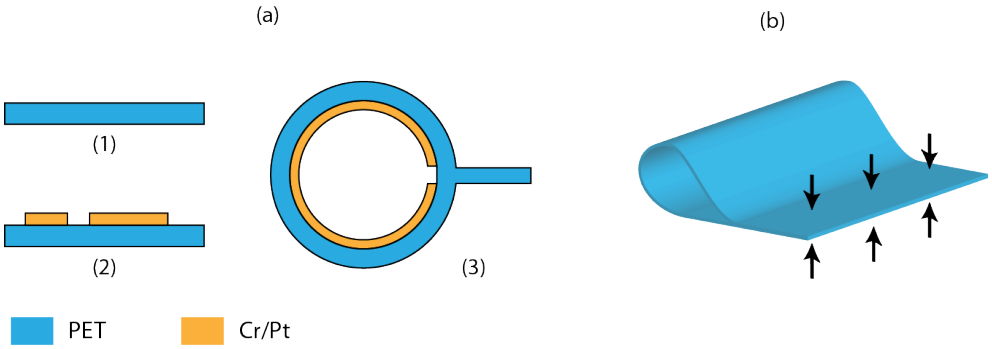

Figure 7.2: Summary of the fabrication process to obtain the PET all-around-electrode pumps (a). The concept to obtain PET channels by folding and bonding a 12-μm-thick foil is also illustrated (b).

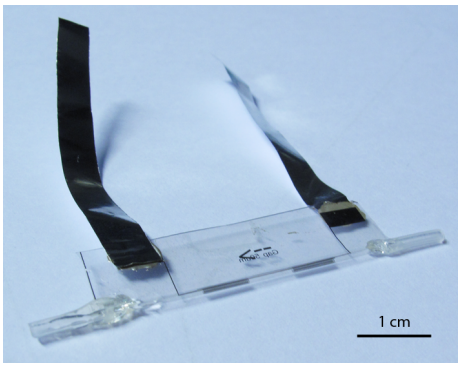

Figure 7.3: All-around-electrode ACEO micropumps fabricated by lift-off of Cr/Pt electrodes on thin PET foils, which were folded and bonded following the described procedure.

Electrical and fluidic connections for the PET pumps can easily be obtained by gluing teflon capillaries at the two ends of the channel with electrodes, and connecting Al stripes to the contact pads using Epotek H20E conductive epoxy from Epoxy Technology (Billerica, MA, USA) as for the glass-based devices. The complete prototypes with the connections are shown in Figure 7.3. Because they have a larger cross-section, these polymer pumps will exhibit an increased flow-rate capability, whilst being able to cope with smaller backpressures. Preliminary tests showed a weak velocity generation, probably due to the total hydraulic resistance of the system being comparable to that of the portion of channel with electrodes. The geometry of the channel, as well as the design of the electrodes will need to be improved in order to observe exploitable fluid velocities. More specifically, the hydraulic resistance of the portion of channel with electrodes must be much larger than for the complete system, and the electrodes must not be short-circuited by the bonding process.

7.3 Inkjet-printed electrodes

Fabricating AC electro-osmotic micropumps with Pt electrodes on thin PET foils would represent a remarkable reduction of the overall processing costs and would allow for a higher bonding precision and yield. Nonetheless, the access to the cleanroom is still expensive, even for only one step, and the lift-off process uses a much larger quantity of materials than what is really needed for the device.

Additive fabrication processes, which do not require extremely clean environments, can address these issues and enable the realisation of very low-cost devices. Among such solutions, printing techniques are particularly interesting as they can adapt to a wide range of substrates and ink materials, including polymers [170] and suspensions of metal nanoparticles. Furthermore, printing overcomes batch fabrication and allows for web-fed, continuous manufacture [171]. Three main printing techniques have been applied to microfabrication: screen printing [172], gravure printing [173] and inkjet-printing [174].

In this section we will show how electrodes for ACEO can be fabricated by inkjet-printing, whose potential for large-scale processing is clearly shown by industrial machines such as the Océ JetStream [175], which is able to print full-colour newspapers at a speed of 2 m/s. The purpose of this study is to evaluate whether inkjet-printed PEDOT:PSS has good potential as electrode material for AC electro-osmosis.

7.3.1 Inkjet printing

Provided that certain conditions in the viscosity and density are met, reported in Table 7.1, there are no further limitations to the kinds of liquids that can be printed by inkjet [176], and very conductive lines can be patterned when the cartridge is filled with a suspension of metal nanoparticles. Other types of substances that can be printed include polymers in liquid phase, which are usually diluted in either aqueous solutions or organic solvents.

Table 7.1: Properties required to be able to print a liquid by inkjet, according to the printer manufacturer's indications [176].

Viscosity	Surface tension	Boiling point	Density
10-12 cP	28-33 dynes	$> 100\,^{\circ}c$ preferred	$> 1000\ kg/m^3$ preferred

Resolution of print

The process of inkjet-printing is characterised by parameters such as the temperature of the ink and of the substrate, and the properties of the waveform applied to the print heads [177]. The dimensions of the nozzles influence the size of the jetted ink droplets which, in turn, determine the maximum resolution of the features on the printed design [178]. As mentioned previously, the main advantages of fabrication by inkjet-printing are that the process only uses the material, which is really needed to define the patterns, that it does not require any mask, since the design is printed directly, and that several layers can be printed and are self-aligned, provided that the substrate is fixed with respect to the frame of the printer. Although the resolution of printed patterns is usually worse than for standard lithography, lines as small as 5 μm can be obtained [174] and the process is relatively fast and cheap.

Printing procedure

A typical printing procedure includes the calibration of the nozzles, the jetting of the ink and a final drying step. Sometimes a post-print bake is required in order to improve the quality of the printed material. Calibrating the nozzles means choosing the shape, magnitude and frequency of the waveform used to expel the ink. This step is particularly important, as these parameters determine both the shape of the drop and the speed at which it impacts the substrate.

The machine prints the design by lines of pixels, moving either parallel or perpendicular to the orientation of the structures. As we shall see in the following sections, choosing the proper printing direction is critical for the resolution of the printed features. When the ink dries, several effects occur, which have a strong influence on the final definition and resolution of the design. On one hand, a lateral spread of the liquid determines an increase in the size of the patterns. On the other, the particles and molecules suspended in the solution tend to diffuse towards the side of the printed drop, generating a pattern known as the "coffee-ring" effect [179]. A final post-print bake is often used to complete the evaporation of the solvent and strengthen the printed material, as well as to decrease the electrical resistivity of conductive lines and elements.

7.3.2 PEDOT:PSS electrodes

Conductive polymers are promising materials for a wide range of electrical and electronic applications. As for microfluidic actuations, a few works have been published in the scientific

literature, showing the potential of PEDOT:PSS as electrode material for electro-osmosis. Erlandsson *et al.* demonstrated the use of large electrodes made of PEDOT:PSS to generate fluid motion by DC electro-osmosis [89] . In addition to presenting a very simple fabrication process, they showed that such a conductive polymer is able to stand DC voltages as large as 100 V without undergoing any electrochemical reactions with the liquid and, above all, without inducing electrolysis and generating bubbles of gas.

PEDOT for ACEO

On the other hand, Hansen *et al.* used PEDOT to fabricate planar arrays of electrodes by photolithographic patterning [108]. Their work proves that PEDOT is an appealing material for the implementation of AC electro-osmotic micropumps. As discussed in Chapter 2, Hansen's devices were able to generate liquid velocities as large as 150 $\mu m/s$ at low applied voltages.

Such interesting properties of PEDOT as electrode material, and the fact that it is well adapted to the print process [180], motivate its employment for the fabrication of ACEO electrodes by inkjet-printing.

Fabrication of the electrodes

For the fabrication of inkjet-printed electrodes, we used Clevios 100 PEDOT:PSS from H.C. Stark, which has good enough viscosity and density to be used in the printing process without needing to mix it with other solvents. We designed single pairs of asymmetric electrodes with the same width-ratio, and sizes ranging between 150 μm and 1 mm as summarised in Table 7.2. In order to verify the influence of the orientation on the size, definition and electric properties of the printed electrodes, these structures were positioned in the layout in such a way that half of the pairs were parallel and half perpendicular to the print direction.

Table 7.2: Dimensions of the asymmetric electrode pairs designed to be fabricated on PET substrates by inkjet-printing of PEDOT:PSS, and by lift-off of Cr/Pt.

Large electrode (μm)	Gap (μm)	Small electrode (μm)
1000	400	600
500	200	300
250	100	150

We realised the electrodes on 250-μm-thick PET sheets from DuPont (Melinex 506), using a Dimatix DMP-2831 inkjet printer. Figure 7.4 shows the obtained patterns: electrodes perpendicular to the print direction seem better defined than parallel ones, and with dimensions closer to the original design, as shown in Table 7.3. The structures with sizes between 300 μm and 1 mm could be successfully fabricated, whereas for smaller sizes the electrodes were not usable, due to the overlap induced by the lateral spread of the printed ink. The same phenomenon was responsible for the smaller size of the gap in larger structures. Table 7.3 shows

the dimensions of the printed electrodes. The profile of the printed material was characterised with the Wyko NT1100 white light interferometer from Veeco (Plainview, NY, USA). As Figure 7.5 shows, the average thickness of the printed PEDOT:PSS layer is about 128 nm, with peaks as high as 400 nm due to the overlap of the single ink drops within the same printed line.

Table 7.3: Measured dimensions of the electrode pairs that were fabricated by inkjet-printing of PEDOT:PSS on PET substrates. The designed size is given alongside the measured size of the structures parallel (∥) and perpendicular (⊥) to the print direction.

Large electrode (μm)			Gap (μm)			Small electrode (μm)		
Design	∥ print	⊥ print	**Design**	∥ print	⊥ print	**Design**	∥ print	⊥ print
1000	1070	1070	400	330	300	600	670	650
500	540	520	200	65	150	300	460	350
250	330	275	100	25	40	150	220	200

Cr/Pt electrodes having the same design as the printed ones were also fabricated, for comparison, by lift-off of metal on the same 250-μm-thick PET substrates. We characterised the sheet resistance of the metal and polymer electrodes with 4-probe measurements that were carried out using a 2400 Sourcemeter from Keithley (Cleveland, OH, USA) and the PM8 probe station from Süss. The average measured value for the printed PEDOT:PSS was comparable for the parallel and perpendicular structures and was about 1.88 ± 0.33 $k\Omega/sq$, while the Pt counterparts exhibited sheet resistances of about 3.20 ± 0.58 Ω/sq, which is about 500 times smaller than the values measured for conductive polymer electrodes.

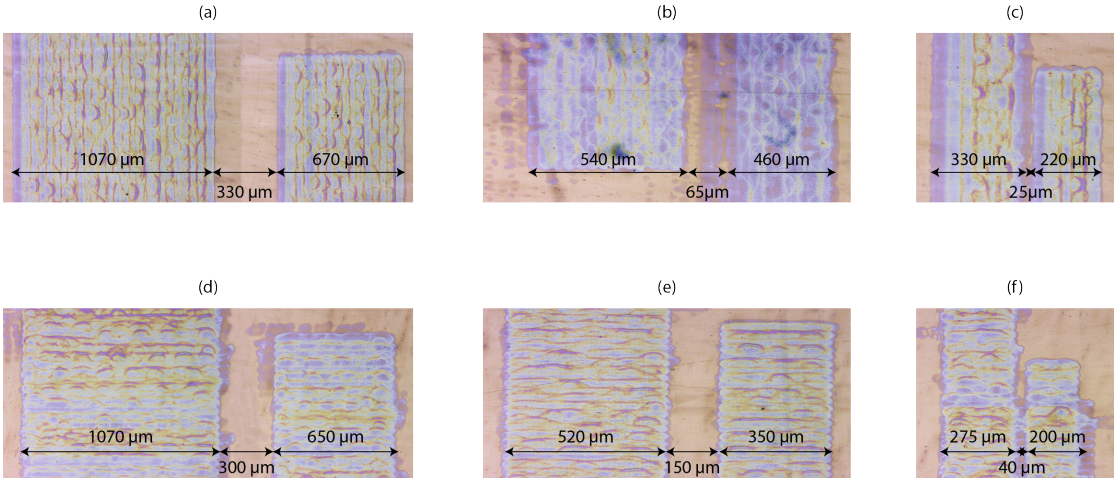

Figure 7.4: Printed electrodes made of PEDOT:PSS. The pictures were acquired with an optical microscope at 20x magnification and clearly show the differences between patterns parallel and perpendicular to the print direction. The lateral spread of the ink during the drying process can also be appreciated.

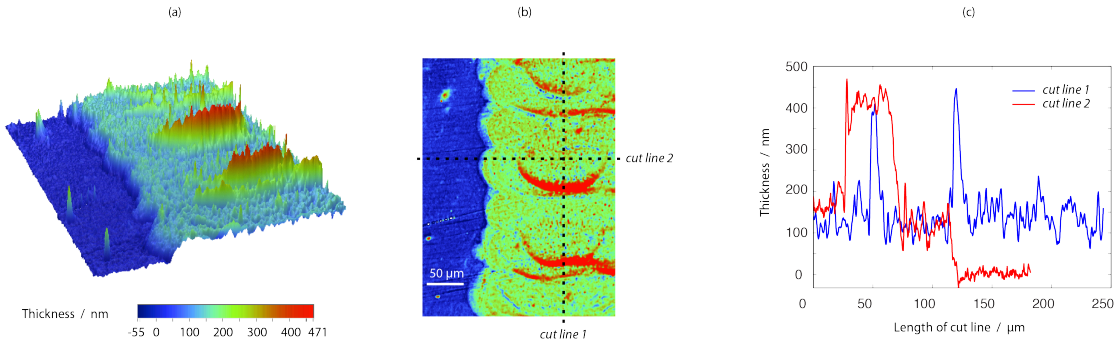

Figure 7.5: Characterisation of the thickness of the printed PEDOT:PSS electrodes. The graphs were obtained using the Wyko NT1100 white light interferometer from Veeco. The peaks in the profile of the polymer layer are due to overlapping of deposited ink droplets.

7.3.3 Capability for AC electro-osmosis

In order to evaluate the capability of inkjet-printed PEDOT:PSS electrodes for AC electro-osmosis, we realised simple devices with only one pair of electrodes by bonding PDMS channels to the printed substrates. We consider that Pt electrodes are suitable for AC electro-osmosis, as PEDOT:PSS patterns will be, if their performances are comparable to those of platinum. We measured the impedance of the devices filled with a KCl buffer at 0.01 mM and compared it to the result of the same measurement carried out on devices with Pt electrodes of the same design.

PDMS channels by rapid prototyping

Channels for the prototypes with one electrode pair were realised by casting PDMS on thick moulds made of Scotch-tape [181]. Because the fluidic performance of the device is not considered here, the shape and size of the fabricated channels do not matter. As long as the same

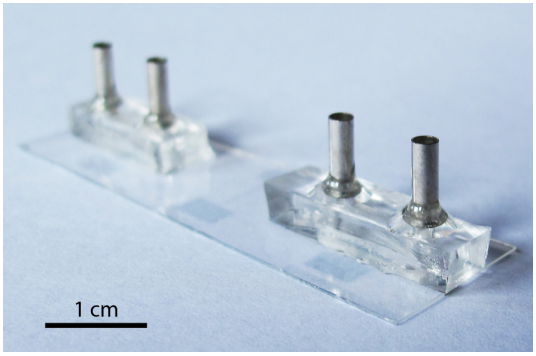

Figure 7.6: Chips with channels made of PDMS and metallic inlets glued with 2-tone epoxy. For the characterisation of the impedance, the channel was filled with the test buffer and the pads directly contacted with the probe station.

channel structure is used for all the devices under test, and the extent of the electrode surface in contact with the test buffer is constant, the comparison of the measured characteristic can be meaningful.

Access holes to the channel were punched into the PDMS chips and the channels were dropped on the substrates with electrodes without any surface treatment. By doing so, the bonding is reversible and the same channel can be used for more than one pair of electrodes. Figure 7.6 shows a picture of the bonded chips with fluidic connections. No electric connections were necessary, as the electrodes were directly contacted for the tests using a probe station.

Characterisation of the impedance

Electrical measurements to characterise the impedance of the fabricated polymer electrodes were carried out on the 500-200-300 μm electrode patterns with the Süss PM8 probe station, which we connected to the impedance analyser. Figure 7.7 shows the module and phase of the measured impedance for the three types of electrodes under test. Electrodes made of PEDOT:PSS exhibit a much lower impedance than the Pt structures. Such behaviour depends on the geometry of the fabricated structures: because the ink drops spread after being jetted onto the substrate, the electrode gap is much smaller than designed, as shown in Table 7.3. This results in a shorter electrical path from the large to the small electrode and a lower resistance of the overall system.

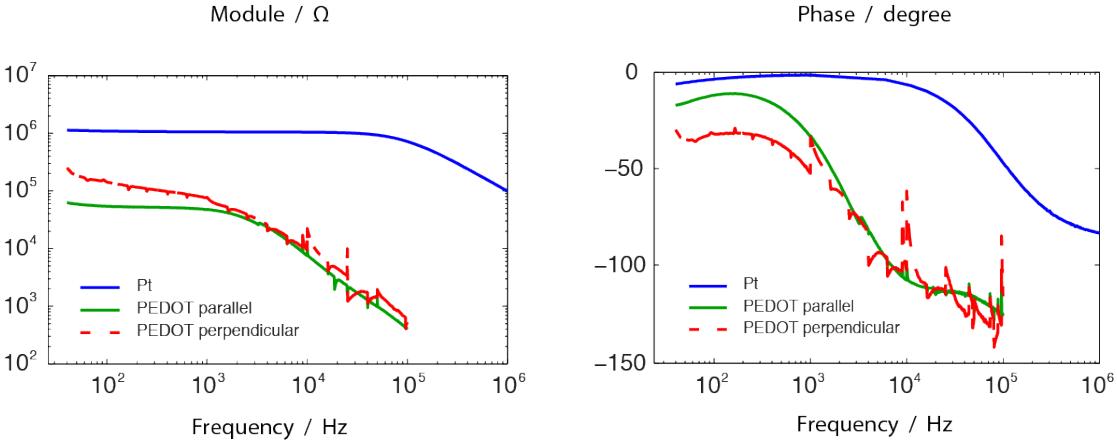

Figure 7.7: Measured impedance of the printed PEDOT:PSS electrodes in contact with a KCl solution at 0.01 mM. Only the design including a large electrode of 500 μm, a gap of 200 μm and a small electrode of 300 μm was tested. The impedance of Pt electrodes with the same design and measured with the same test buffer is given for comparison.

On the other hand, electrodes made of PEDOT:PSS exhibit much stronger non-resistive behaviour, with a pole intervening several decades before the one in the impedance of Pt structures. The difference between the polymer electrodes parallel and perpendicular to the printing direction is also clearly observable. In spite of the printed shape appearing better defined, patterns perpendicular to the print direction exhibit a noisier impedance. This can

be explained by considering the fact that the design is produced by printing parallel lines and that the ink droplets overlap due to this process. This results in electrical paths with better properties along the print directions, whereas the connection between the single printed lines has much worse qualities. Electrodes parallel to the print direction have a regular electrical path along their whole length, while the electrical path of perpendicular ones is disturbed at every printed line.

The presented measurements show that the impedance of devices based on PEDOT:PSS has a comparable shape to that of Pt electrodes and that both curves correspond well with the theoretical models defined in Chapter 3. Therefore, inkjet-printed electrodes are suitable for AC electro-osmosis. However, the impedance seems shifted towards lower frequencies and so will the optimal pumping point. Furthermore, the velocity generation strongly decreases with larger electrode sizes. Although PEDOT:PSS may allow the application of very large voltages [89], which would generate larger fluid velocities, the fabrication process must be optimised and improved to obtain features with smaller dimensions, in order to generate acceptable liquid velocities more easily.

7.4 Conclusion: towards industry

Metal deposition on thin PET substrates has allowed a rapid and effective fabrication of all-around-electrode ACEO micropumps, by reducing to one third the number of required lithographic steps and by exploiting a bonding technique with larger yield. Although the cost of partial cleanroom processing and of the evaporation of expensive metals persist, the fabrication process is much simplified.

On the other hand, there exist alternative and less costly techniques, which enable the patterning of electrodes. We have shown that inkjet-printed electrodes made of PEDOT:PSS have a good potential for AC electro-osmosis. The problem of the excessive size might be addressed by either using much smaller print nozzles or by changing the printing technique. Gravure or screen printing may for example be a better approach to the realisation of smaller electrodes.

Combining the definition of electrode patterns by printing techniques, which do not require access to the cleanroom, and the use of thin flexible substrates will enable the fabrication of AC electro-osmotic micropumps on a larger scale, consuming less time and money. Moreover, such an approach may also be applied to the realisation of a wide range of other microfluidic devices.

8 Summary and Outlook

The goal of this research was to develop and demonstrate pump concepts for the valveless actuation of liquids. Because the biomedical field represents a huge market that can potentially derive tremendous benefits from the implementation of effective and inexpensive valveless micropumps, the work has focused on electrolyte solutions and on the issue inherent to the biomedical world. The suitability of a device for such a large and demanding market depends on its long-term reliability and robustness, which can be better guaranteed by a simple fabrication process.

AC electro-osmotic micropumps with electrodes all around the pumping channel answer most of such requirements. The actuation principle is able to generate liquid velocities comparable to other devices presented in the literature, and the fabricated devices are reliable and robust, as AC electro-osmosis does not require the implementation of mechanical components. Moreover, a fabrication process with only three lithographic steps enabled the realisation of improved devices with 3D electrodes, which were able to generate velocities four times larger than their planar counterparts.

Applications for the pump

The developed devices can effectively pump liquids with low conductivity, whereas they fail to generate sufficient flow-rates and pressures with more concentrated buffers such as the ones used in biomedical applications. There is however much room for the application of the all-around-electrode concept to improved electrode and channel designs. For example, a significant increase in the pumping performances may result from the implementation of electrodes with larger width-ratios or from the parallel connection of several channels with high hydraulic resistance.

On the other hand, our pumps are suitable for applications exploiting poorly conductive polar liquids or where the conductivity of the liquid is not relevant, such as cooling systems. Furthermore, several studies have shown the possibility of using different liquids within the same pump [182, 183, 184] and our devices could be used for indirect pumping in a

configuration where a dilute buffer is used to push or pull a more concentrated one.

Industrial fabrication

As for the fabrication process, the procedure for the complete realisation of the pumps with cleanroom technologies is simple, with only three lithographic steps, yet rather expensive. The tests carried out with alternative manufacturing approaches on thin plastic substrates and using conductive polymers show an interesting potential for industrial fabrication. Using thin plastic foils, in fact, simplifies the realisation of the all-around electrodes and improves the speed and quality of the bonding process, while the possibility of defining conductive patterns by printing polymers or suspensions of metal nanoparticles opens the way to rapid and low-cost batch fabrication.

Outlook

Future work aiming at the improvement of the devices and processes presented in this thesis should be organised around three main axes. First it should focus on the use of flexible plastic substrates as an effective means to obtain electrodes with tridimensional geometries. Second, fabricating arrays of channels with large hydraulic resistance will provide a way of ameliorating the fluidic performance of the devices. Improved designs may also include wider yet thinner channels or other geometries, such as spirals and serpentines, allowing for an increase of the pressure capabilities whilst maintaining large flow-rates. Finally, the electrodes should be modified to optimise the velocity generation. Possible directions to investigate include changing their width ratio, decreasing the overall size (provided that the lithography allows for it) and adding a thin insulating layer, which would avoid any electrochemical reaction at the surface and allow for the application of larger potentials, thus increasing the generated velocity.

We demonstrated a simple and effective way of improving AC electro-osmotic pumps and proposed different approaches to the microfabrication of the devices. Our concept can be applied to any design of the system and of the electrodes, and can be the basis for the development of improved pumping devices. The opportunities linked to the implementation of all-around-electrode AC electro-osmostic micropumps, which are easy to realise and well adapted to large-scale industrial production, will lead to a new generation of simpler and more effective valveless micropumps.

A Matlab scripts

All Matlab [140] scripts prepared for simulations or data processing are presented here. First, we show the code used to simulate the onset of DC electro-osmosis with the Lattice-Boltzmann method, whose results are presented in Section 3.3. Then we present the code used to compute the approximated solutions to the Navier-Stokes equation in a channel with square cross-section and where a constant velocity is generated in turn on one, two, or all sides, as discussed in Section 3.5. Finally the scripts used to process the data of particle image velocimetry obtained from the Tracker [150] for the experiments in Chapter 5 and Chapter 6.

A.1 Lattice-Boltzmann simulation of DCEO flow generation

The Lattice-Boltzmann method allows the implementation of fluid simulations through the computation of the behaviour of the single particles that constitute the system [125]. A script to simulate the phenomenon of electro-osmosis should couple the standard Navier-Stokes equations [1] and the Poisson equation [119] describing the evolution of the charge density. The present simulation was inspired by the work of Wang *et al.* [127, 128] and Guo *et al.* [126], where two different simulation lattices were superposed: one for the solution of the Navier-Stokes equations and one for the Poisson equation.

Nevertheless, in order to have a simpler simulation, we will consider the charge density to be constant in time and we will calculate it *a priori*. This approximation will not lead to significant errors as long as the stream potential generated by the ion movement along the channel is negligible respect to the applied external potential and pressure.

The script simulates the temporal evolution of the velocity across the cross-section of a rectangular channel. Such a domain is represented by a series of matrices (lattices), on which the computations are carried out. At every step, the fluid density and velocity are computed for all the points in the lattice, considering the value of the parameters in the previous step as well as the total force applied on the particles. According to [127], a term proportional to the

applied electrical force should be added in the collision equation, which becomes

$$f_{out} = f_{in} - \omega(f_{in} - f_{eq}) + F \cdot f_{eq}, \tag{A.1}$$

where the force term accounting for the applied potential and the backpressure, has the dimensions of an acceleration and is given by

$$F = \frac{-\nabla p + \rho_e E}{\rho}. \tag{A.2}$$

```
clear;

% PHYSICAL CONSTANTS %%%%%%%%%%%%%%%%%
kB    = 1.38e-23; % Boltzmann constant
T     = 293; % Absolute temperature
eps0  = 8.854e-12; % Vacuum permittivity
e     = 1.6e-19; % Electron charge
Na    = 6.023e23; % Avogadro number

% SYSTEM CONSTANTS %%%%%%%%%%%%%%%%%%
E        = 0; % Applied electric field (V/m)
gradP    = 100/5e-5; % Pressure gradient across the channel (Pa/m)
n        = 1e-4*1000; % Buffer concentration (mol/m3)
epsr     = 78; % Relative permittivity
zc       = [1, -1]; % Ion valence
z        = 1;
zeta     = 0.030; % Zeta potential on channel walls (V)
etaReal  = 1e-6; % kinematic viscosity
Is       = 0.5*n*sum(zc.^2); % Ionic strength of the solution

% REFERENCE LATTICE VARIABLES %%%%%%%%%%%
lambdaD = sqrt( epsr*eps0*kB*T / (2*Na*Is*e^2) ); % Debye length (m)
l0            = 0.5e-6;
N             = 500;
delta_x       = l0 / N; % m
Vt            = kB*T/e; % thermal potential (V)
delta_t       = 10^(-12); % s
u0            = delta_x / delta_t; % m/s

% OTHER LATTICE AND SIMULATION CONSTANTS
ly            = N;
lx            = 5; % aspect_ratio*ly;
Ex            = E; % x-component of applied E field, physical units
```

```
Ey            = 0; % y-component of applied E field
gradPx        = gradP * ones(1,lx,ly); % x-component of P gradient
cs            = 1/sqrt(3); % Sound velocity
chi           = 1; % Potential diffusivity
nu            = etaReal * delta_t / delta_x^2; % LB viscosity
omegaBoltz    = 1./(3*nu + 0.5); % Relaxation for fluid

% SIMULATION PARAMETERS %%%%%%%%%%%%%%
endTime       = 500000;
tPlot         = 50000; % Iterations between graphical outputs

% D2Q9 LATTICE CONSTANTS for Navier-Stokes equations %
tBoltz   = [4/9, 1/9,1/9,1/9,1/9, 1/36,1/36,1/36,1/36];
cxBoltz  = [  0,   1,  0, -1,  0,    1,  -1,  -1,   1];
cyBoltz  = [  0,   0,  1,  0, -1,    1,   1,  -1,  -1];
oppBoltz = [  1,   4,  5,  2,  3,    8,   9,   6,   7];

% Grid definition %%%%%%%%%%%%%%%%%%%%%%
[y,x] = meshgrid(1:ly,1:lx);

% INITIAL CONDITION FOR FLUID rho=1, u=0 => fIn(i)=t(i) %%
fIn = reshape( tBoltz' * ones(1,lx*ly), 9, lx, ly);

% Computation of the POTENTIAL ACROSS THE CHANNEL %
r=0:1:ly-1; r=r*delta_x;
pot=(4*Vt/z)*atanh(tanh(z*zeta/(4*Vt))*exp(-r/lambdaD));
pot2=(4*Vt/z)*atanh(tanh(z*zeta/(4*Vt))*exp((r-max(r))/lambdaD));
psi = zeros(1,lx,ly);
for i=1:lx,
    psi(1,i,:)=pot+pot2; %physical unit
end;
rho_e  = ( 2*z*e*n*Na .* sinh( z .* psi / Vt) ) ; % physical units

% VISUALISATION INITIALISATION
vid = avifile('ux2.avi', 'fps', 50);
vid2 = avifile('uxProfile2.avi', 'fps', 50);

% MAIN LOOP %%%%%%%%%%%%%%%%%%%%%%%%
for iter=1:endTime
    rho   = sum(fIn);
    ux    = reshape ( (cxBoltz * reshape(fIn,9,lx*ly)), 1,lx,ly) ./rho;
    uy    = reshape ( (cyBoltz * reshape(fIn,9,lx*ly)), 1,lx,ly) ./rho;
```

```
    % COLLISION STEP FLUID %%%%%%%%%%%%%%%
    for i=1:9
        cuBoltz       = (cxBoltz(i).*ux+cyBoltz(i).*uy);
        fEq(i,:,:)    =  tBoltz(i) .* ( 1 + 3*cuBoltz + ...
            9/2*(cuBoltz.*cuBoltz) - 3/2*(ux.^2 + uy.^2) );
    Fex   = (rho_e*Ex - gradPx) /1000 * delta_t^2 / delta_x; %lattice units
    Fey   = (rho_e*Ey - gradPx) /1000 * delta_t^2 / delta_x; %lattice units
        force(i,:,:)  = 3 * ( Fex .* (cxBoltz(i)-ux(1,:,:)) + ...
            Fey .* (cyBoltz(i)-uy(1,:,:)) ) .* fEq(i,:,:);
        fOut(i,:,:)   = fIn(i,:,:) - ...
            omegaBoltz .* (fIn(i,:,:)-fEq(i,:,:)) + force(i,:,:);
    end;

    % STREAMING STEP FLUID %%%%%%%%%%%%%%
    for i=1:9
        fIn(i,:,:) = circshift(fOut(i,:,:), [0, cxBoltz(i), cyBoltz(i)]);
    end;

    % MICROSCOPIC BOUNDARY CONDITIONS FOR FLUID
    for i=1:9
        fIn(i,:,1)   = fOut(oppBoltz(i),:,1); % No-slip on channel walls
        fIn(i,:,ly)  = fOut(oppBoltz(i),:,ly);
    end;

    % VISUALISATION %%%%%%%%%%%%%%%%%%%
    if ((iter<tPlot & mod(iter,100)==0) || mod(iter,tPlot)==0)
        uxg   = reshape(ux,lx,ly); % horizontal velocity
        fig1=figure(1);
        imagesc(uxg); colorbar; title('X-Velocity'); % surface plot
        fr = getframe(fig1);
        vid = addframe(vid,fr);
        fig2=figure(2);
        plot(uxg(floor(lx/2),:)); title('X-Velocity profile'); % profile plot
        saveas(fig2, ['ux',int2str(iter) ,'.fig']);
        fr = getframe(fig2);
        vid2 = addframe(vid2,fr);
    end;

end;

vid = close(vid);
```

```
vid2 = close(vid2);
```

A.2 Simulation of the frequency dependence of velocity generation

We simulated the dependence of the generated velocity on the applied AC frequency. The present scripts computes the average generated on the electrode surface according to the theory presented by Brown *et al.* [136] for the one-side-electrode design presented in Chapter 5. The displayed plot accounts for the parameters introduced in Chapter 3 and defining the maximum velocity of the Poiseuille flow generated in the observation region, i.e. the velocity that we measured.

```
clear all

%%% physical constants %%%
pi = pi();
eps0 = 8.85e-12; %vacuum permittivity
epsr = 80; %relative permittivity (water @ 20 degree)
eta = 1.003e-3; %viscosity
sigma = 2.5e-6/1e-2; %conductivity S/m
T = 293; %absolute temperature
kBoltzmann = 1.38e-23; %Boltzmann constant
e = 1.6e-19; %electron charge
Na = 6.022e23; %Avogadro number
c0 =0.01e-3*1000; % concentration mol/m3 ;
Z = 1; % ion valence, assuming we have K+ and Cl- ions

%%% design parameters %%%
L = 25e-6; % large electrode length
S = 15e-6; % small electrode length
G = 10e-6; % inter electrode gap
h = 50e-6; % channel height
ltot = 3e-2; % channel length
lpair = 2*(L+G+S); %spatial period of the array
larray = 100*100e-6; %length of the electrode array
lel = L*larray/lpair; % only the L electrode generates fwd velocity
gamma = lel/ltot; % ratio electrode along the channel to channel length
sidesElectr = 1; % sides with electrodes
beta = sidesElectr/4; % factor for average velocity above electrodes

%%% derived parameters %%%
k = L/S;
```

```
xmax = (G+L+S) /( sqrt(k) + 1/sqrt(k)) %normalised electrode end coord.
xmin = G /( sqrt(k) + 1/sqrt(k)) %normalised electrode start coordinate

%Debye length
lambdaD = sqrt( eps0*epsr*kBoltzmann*T / (2*(Z^2)*(e^2)*c0*Na) );

%% Equation parameters
vL0 = eps0*epsr / (2*eta*sqrt(k)*(1+k)^2); % maximum velocity
omega0 = 2*lambdaD*sigma / (eps0*epsr*pi); % optimal angular freq.

%%% computations (as a function of frequency) %%%
f = 0:0.01:10000; % frequency
o = 2*pi*f; % angular frequency

K1 = Psi0^2 * vL0 / (2 * (xmax-xmin));
K2 = ((o*sqrt(xmin*xmax)/omega0).^2) * (xmax/xmin-xmin/xmax);

k1 = (sqrt(xmin*xmax)/omega0)^2;
k2 = (sqrt(xmin*xmax)/omega0)^2;
K3 = (k1*o.^2+xmin/xmax) .* (k2*o.^2+xmax/xmin);

vLave = K1 * K2 ./ K3; % average velocity on electrode surface

semilogx(f,vLave*beta*gamma) % plot max velocity of Poiseuille flow
```

A.3 Approximated solutions to the Navier-Stokes equation

Section 3.5 presented the theoretical proof that the performances of AC electro-osmosis are enhanced by generating the velocity on all the sides of the channel. In order to provide such proof we considered a channel with square cross-section as in Figure A.1 and solved the Navier-Stokes equation

$$\eta \nabla^2 v(y,z) = 0 \tag{A.3}$$

for the different sets of boundary conditions shown in Table A.1.

The solutions to Equation A.3 can be easily computed when the velocity is non-zero only on side of the channel [145]. Because the equation is linear, the solution when the velocity is non-zero on two (respectively all) sides of the channel is obtained through the superposition of the single solutions to the problems where the velocity is generated, in turn, on each side of the channel.

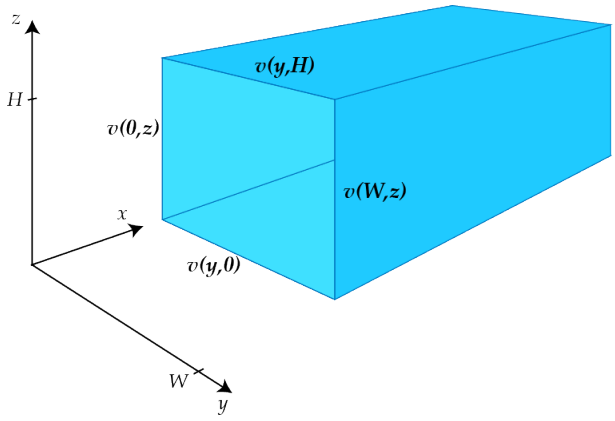

Figure A.1: Channel structure considered for the theoretical analysis and simulation of multi-side ACEO flows.

Table A.1: Boundary conditions for the Navier-Stokes equation, for the one-side- (1SE), two-side- (2SE) and all-around-electrode (AAE) configurations.

	1SE	2SE	AAE
$v(y,0)$	v_{aceo}	v_{aceo}	v_{aceo}
$v(0,z)$	0	0	v_{aceo}
$v(y,H)$	0	v_{aceo}	v_{aceo}
$v(W,z)$	0	0	v_{aceo}

For the boundary conditions $v(y,0) = v_{aceo}$, $v(0,z) = v(y,H) = v(W,z) = 0$, the velocity distribution is given by

$$v_1(y,z) = \sum_{n=1}^{\infty} \frac{2v_{aceo}(1-\cos(n\pi))}{n\pi} \sin\frac{n\pi y}{W} \frac{\sinh\frac{n\pi(H-z)}{W}}{\sinh\frac{n\pi H}{W}}. \tag{A.4}$$

When the boundary conditions are $v(y,H) = v_{aceo}$, $v(0,z) = v(y,0) = v(W,z) = 0$, the velocity field is described by

$$v_2(y,z) = \sum_{n=1}^{\infty} \frac{2v_{aceo}(1-\cos(n\pi))}{n\pi} \sin\frac{n\pi y}{W} \frac{\sinh\frac{n\pi z}{W}}{\sinh\frac{n\pi H}{W}}. \tag{A.5}$$

On the other hand, for $v(0,z) = v_{aceo}$, $v(y,0) = v(y,H) = v(W,z) = 0$, the velocity distribution is given by

$$v_3(y,z) = \sum_{n=1}^{\infty} \frac{2v_{aceo}(1-\cos(n\pi))}{n\pi} \sin\frac{n\pi z}{H} \frac{\sinh\frac{n\pi(W-y)}{H}}{\sinh\frac{n\pi W}{H}}, \tag{A.6}$$

and for $v(W,z) = v_{aceo}$, $v(0,z) = v(y,H) = v(y,0) = 0$, the velocity distribution is given by

$$v_4(y,z) = \sum_{n=1}^{\infty} \frac{2v_{aceo}(1-\cos(n\pi))}{n\pi} \sin\frac{n\pi z}{H} \frac{\sinh\frac{n\pi y}{H}}{\sinh\frac{n\pi W}{H}}. \tag{A.7}$$

The script approximates the four velocity distributions to the 100^{th} term of the series and computes the solutions of the velocity field over the cross-section of 1SE, 2SE and AAE devices as $v_{1SE} = v_1$, $v_{2SE} = v_1 + v_2$ and $v_{AAE} = v_1 + v_2 + v_3 + v_4$. In order to simplify the code, we considered that $\cos(n\pi) = (-1)^n$.

```
clear;

nmax = 100; % number of terms of the series to be computed
H = 100; % channel height
W = 100; % channel width
u0 = 100; % velocity condition on the boundaries

% definition of the y coordinates
yi = 0:0.05:W; y=yi'*ones(1,length(yi)); y=y';
% definition of the z coordinates
zi = H:-0.05:0; z=zi'*ones(1,length(zi));

%% ONE-SIDE
u1=zeros(length(zi),length(yi)); % set to 0 the initial solution
%compute  approximated solution to problem A
for n=1:nmax,
    c1 = 2*u0*(1-(-1)^n)/(n*pi()*sinh(n*pi()*H/W)); % nth coefficient
    un = c1 * sin(n*pi()*y/W) .* sinh(n*pi()*(H-z)/W); % nth term
    u1 = u1 + un; % total velocity
end;
figure, imagesc(u1), colorbar % plot the solution


%% TWO-SIDE
u2=zeros(length(zi),length(yi)); % set to 0 the initial solution
%compute the approximated solution to problem B
for n=1:nmax,
    c2 = 2*u0*(1-(-1)^n)/(n*pi()*sinh(n*pi()*H/W)); % nth coefficient (B)
    un =  c2 * sin(n*pi()*y/W) .* sinh(n*pi()*z/W); % nth term (B)
    u2 = u2 + un; % total velocity (B)
end;
u2 = u2 + u1; % the solution is the sum of solutions A and B
```

```
figure, imagesc(u2),colorbar % plot the solution


%% ALL-AROUND
ua=zeros(length(zi),length(yi)); % set to 0 the initial solution
%compute the approximated solution to problem C and D
for n=1:nmax,
    c3 = 2*u0*(1-(-1)^n)/(n*pi()*sinh(n*pi()*W/H)); % nth coefficient (C)
    c4 = 2*u0*(1-(-1)^n)/(n*pi()*sinh(n*pi()*W/H)); % nth coefficient (D)
    un3 =  c3 * sin(n*pi()*z/H) .* sinh(n*pi()*(W-y)/H); % nth term (C)
    un4 =  c4 * sin(n*pi()*z/H) .* sinh(n*pi()*y/H); % nth term (C)
    ua = ua + un3 + un4; % total velocity (C and D)
end;
ua = ua + u2; % the solution is the sum of all solutions (A to D)
figure, imagesc(ua), colorbar % plot the solution
```

A.4 Data processing for μPIV

After performing micro particle image velocimetry with the Tracker, we obtained text files containing the information about the time, position and velocity of the tracked particles. More precisely, such a text file has one column for the time, one for the x-coordinate, one for the x-velocity and one for the y-velocity. In order to process the data with Matlab, the file is imported into the workspace by using the function `importfileTracker`. Because the Tracker computes the velocity of the particles by considering the difference between two subsequent x positions, the data include `NaN` (not-a-number) values corresponding to the first and last element of the velocity array, where the previous and next position of the particles are unknown.

For each value of frequency used in the experiments, the script for data processing calls the `importfileTracker` function, eliminates the `NaN` values and computes the average value of the velocity. Finally, it builds an array with all the mean velocities and plots it against the frequency on a semi-logarithmic scale.

Importing the files generated by the Tracker into Matlab

```
function importfileTracker(fileToRead1, prefix)
%  IMPORTFILE1(FILETOREAD1)
%  Imports data from the specified file
%  FILETOREAD1:  file to read

% Import the file
newData1 = importdata(fileToRead1);
```

```
% Define variable names (add or remove as necessary)
% t=time, x=x_coord, y=y_coord, u=x_vel, v=y_vel, w=mod_vel
suffix = ['t','x','u','v'];

% Create new variables in the base workspace from those fields
for i = 1:size(newData1.colheaders, 2)
    assignin('base', strcat(prefix,suffix(i)), newData1.data(:,i));
end
```

Process data and plot graphs

```
folder = './ExpData/'; % data folder on hard disk
prototype = 's2b001'; % device (s1, s2, aa) and buffer (b001, b01, b1)
acvolt='v3f'; % applied voltage
freq=[20,50,100,150,200,500,1000,2000,5000]; % frequency sweep
error = 0.05; % 5% relative error on measured velocity

for i=1:length(freq),
% import files
   fileToImport = strcat(folder, acvolt, num2str(freq(i)) ,'.txt');
   prefix = strcat(prototype, '_', acvolt, num2str(freq(i)), '_');
   importfileTracker(fileToImport, prefix)
% convert NaN in 0
   velVar = strcat( prefix,'u');
   eval( strcat( velVar, '(isnan(', velVar, '))', ' = 0;' ) )
% compute averages
   avVelVar = strcat( prototype, '_', acvolt, num2str(freq(i)), '_avu');
   eval( strcat(avVelVar, ' = mean(', velVar,');') )
end;

%% prepare curve vel(f) and error e(f)
avVelArray = strcat( prototype, '_', acvolt(1:2), 'u');
velToAdd = strcat( prototype, '_', acvolt, num2str(freq(1)), '_avu' );
eval( strcat( avVelArray, '=', velToAdd,';' ));
for i=2:length(freq),
    velToAdd = strcat( prototype, '_', acvolt, num2str(freq(i)), '_avu' );
    eval( strcat( avVelArray, ' = [', avVelArray, ', ', velToAdd, '];' ) )
end;

%% plot curve vel(f)
eval( strcat( 'errorbar(freq,', avVelArray, ',' , avVelArray, '*error)' ))
```

Bibliography

[1] H. Bruus, *Theoretical Microfluidics*. Oxford University Press, 2008.

[2] M. Brivio, W. Verboom, and D. N. Reinhoudt, "Miniaturized continuous flow reaction vessels: Influence on chemical reactions," *Lab on a Chip*, vol. 6, no. 3, pp. 329–344, 2006.

[3] D. Figeys and D. Pinto, "Lab-on-a-chip: A revolution in biological and medical sciences," *Analytical Chemistry*, vol. 72, no. 9, pp. 330A–335A, 2000.

[4] C. Rivet, H. Lee, A. Hirsch, S. Hamilton, and H. Lu, "Microfluidics for medical diagnostics and biosensors," *Chemical Engineering Science*, vol. 66, no. 7, pp. 1490–1507, 2011.

[5] P. S. Dittrich and A. Manz, "Lab-on-a-chip: Microfluidics in drug discovery," *Nature Reviews Drug Discovery*, vol. 5, no. 3, pp. 210–218, 2006.

[6] J. Atencia and D. J. Beebe, "Controlled microfluidic interfaces," *Nature*, vol. 437, no. 7059, pp. 648–655, 2005.

[7] A. Allievi, "Microsensor concept based on interfacial liquid-liquid microwave flow in a microfluidic channel," *Journal of Micromechanics and Microengineering*, vol. 15, no. 12, pp. 2326–2338, 2005.

[8] D. Psaltis, S. R. Quake, and C. Yang, "Developing optofluidic technology through the fusion of microfluidics and optics," *Nature*, vol. 442, no. 7101, pp. 381–386, 2006.

[9] C. J. Campbell and B. A. Grzybowski, "Microfluidic mixers: From microfabricated to self-assembling devices," *Philosophical Transactions of the Royal Society A: Mathematical, Physical and Engineering Sciences*, vol. 362, no. 1818, pp. 1069–1086, 2004.

[10] A. K. Agarwal, S. S. Sridharamurthy, D. J. Beebe, and H. Jiang, "Programmable autonomous micromixers and micropumps," *Journal of Microelectromechanical Systems*, vol. 14, no. 6, pp. 1409–1421, 2005.

[11] E. Verpoorte and N. F. De Rooij, "Microfluidics meets MEMS," *Proceedings of the IEEE*, vol. 91, no. 6, pp. 930–953, 2003.

[12] A. Manz, N. Graber, and H. M. Widmer, "Miniaturized total chemical analysis systems: A novel concept for chemical sensing," *Sensors and Actuators B: Chemical*, vol. 1, no. 1-6, pp. 244–248, 1990.

[13] D. Erickson and D. Li, "Integrated microfluidic devices," *Analytica Chimica Acta*, vol. 507, no. 1, pp. 11–26, 2004.

[14] P. Mitchell, "Microfluidics - downsizing large-scale biology. To what extent has microfluidics technology fulfilled life science researchers' expectations of creating a viable "lab-on-a-chip"?," *Nature Biotechnology*, vol. 19, no. 8, pp. 717–721, 2001.

[15] C. R. Buie, J. D. Posner, T. Fabian, S.-W. Cha, D. Kim, F. B. Prinz, J. K. Eaton, and J. G. Santiago, "Water management in proton exchange membrane fuel cells using integrated electroosmotic pumping," *Journal of Power Sources*, vol. 161, no. 1, pp. 191–202, 2006.

[16] B. S. Pivovar, "An overview of electro-osmosis in fuel cell polymer electrolytes," *Polymer*, vol. 47, no. 11, pp. 4194–4202, 2006.

[17] V. Singhal, S. V. Garimella, and A. Raman, "Microscale pumping technologies for microchannel cooling systems," *Applied Mechanics Reviews*, vol. 57, no. 1-6, pp. 191–221, 2004.

[18] J. K. Luo, Y. Q. Fu, Y. Li, X. Y. Du, A. J. Flewitt, A. J. Walton, and W. I. Milne, "Moving-part-free microfluidic systems for lab-on-a-chip," *Journal of Micromechanics and Microengineering*, vol. 19, no. 5, p. 054001, 2009.

[19] F. Amirouche, Y. Zhou, and T. Johnson, "Current micropump technologies and their biomedical applications," *Microsystem Technologies*, vol. 15, no. 5, pp. 647–666, 2009.

[20] E. L. P. Uhlig, W. F. Graydon, and W. Zingg, "The electro-osmotic actuation of implantable insulin micropumps," *Journal of Biomedical Materials Research*, vol. 17, no. 6, pp. 931–943, 1983.

[21] R. A. M. Receveur, F. W. Lindemans, and N. F. de Rooij, "Microsystem technologies for implantable applications," *Journal of Micromechanics and Microengineering*, vol. 17, no. 5, pp. R50–R80, 2007.

[22] "Pump meters micro volumes," *Chemical and Engineering News*, vol. 32, no. 5, pp. 440–442, 1954.

[23] W. J. Spencer, W. T. Corbett, L. R. Dominguez, and B. D. Shafer, "An electronically controlled piezoelectric insulin pump and valves," *IEEE Transactions on Sonics and Ultrasonics*, vol. 25, no. 3, pp. 153 –156, 1978.

[24] H. T. G. van Lintel, F. C. M. van De Pol, and S. Bouwstra, "A piezoelectric micropump based on micromachining of silicon," *Sensors and Actuators*, vol. 15, no. 2, pp. 153–167, 1988.

[25] N. T. Nguyen, X. Y. Huang, and T. K. Chuan, "Mems-micropumps: A review," *Journal of Fluids Engineering*, vol. 124, no. 2, pp. 384–392, 2002.

[26] D. J. Laser and J. G. Santiago, "A review of micropumps," *Journal of Micromechanics and Microengineering*, vol. 14, no. 6, pp. R35–R64, 2004.

[27] B. D. Iverson and S. V. Garimella, "Recent advances in microscale pumping technologies: a review and evaluation," *Microfluidics and Nanofluidics*, vol. 5, no. 2, pp. 145–174, 2008.

[28] H. Q. Li, D. C. Roberts, J. L. Steyn, K. T. Turner, J. A. Carretero, O. Yaglioglu, L. Saggere, N. W. Hagood, S. M. Spearing, M. Schmidt, R. Mlcak, and K. S. Breuer, "A high frequency high flow rate piezoelectrically driven MEMS micropump," *Structure*, vol. June, pp. 69–72, 2000.

[29] S. P. Beeby, M. J. Tudor, and N. M. White, "Energy harvesting vibration sources for microsystems applications," *Measurement Science and Technology*, vol. 17, no. 12, pp. R175–R195, 2006.

[30] C. H. Chen and J. G. Santiago, "A planar electroosmotic micropump," *Journal of Microelectromechanical Systems*, vol. 11, no. 6, pp. 672–683, 2002.

[31] J. S. Hu and C. Y. H. Chao, "A study of the performance of microfabricated electroosmotic pump," *Sensors and Actuators A: Physical*, vol. 135, no. 1, pp. 273–282, 2007.

[32] J. M. Berg, R. Anderson, M. Anaya, B. Lahlouh, M. Holtz, and T. Dallas, "A two-stage discrete peristaltic micropump," *Sensors and Actuators, A: Physical*, vol. 104, no. 1, pp. 6–10, 2003.

[33] K.-P. Kamper, J. Dopper, W. Ehrfeld, and S. Oberbeck, "A self-filling low-cost membrane micropump," in *11th Annual International Workshop on Micro Electro Mechanical Systems. MEMS 98*, pp. 432–437, 1998.

[34] M. Esashi, S. Shoji, and A. Nakano, "Normally closed microvalve and mircopump fabricated on a silicon wafer," *Sensors and Actuators*, vol. 20, no. 1-2, pp. 163 – 169, 1989.

[35] R. Zengerle, J. Ulrich, S. Kluge, M. Richter, and A. Richter, "A bidirectional silicon micropump," *Sensors and Actuators A: Physical*, vol. 50, no. 1-2, pp. 81–86, 1995.

[36] M. Khoo and C. Liu, "A novel micromachined magnetic membrane microfluid pump," in *22nd Annual International Conference of the IEEE Engineering in Medicine and Biology Society*, vol. 3, pp. 2394 –2397, 2000.

[37] S. Santra, P. Holloway, and C. D. Batich, "Fabrication and testing of a magnetically actuated micropump," *Sensors and Actuators B: Chemical*, vol. 87, no. 2, pp. 358 – 364, 2002.

[38] O. Français and I. Dufour, "Dynamic simulation of an electrostatic micropump with pull-in and hysteresis phenomena," *Sensors and Actuators, A: Physical*, vol. 70, no. 1-2, pp. 56–60, 1998.

[39] M. A. Unger, H.-P. Chou, T. Thorsen, A. Scherer, and S. R. Quake, "Monolithic microfabricated valves and pumps by multilayer soft lithography," *Science*, vol. 288, no. 5463, pp. 113–116, 2000.

[40] J. H. Kim, K. H. Na, C. J. Kang, and Y. S. Kim, "A disposable thermopneumatic-actuated micropump stacked with pdms layers and ito-coated glass," *Sensors and Actuators A: Physical*, vol. 120, no. 2, pp. 365–369, 2005.

[41] P. Lemaire, L. Metref, F. Bianchi, and P. Renaud, "On-chip thermopneumatic actuation system for coagulation time measurement," in *Eurosensors XIII*, vol. 1, pp. 521–524, 2009.

[42] W. H. Song and J. Lichtenberg, "Thermo-pneumatic, single-stroke micropump," *Journal of Micromechanics and Microengineering*, vol. 15, no. 8, p. 1425, 2005.

[43] Debiotech SA, "MIP implantable: main performance specification." http://www.debiotech.com/, 2011.

[44] Debiotech SA, "Disposable insulin nanopump from debiotech and stmicroelectronics marks major breakthrough in diabetes treatment." http://www.debiotech.com/, April 2007.

[45] Bartels Mikrotechnik GmbH, "No space for compromises: Bartels micro pump mp6." http://www.micro-components.com/, 2011.

[46] P. K. Yuen, "Smartbuild-a truly plug-n-play modular microfluidic system," *Lab on a Chip*, vol. 8, pp. 1374–1378, 2008.

[47] L. Gervais, *Capillary Microfluidic Chips for Point-of-Care Testing*. PhD thesis, Ecole Polytechnique Fédérale de Lausanne, Lausanne, 2011.

[48] M. Joanicot and A. Ajdari, "Droplet control for microfluidics," *Science*, vol. 309, no. 5736, pp. 887–888, 2005.

[49] F. Mugele and J.-C. Baret, "Electrowetting: From basics to applications," *Journal of Physics Condensed Matter*, vol. 17, no. 28, pp. R705–R774, 2005.

[50] J. Zeng and T. Korsmeyer, "Principles of droplet electrohydrodynamics for lab-on-a-chip," *Lab on a Chip*, vol. 4, pp. 265–277, 2004.

[51] S. K. Cho, H. Moon, and C.-J. Kim, "Creating, transporting, cutting, and merging liquid droplets by electrowetting-based actuation for digital microfluidic circuits," *Journal of Microelectromechanical Systems*, vol. 12, pp. 70 – 80, feb 2003.

[52] B. Berge and J. Peseux, "Variable focal lens controlled by an external voltage: An application of electrowetting," *European Physical Journal E*, vol. 3, no. 2, pp. 159–163, 2000.

[53] R. A. Hayes and B. J. Feenstra, "Video-speed electronic paper based on electrowetting," *Nature*, vol. 425, no. 6956, pp. 383–385, 2003.

[54] R. B. Fair, "Digital microfluidics: Is a true lab-on-a-chip possible?," *Microfluidics and Nanofluidics*, vol. 3, no. 3, pp. 245–281, 2007.

[55] C. S. Zhang, D. Xing, and Y. Y. Li, "Micropumps, microvalves, and micromixers within PCR microfluidic chips: Advances and trends," *Biotechnology Advances*, vol. 25, no. 5, pp. 483–514, 2007.

[56] Y. Q. Fu, X. Y. Du, J. K. Luo, A. J. Flewitt, W. I. Milne, D. S. Lee, N. M. Park, S. Maeng, S. H. Kim, Y. J. Choi, and J. Park, "SAW streaming in ZnO surface acoustic wave micromixer and micropump," *IEEE Sensors*, vol. 1-3, pp. 478–483, 2007.

[57] S. Girardo, M. Cecchini, F. Beltram, R. Cingolani, and D. Pisignano, "Polydimethylsiloxane-LiNbO3 surface acoustic wave micropump devices for fluid control into microchannels," *Lab on a Chip - Miniaturisation for Chemistry and Biology*, vol. 8, no. 9, pp. 1557–1563, 2008.

[58] X. Y. Du, Y. Q. Fu, S. C. Tan, J. K. Luo, A. J. Flewitt, W. I. Milne, D. S. Lee, N. M. Park, J. Park, Y. J. Choi, S. H. Kim, and S. Maeng, "ZnO film thickness effect on surface acoustic wave modes and acoustic streaming," *Applied Physics Letters*, vol. 93, no. 9, 2008.

[59] R. Shilton, M. K. Tan, L. Y. Yeo, and J. R. Friend, "Particle concentration and mixing in microdrops driven by focused surface acoustic waves," *Journal of Applied Physics*, vol. 104, no. 1, p. 014910, 2008.

[60] L. Schmid, A. Wixforth, D. A. Weitz, and T. Franke, "Novel surface acoustic wave (SAW)-driven closed PDMS flow chamber," *Microfluidics and Nanofluidics*, vol. 9, pp. 1–7, 2011. Article in Press.

[61] C. Yamahata, M. Chastellain, V. K. Parashar, A. Petri, H. Hofmann, and M. A. M. Gijs, "Plastic micropump with ferrofluidic actuation," *Journal of Microelectromechanical Systems*, vol. 14, no. 1, pp. 96–102, 2005.

[62] A. V. Lemoff and A. P. Lee, "An ac magnetohydrodynamic micropump," *Sensors and Actuators B: Chemical*, vol. 63, no. 3, pp. 178 – 185, 2000.

[63] M. C. Weston, M. D. Gerner, and I. Fritsch, "Magnetic fields for fluid motion," *Analytical Chemistry*, vol. 82, no. 9, pp. 3411–3418, 2010.

[64] J. Jang and S. Lee, "Theoretical and experimental study of MHD (magnetohydrodynamic) micropumps," *Sensors and Actuators A: Physical*, vol. 80, no. 1, pp. 84 – 89, 2000.

[65] A. Homsy, S. Koster, J. C. T. Eijkel, A. van den Berg, F. Lucklum, E. Verpoorte, and N. F. de Rooij, "A high current density DC magnetohydrodynamic (MHD) micropumps," *Lab on a Chip*, vol. 5, no. 4, pp. 466–471, 2005.

[66] A. Homsy, V. Linder, F. Lucklum, and N. F. de Rooij, "Magnetohydrodynamic pumping in nuclear magnetic resonance environments," *Sensors and Actuators B: Chemical*, vol. 123, no. 1, pp. 636–646, 2007.

[67] J. C. T. Eijkel, C. Dalton, C. J. Hayden, J. P. H. Burt, and A. Manz, "A circular AC magnetohydrodynamic micropump for chromatographic applications," *Sensors and Actuators B: Chemical*, vol. 92, no. 1-2, pp. 215 – 221, 2003.

[68] J. West, B. Karamata, B. Lillis, J. P. Gleeson, J. Alderman, J. K. Collins, W. Lane, A. Mathewson, and H. Berney, "Application of magnetohydrodynamic actuation to continuous flow chemistry," *Lab on a Chip*, vol. 2, pp. 224–230, 2002.

[69] A. Richter and H. Sandmaier, "An electrohydrodynamic micropumps," *Micro Electro Mechanical Systems*, vol. 3rd Workshop on Micro Electro Mechanical Systems. MEMS 90. February 11-14, 1990, Napa Valley, CA, USA, pp. 99–104, 1990.

[70] A. Richter, A. Plettner, K. A. Hofmann, and H. Sandmaier, "A micromachined electrohydrodynamic (ehd) pump," *Sensors and Actuators A: Physical*, vol. 29, no. 2, pp. 159–168, 1991.

[71] M. Felten, P. Geggier, M. Jäger, and C. Duschl, "Controlling electrohydrodynamic pumping in microchannels through defined temperature fields," *Physics of Fluids*, vol. 18, no. 5, p. 051707, 2006.

[72] J. Darabi and H. Wang, "Development of an electrohydrodynamic injection micropump and its potential application in pumping fluids in cryogenic cooling systems," *Journal of Microelectromechanical Systems*, vol. 14, no. 4, pp. 747–755, 2005.

[73] D. B. Go, S. V. Garimella, T. S. Fisher, and R. K. Mongia, "Ionic winds for locally enhanced cooling," *Journal of Applied Physics*, vol. 102, no. 5, p. 053302, 2007.

[74] S. Moghaddam and M. M. Ohadi, "Effect of electrode geometry on performance of an EHD thin-film evaporator," *Journal of Microelectromechanical Systems*, vol. 14, no. 5, pp. 978–986, 2005.

[75] J. W. Jorgenson and K. D. Lukacs, "High-resolution separations based on electrophoresis and electroosmosis," *Journal of Chromatography A*, vol. 218, no. 0, pp. 209 – 216, 1981.

[76] S. C. Jacobson, R. Hergenröder, L. B. Koutny, and M. J. Ramsey, "Open channel electrochromatography on a microchip," *Analytical Chemistry*, vol. 66, no. 14, pp. 2369–2373, 1994.

[77] A. Ramos, H. Morgan, N. G. Green, and A. Castellanos, "AC electrokinetics: a review of forces in microelectrode structures," *Journal of Physics D - Applied Physics*, vol. 31, no. 18, pp. 2338–2353, 1998.

[78] A. Ramos, H. Morgan, N. G. Green, A. Gonzalez, and A. Castellanos, "Pumping of liquids with traveling-wave electroosmosis," *Journal of Applied Physics*, vol. 97, no. 8, p. 084906, 2005.

[79] W. E. Morf, O. T. Guenat, and N. F. de Rooij, "Partial electroosmotic pumping in complex capillary systems - part 1: Principles and general theoretical approach," *Sensors and Actuators B: Chemical*, vol. 72, no. 3, pp. 266–272, 2001.

[80] O. T. Guenat, D. Ghiglione, W. E. Morf, and N. F. de Rooij, "Partial electroosmotic pumping in complex capillary systems - part 2: Fabrication and application of a micro total analysis system (μTAS) suited for continuous volumetric nanotitrations," *Sensors and Actuators B: Chemical*, vol. 72, no. 3, pp. 273–282, 2001.

[81] S. L. Zeng, C. H. Chen, J. C. Mikkelsen, and J. G. Santiago, "Fabrication and characterization of electroosmotic micropumps," *Sensors and Actuators B: Chemical*, vol. 79, no. 2-3, pp. 107–114, 2001.

[82] L. X. Chen, H. L. Wang, J. P. Ma, C. X. Wang, and Y. F. Guan, "Fabrication and characterization of a multi-stage electroosmotic pump for liquid delivery," *Sensors and Actuators B: Chemical*, vol. 104, no. 1, pp. 117–123, 2005.

[83] L. X. Chen, Q. L. Li, S. Lee, and J. Choo, "Development of an electroosmotic pump using nanosilica particle packed capillary," *IEEE Sensors Journal*, vol. 8, no. 5-6, pp. 488–494, 2008.

[84] T. T. Razunguzwa and A. T. Timperman, "Fabrication and characterization of a frit-less microfabricated electroosmotic pump with reduced pH dependence," *Analytical Chemistry*, vol. 76, no. 5, pp. 1336–1341, 2004.

[85] Y. Takamura, H. Onoda, H. Inokuchi, S. Adachi, A. Oki, and Y. Horiike, "Low-voltage electroosmosis pump for stand-alone microfluidics devices," *Electrophoresis*, vol. 24, no. 1-2, pp. 185–192, 2003.

[86] P. Prakash, M. D. Grissom, C. D. Rahn, and A. L. Zydney, "Development of an electroosmotic pump for high performance actuation," *Journal of Membrane Science*, vol. 286, no. 1-2, pp. 153–160, 2006.

[87] S. K. Vajandar, D. Y. Xu, D. A. Markov, J. P. Wikswo, W. Hofmeister, and D. Y. Li, "SiO2-coated porous anodic alumina membranes for high flow rate electroosmotic pumping," *Nanotechnology*, vol. 18, no. 27, p. 275705, 2007.

[88] K. Seibel, L. Scholer, H. Schafer, and M. Bohm, "A programmable planar electroosmotic micropump for lab-on-a-chip applications," *Journal of Micromechanics and Microengineering*, vol. 18, no. 2, p. 025008, 2008.

[89] P. G. Erlandsson and N. D. Robinson, "Electrolysis-reducing electrodes for electrokinetic devices," *Electrophoresis*, vol. 32, no. 6-7, pp. 784–790, 2011.

[90] C. Arvind and P. Muthukumaran, "Geometrical tuning of microdiffuser/nozzle for valveless micropumps," *Journal of Micromechanics and Microengineering*, vol. 21, no. 4, p. 045035, 2011.

[91] A. Ramos, H. Morgan, N. G. Green, and A. Castellanos, "Ac electric-field-induced fluid flow in microelectrodes," *Journal of Colloid and Interface Science*, vol. 217, no. 2, pp. 420–422, 1999.

[92] S. Mutlu, C. Yu, P. Selvaganapathy, F. Svec, C. H. Mastrangelo, and J. M. J. Frechet, "Micromachined porous polymer for bubble free electro-osmotic pump," *15th IEEE International Conference on Micro Electro Mechanical Systems. MEMS 2002. January 20-24, 2002, Las Vegas, NV, USA*, pp. 19–23, 2002.

[93] A. Brask, D. Snakenborg, J. P. Kutter, and H. Bruus, "AC electroosmotic pump with bubble-free palladium electrodes and rectifying polymer membrane valves," *Lab on a Chip*, vol. 6, no. 2, pp. 280–288, 2006.

[94] E. J. van der Wouden, D. C. Hermes, J. G. E. Gardeniers, and A. van den Berg, "Directional flow induced by synchronized longitudinal and zeta-potential controlling AC-electrical fields," *Lab on a Chip*, vol. 6, no. 10, pp. 1300–1305, 2006.

[95] N. A. Mishchuk, T. Heldal, T. Volden, J. Auerswald, and H. Knapp, "Micropump based on electroosmosis of the second kind," *Electrophoresis*, vol. 30, no. 20, pp. 3499–3506, 2009.

[96] N. Mishchuk, T. Heldal, T. Volden, J. Auerswald, and H. Knapp, "Microfluidic pump based on the phenomenon of electroosmosis of the second kind," *Microfluidics and Nanofluidics*, vol. 11, pp. 675–684, 2011.

[97] Osmotex AG, "Osmotex micro- and nanopumps." http://www.osmotex.ch/en/technology/osmotex_pumps/, 2011.

[98] S. Debesset, C. J. Hayden, C. Dalton, J. C. T. Eijkel, and A. Manz, "An AC electroosmotic micropump for circular chromatographic applications," *Lab on a Chip*, vol. 4, no. 4, pp. 396–400, 2004.

[99] V. Studer, A. Pepin, Y. Chen, and A. Ajdari, "An integrated AC electrokinetic pump in a microfluidic loop for fast and tunable flow control," *Analyst*, vol. 129, no. 10, pp. 944–949, 2004.

[100] W. Y. Ng, Y. C. Lam, and I. Rodriguez, "Experimental verification of faradaic charging in AC electrokinetics," *Biomicrofluidics*, vol. 3, no. 2, p. 022405, 2009.

[101] A. Gonzalez, A. Ramos, P. García-Sánchez, and A. Castellanos, "Effect of the combined action of faradaic currents and mobility differences in AC electro-osmosis," *Physical Review E*, vol. 81, no. 1, p. 016320, 2010.

[102] N. Loucaides, A. Ramos, and G. Georghiou, "Novel systems for configurable AC electroosmotic pumping," *Microfluidics and Nanofluidics*, vol. 3, no. 6, pp. 709–714, 2007.

[103] N. Loucaides, A. Ramos, and G. Georghiou, "Configurable AC electroosmotic pumping and mixing," *Microelectronic Engineering*, vol. 90, pp. 47–50, 2012. Article in Press.

[104] S.-H. Huang, H.-J. Hsueh, and K.-Y. Hung, "Configurable AC electroosmotic generated in-plane microvortices and pumping flow in microchannels," *Microfluidics and Nanofluidics*, vol. 8, no. 2, pp. 187–195, 2010.

[105] P. García-Sánchez, A. Ramos, N. G. Green, and H. Morgan, "Experiments on AC electrokinetic pumping of liquids using arrays of microelectrodes," *IEEE Transactions on Dielectrics and Electrical Insulation*, vol. 13, no. 3, pp. 670–677, 2006.

[106] H. Yang, H. Jiang, A. Ramos, and P. García-Sánchez, "AC electrokinetic pumping on symmetric electrode arrays," *Microfluidics and Nanofluidics*, vol. 7, no. 6, pp. 767–772, 2009.

[107] K. Xie, Y. Lai, X. Guo, and R. J. Campbell, "A three phase serpentine micro electrode array for AC electroosmotic flow pumping," *Microsystem Technologies*, vol. 16, no. 10, pp. 1825–1830, 2010.

[108] T. S. Hansen, K. West, O. Hassager, and N. B. Larsen, "An all-polymer micropump based on the conductive polymer poly(3,4-ethylenedioxythiophene) and a polyurethane channel system," *Journal of Micromechanics and Microengineering*, vol. 17, no. 5, pp. 860–866, 2007.

[109] C.-C. Huang, M. Z. Bazant, and T. Thorsen, "Ultrafast high-pressure AC electro-osmotic pumps for portable biomedical microfluidics," *Lab on a Chip*, vol. 10, no. 1, pp. 80–85, 2010.

[110] W. Hilber, B. Weiss, A. Saeed, R. Holly, and B. Jakoby, "Density-dependent particle separation in microchannels using 3D AC-driven electro-osmotic pumps," *Sensors and Actuators, A: Physical*, vol. 156, no. 1, pp. 115–120, 2009.

[111] Y. M. Senousy and C. K. Harnett, "Fast three dimensional AC electro-osmotic pumps with nonphotolithographic electrode patterning," *Biomicrofluidics*, vol. 4, no. 3, pp. 1–7, 2010.

[112] X. Guo, K. Xie, R. J. Campbell, and Y. Lai, "A study on three-dimensional electrode arrays fabricated by PolyMUMPs for AC electro-osmotic pumping," *Microelectronic Engineering*, vol. 88, no. 10, pp. 3113–3118, 2011.

[113] X. Guo, Y. Lai, K. Xie, and R. J. Campbell, "Discrete 3D T-shaped electrode arrays for moving liquid by AC electro-osmosis," *Advanced Materials Research*, vol. 254, pp. 78–81, 2011.

[114] H. A. Rouabah, B. Y. Park, R. B. Zaouk, H. Morgan, M. J. Madou, and N. G. Green, "Design and fabrication of an AC electro-osmosis micropump with 3D high-aspect-ratio electrodes using only SU-8," *Journal of Micromechanics and Microengineering*, vol. 21, no. 3, p. 035018, 2011.

[115] J.-L. Chen, W.-H. Shih, and W.-H. Hsieh, "Three-dimensional non-linear AC electro-osmotic flow induced by a face-to-face, asymmetric pair of planar electrodes," *Microfluidics and Nanofluidics*, vol. 9, no. 2-3, pp. 579–584, 2010.

[116] D. Lee, G. Xu, Y. Tng, K. Z. Htet, C. Yang, and J. Ying, "Large distance liquid pumping by ac electro-osmosis for the delivery of biological cells and reagents in microfluidic devices," in *SPIE*, vol. 6836, 2008.

[117] K.-L. Yang, S. Yiacoumi, and C. Tsouris, *Dekker Encyclopedia of Nanoscience and Nanotechnology*, ch. Electrical Double-Layer Formation, pp. 1001–1014. Marcel Dekker, 2004.

[118] R. H. Doremus, Y. Mehrotra, W. A. Lanford, and C. Burman, "Reaction of water with glass: influence of a transformed surface layer," *Journal of Materials Science*, vol. 18, pp. 612–622, 1983.

[119] D. Halliday and R. Resnick, *Principles of Physics*. Wiley, international student version, 9th ed., 2011.

[120] J. S. Hu and C. Y. H. Chao, "Numerical study of electroosmotic (EO) flow in microfabricated EO pump with overlapped electrical double layer (EDL)," *International Journal of Refrigeration - Revue Internationale Du Froid*, vol. 30, no. 2, pp. 290–298, 2007.

[121] M. S. Kilic, M. Z. Bazant, and A. Ajdari, "Steric effects in the dynamics of electrolytes at large applied voltages. I. double-layer charging," *Physical Review E*, vol. 75, no. 2, p. 021502, 2007.

[122] M. S. Kilic, M. Z. Bazant, and A. Ajdari, "Steric effects in the dynamics of electrolytes at large applied voltages. II. modified poisson-nernst-planck equations," *Physical Review E*, vol. 75, no. 2, p. 021503, 2007.

[123] M. Z. Bazant and T. M. Squires, "Induced-charge electrokinetic phenomena," *Current Opinion in Colloid and Interface Science*, vol. 15, no. 3, pp. 203–213, 2010.

[124] P. Pham, M. Howorth, A. Planat-Chrétien, and S. Tardu, "Numerical simulation of the electrical double layer based on the poisson-boltzmann models for AC electroosmosis flows," in *Proceedings of the COMSOL Users Conference, Grenoble*, 2007.

[125] M. C. Sukop and D. T. Thorne, *Lattice Boltzmann Modeling; an Introduction for Geoscientists and Engineers*. Springer-Verlag Berlin/Heidelberg, 2006.

[126] Z. L. Guo, T. S. Zhao, and Y. Shi, "A lattice boltzmann algorithm for electro-osmotic flows in microfluidic devices," *Journal of Chemical Physics*, vol. 122, no. 14, p. 094908, 2005.

[127] J. K. Wang, M. Wang, and Z. X. Li, "Lattice poisson-boltzmann simulations of electro-osmotic flows in microchannels," *Journal of Colloid and Interface Science*, vol. 296, no. 2, pp. 729–736, 2006.

[128] M. Wang, J. K. Wang, S. Y. Chen, and N. Pan, "Electrokinetic pumping effects of charged porous media in microchannels using the lattice poisson-boltzmann method," *Journal of Colloid and Interface Science*, vol. 304, no. 1, pp. 246–253, 2006.

[129] S. Pennathur and J. G. Santiago, "Electrokinetic transport in nanochannels. 1. Theory," *Analytical Chemistry*, vol. 77, no. 21, pp. 6772–6781, 2005.

[130] S. Pennathur and J. G. Santiago, "Electrokinetic transport in nanochannels. 2. Experiments," *Analytical Chemistry*, vol. 77, no. 21, pp. 6782–6789, 2005.

[131] F. Z. Tian, B. M. Li, and D. Y. Kwok, "Lattice boltzmann simulation of electroosmotic flows in micro- and nanochannels," in *International Conference on MEMS, Nano and Smart Systems. August 25-27, 2004. Banff, Canada.*, pp. 294–299, 2004.

[132] P. Atkins and J. de Paula, *Physical Chemistry*, vol. 1. W. H. Freeman, 9th ed., 2010.

[133] D. Pletcher, *A first course on electrode processes.* The Electrochemical Consultancy, 1991.

[134] W. Haynes, ed., *CRC Handbook of Chemistry and Physics.* CRC Press, 92nd ed., 2012.

[135] A. Ramos, A. Gonzalez, A. Castellanos, N. G. Green, and H. Morgan, "Pumping of liquids with AC voltages applied to asymmetric pairs of microelectrodes," *Physical Review E*, vol. 67, no. 5, p. 056302, 2003.

[136] A. B. D. Brown, C. G. Smith, and A. R. Rennie, "Pumping of water with AC electric fields applied to asymmetric pairs of microelectrodes," *Physical Review E*, vol. 63, no. 1, p. 016305, 2001.

[137] N. G. Green, A. Ramos, A. Gonzalez, H. Morgan, and A. Castellanos, "Fluid flow induced by nonuniform ac electric fields in electrolytes on microelectrodes. i. experimental measurements," *Physical Review E*, vol. 61, no. 4, pp. 4011–4018, 2000.

[138] A. Gonzalez, A. Ramos, N. G. Green, A. Castellanos, and H. Morgan, "Fluid flow induced by nonuniform AC electric fields in electrolytes on microelectrodes. II. A linear double-layer analysis," *Physical Review E*, vol. 61, no. 4, pp. 4019–4028, 2000.

[139] N. G. Green, A. Ramos, A. Gonzalez, H. Morgan, and A. Castellanos, "Fluid flow induced by nonuniform ac electric fields in electrolytes on microelectrodes. iii. observation of streamlines and numerical simulation," *Physical Review E*, vol. 66, no. 2, p. 026305, 2002.

[140] Mathworks, "Matlab - the language of technical computing." http://www.mathworks.com/products/matlab/index.html, 2011.

[141] J. Lichtenberg, *A Microchip-based Ion Analysis System Incorporating Electrophoretic Separation, Conductivity Detection, and Sample Pretreatment.* PhD thesis, Institute of Microtechnology, University of Neuchâtel, 2002.

[142] A. Castellanos, A. Ramos, A. Gonzalez, N. G. Green, and H. Morgan, "Electrohydrodynamics and dielectrophoresis in microsystems: scaling laws," *Journal of Physics D: Applied Physics*, vol. 36, no. 20, pp. 2584–2597, 2003.

[143] D. Burch and M. Z. Bazant, "Design principle for improved three-dimensional AC electroosmotic pumps," *Physical Review E*, vol. 77, no. 5, p. 055303, 2008.

[144] M. M. Gregersen, L. H. Olesen, A. Brask, M. F. Hansen, and H. Bruus, "Flow reversal at low voltage and low frequency in a microfabricated AC electrokinetic pumps," *Physical Review E*, vol. 76, no. 5, p. 056305, 2007.

[145] P. J. Olver, "Introduction to partial differential equations." http://www.math.umn.edu/~olver/pdn.html, 2011.

[146] L. Ribetto, A. Homsy, and N. F. de Rooij, "Flow recirculation when pumping fluids with ac electroomosis," in *5th Asia-Pacific Conference on Transducers and Micro-Nano Technology. APCOT 2010. Perth.*, 2010.

[147] L. H. Olesen, , H. Bruus, and A. Ajdari, "AC electrokinetic micropumps: the effect of geometrical confinement, faradaic current injection, and nonlinear surface capacitance," *Physical Review E*, vol. 73, no. 5, p. 056313, 2006.

[148] J. G. Santiago, S. T. Wereley, C. D. Meinhart, D. J. Beebe, and R. J. Adrian, "A particle image velocimetry system for microfluidics," *Experiments in Fluids*, vol. 25, no. 4, pp. 316–319, 1998.

[149] S. Devasenathipathy, J. G. Santiago, S. T. Wereley, C. D. Meinhart, and K. Takehara, "Particle imaging techniques for microfabricated fluidic systems," *Experiments in Fluids*, vol. 34, no. 4, pp. 504–514, 2003.

[150] D. Brown, "The tracker: Video analysis and modeling tool." http://www.cabrillo.edu/~dbrown/tracker/, 2011.

[151] M. Drosg, "Basics on uncertainties (errors)," in *Dealing with Uncertainties*, pp. 15–31, Springer Berlin Heidelberg, 2007.

[152] H. B. Bull, "Electrokinetics. XV. The use of inert electrodes in measuring the streaming potential," *Journal of the American Chemical Society*, vol. 57, no. 2, pp. 259–260, 1935.

[153] P. Wägli, A. Homsy, and N. F. de Rooij, "Norland optical adhesive (NOA81) microchannels with adjustable wetting behavior and high chemical resistance against a range of mid-infrared-transparent organic solvents," *Sensors and Actuators B: Chemical*, vol. 156, no. 2, pp. 0994–1001, 2011.

[154] D. Bartolo, G. Degre, P. Nghe, and V. Studer, "Microfluidic stickers," *Lab on a Chip*, vol. 8, no. 2, pp. 274–279, 2008.

[155] Y. J. Kang, C. Yang, and X. Y. Huang, "Dynamic aspects of electroosmotic flow in a cylindrical microcapillary," *International Journal of Engineering Science*, vol. 40, no. 20, pp. 2203–2221, 2002.

[156] Y. J. Kang, C. Yang, and X. Y. Huang, "AC electroosmosis in microchannels packed with a porous medium," *Journal of Micromechanics and Microengineering*, vol. 14, no. 8, pp. 1249–1257, 2004.

[157] Y. C. Marcos, K. T. Ooi, T. N. Wong, and J. H. Masliyah, "Frequency-dependent laminar electroosmotic flow in a closed-end rectangular microchannel," *Journal of Colloid and Interface Science*, vol. 275, no. 2, pp. 679–698, 2004.

[158] Y. L. Zhang, T. N. Wong, C. Yang, and K. T. Ooi, "Dynamic aspects of electroosmotic flow," *Microfluidics and Nanofluidics*, vol. 2, no. 3, pp. 205–214, 2006.

[159] H. Nyquist, "Certain topics in telegraph transmission theory," *Proceedings of the IEEE*, vol. 90, no. 2, pp. 280 –305, 2002.

[160] A. Daridon, V. Fascio, J. Lichtenberg, R. Wütrich, H. Langen, E. Verpoorte, and N. F. de Rooij, "Multi-layer microfluidic glass chips for microanalytical applications," *Fresenius' Journal of Analytical Chemistry*, vol. 371, pp. 261–269, 2001.

[161] R. M. Tiggelaar, R. G. P. Sanders, A. W. Groenland, and J. G. E. Gardeniers, "Stability of thin platinum films implemented in high-temperature microdevices," *Sensors and Actuators A: Physical*, vol. 152, no. 1, pp. 39 – 47, 2009.

[162] CMi - EPFL Centre of Micronanotechnology, "Consumable pricelist." http://cmi.epfl.ch, 2011.

[163] Goodfellow Cambridge Ltd., "Online catalogue." http://www.goodfellow.com/catalogue/GFCatalogue.php?Language=E, 2011.

[164] A. L. Vig, T. Mäkelä, P. Majander, V. Lambertini, J. Ahopelto, and A. Kristensen, "Roll-to-roll fabricated lab-on-a-chip devices," *Journal of Micromechanics and Microengineering*, vol. 21, no. 3, p. 035006, 2011.

[165] L. P. Yeo, S. H. Ng, Z. F. Wang, H. M. Xia, Z. P. Wang, V. S. Thang, Z. W. Zhong, and N. F. de Rooij, "Investigation of hot roller embossing for microfluidic devices," *Journal of Micromechanics and Microengineering*, vol. 20, no. 1, p. 015017, 2010.

[166] M. Focke, D. Kosse, C. Muller, H. Reinecke, R. Zengerle, and F. von Stetten, "Lab-on-a-foil: microfluidics on thin and flexible films," *Lab on a Chip*, vol. 10, no. 11, pp. 1365–1386, 2010.

[167] R. Lawes, "Manufacturing costs for microsystems/MEMS using high aspect ratio microfabrication techniques," *Microsystem Technologies*, vol. 13, pp. 85–95, 2007.

[168] H. Becker and C. Gärtner, "Polymer microfabrication methods for microfluidic analytical applications," *Electrophoresis*, vol. 21, no. 1, pp. 12–26, 2000.

[169] J. Courbat, *Gas Sensors on Plastic Foil with Reduced Power Consumption for Wireless Applications*. PhD thesis, Ecole Polytechnique Fédérale de Lausanne (EPFL), 2010.

[170] B. Weng, R. L. Shepherd, K. Crowley, A. J. Killard, and G. G. Wallace, "Printing conducting polymers," *Analyst*, vol. 135, no. 11, pp. 2779–2789, 2010.

[171] J. Miettinen, V. Pekkanen, K. Kaija, P. Mansikkamäki, J. Mäntysalo, M. Mäntysalo, J. Niittynen, J. Pekkanen, T. Saviauk, and R. Rönkkä, "Inkjet printed system-in-package design and manufacturing," *Microelectronics Journal*, vol. 39, no. 12, pp. 1740–1750, 2008.

[172] J. Wang, B. Tian, V. B. Nascimento, and L. Angnes, "Performance of screen-printed carbon electrodes fabricated from different carbon inks," *Electrochimica Acta*, vol. 43, no. 23, pp. 3459–3465, 1998.

[173] H. W. Kang, H. J. Sung, T.-M. Lee, D.-S. Kim, and C.-J. Kim, "Liquid transfer between two separating plates for micro-gravure-offset printing," *Journal of Micromechanics and Microengineering*, vol. 19, no. 1, p. 015025, 2009.

[174] H. Sirringhaus, T. Kawase, R. H. Friend, T. Shimoda, M. Inbasekaran, W. Wu, and E. P. Woo, "High-resolution inkjet printing of all-polymer transistor circuits," *Science*, vol. 290, no. 5499, pp. 2123–2126, 2000.

[175] Océ, "Jetstream compact series." http://global.oce.com/products/jetstream-compact-series/, 2011.

[176] Fujifilm Dimatix, "Jettable fluid formulation guidelines." http://www.dimatix.com/files/Dimatix-Materials-Printer-Jettable-Fluid-Formulation-Guidelines.pdf, 2011.

[177] M. H. Tsai, W. S. Hwang, H. H. Chou, and P. H. Hsieh, "Effects of pulse voltage on inkjet printing of a silver nanopowder suspension," *Nanotechnology*, vol. 19, no. 33, p. 335304, 2008.

[178] Y. Wang and J. Bokor, "Ultra-high-resolution monolithic thermal bubble inkjet print head," *Journal of Micro/Nanolithography, MEMS, and MOEMS*, vol. 6, no. 4, p. 043009, 2007.

[179] R. D. Deegan, O. Bakajin, T. F. Dupont, G. Huber, S. R. Nagel, and T. A. Witten, "Capillary flow as the cause of ring stains from dried liquid drops," *Nature*, vol. 389, no. 6653, pp. 827–829, 1997.

[180] T. Kawase, T. Shimoda, C. Newsome, H. Sirringhaus, and R. H. Friend, "Inkjet printing of polymer thin film transistors," *Thin Solid Films*, vol. 438-439, pp. 279–287, 2003.

[181] A. B. Shrirao and R. Perez-Castillejos, "Simple fabrication of microfluidic devices by replicating scotch-tape masters." http://blogs.rsc.org/chipsandtips/2010/05/17/simple-fabrication-of-microfluidic-devices-by-replicating-scotch-tape-masters/, May 2010.

[182] A. Brask, G. Goranovic, M. J. Jensen, and H. Bruus, "A novel electro-osmotic pump design for nonconducting liquids: theoretical analysis of flow rate-pressure characteristics and stability," *Journal of Micromechanics and Microengineering*, vol. 15, no. 4, pp. 883–891, 2005.

[183] Y. D. Gao, T. N. Wong, C. Yang, and K. T. Ooi, "Two-fluid electroosmotic flow in microchannels," *Journal of Colloid and Interface Science*, vol. 284, no. 1, pp. 306–314, 2005.

[184] A. Gunther and K. F. Jensen, "Multiphase microfluidics: from flow characteristics to chemical and materials synthesis," *Lab on a Chip*, vol. 6, no. 12, pp. 1487–1503, 2006.

Acknowledgements

A successful doctorate, as the first research experience in one's life, needs not only an advanced and fertile scientific environment, but also the help and support of many different people. I was lucky to find both: colleagues with valuable advices, wonderful friends and caring love. Before embarking on this adventure, I could not imagine that I would meet and work with such a large amount of inspiring and exciting people. I am grateful for this and for all the time that I spent studying, experimenting and sharing thoughts, which made me learn and grow.

I whish to acknowledge Tronics Microsystems for funding this project, Stéphane Renard and Antoine Filipe for following my work and regularly offering precious comments and suggestions. I would also like to thank Christian Pisella for his sympathy and enthusiasm.

My deepest gratitude goes to Prof. Nico de Rooij, who has accepted me in his laboratory and given me the opportunity to work in such an exciting, multidisciplinary and multicultural environment. Here, the careful and stimulating supervision of Alexandra Homsy was most important to successfully complete my PhD and I am thankful to her for all the time and energy she devoted to this project. My job was also easier and more pleasant thanks to Blaise Guélat and Philip Wägli, my fellows and friends in the microfluidics team.

The work presented in Chapter 7 is the result of the enthusiastic inputs that I received from Jérôme Courbat and Danick Briand and the fruitful collaboration with them. I am also grateful to Peter Van der Wal for the long discussions and all the tiny bits of chemistry that I learnt from him. I most value the help of Robert Lockhart in improving my abstracts and presentations and the advice of Giorgio Mattana, who proof-read the Italian version of the abstract.

I am extremely grateful to have found such good colleagues and friends as Jonathan Masson and Rahel Strässle, and for all the time, enriching discussions and activities that I could share with them. Indeed, working in SAMLAB has also been a great experience thanks to all the bright and inspiring people I was with. I would like to thank Terunobu Akyiama, Dara Bayat, Roland Bitterli, Michael Canonica, David de Koninck, Cécile Fattebert, Olivier Frey, Franz Friedrich, Sebastian Gautsch, Rokhaya Gueye, Nicolas Golay, Don Isarakorn, Pattanaphong Janphuang, Fabio Jutzi, Frédéric Loizeau, Olivier Lässer, Francisco Molina Lopez, Wilfried Noell, Yves Pétremand, Sotiria Psoma, Jason Ruan, Sara Talaei, Andres Vasquez Quintero and Yexian Wu.

Moreover, I should also mention and thank Samin Akbari, Caglar Ataman, Simon Dandavino, Luc Maffli, Muhamad Niklaus, Myriam Poliero, Pille Rinne, Samuel Rosset, Jun Shintake and Vinu Venkatraman from LMTS, and Alessandro Ambuehl, Nicolas Ferrier, Paolo Germano, Pascal Meyer, Grégory Savioz, Omar Scaglione and Christophe Winter from LAI. I am glad for the good moments that we spent together.

I also wish to acknowledge Prof. Herbert Shea from LMTS for the valuable feedback on my work, Prof. Christophe Ballif and Rémi Biron from PV-Lab for the help and collaboration with the realisation of ITO electrodes, as well as Ludovica Colella from LMIS4 for showing me and letting me use her setup for conductivity measurements, and Dominique Solignac from Icoflex for helping me with laminated photoresist and sandblasting.

The practical realisation of the pumps and all microfabrication greatly benefited from the skills and expertise of Sylvain Jeanneret's team at CSEM - Division C. I would like to specially thank Sébastien Lani for the precious help in defining process parameters, and Laurent Guillot, Jean-Paul Morel, Stéphane Ischer, Sylviane Pochon and Pierre-André Clerc for their high quality work. Further, Edith Millotte, Rémy Fournier, Giovanni Bergonzi, Sabina Jenny and José Vaquera from Division C, as well as Laure Aeschimann and Mathieu Burri from Nanoworld have also helped me a lot and contributed to make my time in the cleanroom more enjoyable. Finally, this list would not be complete without mentioning the valuable assistance of the CSEM Microscopy Service and I am grateful to Massoud Dadras and Mireille Leboeuf for that.

I should express my gratitude to Karine Frossard for the ready and effective support with administrative matters, to Claudio Novelli for the assistance with computers and the long discussions that I will certainly miss, and to Marie Halm for her good work and for always being so cheerful.

Among the amazing people that I met during my PhD, I wish to thank Barbara Althaus from the EPFL Language Centre for proof-reading my thesis and helping me improve my English, as well as Stephanie Traub and Veronika Vitzthum, who guided my first steps in learning German.

Si mon arrivée en Suisse s'est très bien passée, je dois remercier, entre autres, mon ami Pierre, qui m'a laissé sa chambre dans le très bel appartement qui a été ma maison à Lausanne.

Je souhaite également remercier Isabelle et Daniel pour leur accueil et pour les bon moments que nous avons passés ensemble, ainsi que Floriane, qui a été un grand example d'enthousiasme et de détermination. Elle mérite aussi un remerciement spécial pour toutes les fois où elle m'a déposé à Genève.

Il y a une personne qui m'a beaucoup soutenu, et avec qui j'ai grandi et changé pendant ces années. Benjamin, merci d'être là !

Vorrei ringraziare Michelangelo, che mi ha ospitato per un paio di settimane mentre cercavo casa. Quando poi ho trovato una sistemazione, è stato un piacere condividere l'appartamento con Cristina e Livio, che sono stati degli ottimi compagni nell'avventura del dottorato.

Un ringraziamento particolare va alle persone che nonostante l'ostacolo delle Alpi mi sono vicine dai tempi del liceo e anche da prima: Aline, con il suo pungente senso critico, Laura, con il suo infaticabile entusiasmo, Davide, con il suo desiderio di agire per gli altri. E non posso dimenticare le amiche del collegio, Nadia e Raffaella, che per prime mi hanno mostrato che si può sopravvivere al dottorato.

Infine, non sarei quello che sono e non avrei potuto intraprendere questa bella avventura, se non potessi contare sull'affetto e sull'appoggio di una splendida famiglia. Grazie mamma, papà e Marco, per avermi sempre sostenuto e incoraggiato.

Luca Ribetto
luca.ribetto@a3.epfl.ch

Education

Oct. 2008 - Jan. 2012 *Ph.D. candidate, Microsystems and Microelectronics*
École Polytechnique Fédérale de Lausanne (EPFL), Switzerland
Research on valveless micropumps

Sep. 2006 - Sep. 2008 *M.Sc. in Micro and Nano Technologies for Integrated Systems*
École Polytechnique Fédérale de Lausanne (EPFL), Switzerland
Institut National Polytechnique de Grenoble (Grenoble INP), France
Politecnico di Torino (PoliTO), Italy
Master thesis title: "Indoor Solar Energy Harvesting for Tyndall 25mm Mote"

Sep. 2003 - Sep. 2006 *B.Sc. in Information Technologies*
Institut National Polytechnique de Grenoble (Grenoble INP), France
Politecnico di Torino (PoliTO), Italy

Internships

2008 Tyndall National Institute, Cork (Ireland)
Master thesis work on indoor energy harvesting

2007 Tronics Microsystems, Crolles (France)
Preliminary study for a microfabricated energy harvester

Languages

Italian, native
French, bilingual
English, proficient (level C2 of the common European framework)
German, independent (level B2 of the common European framework)

Publications related to the thesis

L. Ribetto, A. Homsy, N. F. de Rooij, **All-Around-Electrode AC Electro-Osmotic Micropump with Simple Fabrication and Improved Velocity Generation**, Accepted for poster presentation at the 25th International Conference on Micro Electro Mechanical Systems, IEEE MEMS, Paris (France), 29 January - 2 February, 2012

L. Ribetto, J. Courbat, A. Homsy, D. Briand, N. F. de Rooij, **Inkjet-Printed Conductive Polymer Electrodes for AC Electro-Osmosis**, Poster presentation at the 1st Swiss Conference on Printed Electronics and Functional Materials, Basel (Switzerland), 1-2 December, 2011

L. Ribetto, A. Homsy, N. F. de Rooij, **Improved Two-Side AC Electro-Osmotic Micropump**, Oral presentation at the 2nd Conference on Advances in Nano and Microfluidics & Asia-Pacific Symposium on Labs-on-a-chip, Singapore, 6-9 January, 2011

L. Ribetto, A. Homsy, N. F. de Rooij, **Flow Recirculation when Pumping Liquids with AC Electric Fields: Experiments and Simulations**, Poster presentation at the 5th Asia-Pacific Conference on Transducers and Micro-Nano Technologies, APCOT, Perth (Australia), 6-9 July, 2010, *Awarded with the prize for the best student presentation*

Publication not related to the thesis

W. S. Wang, T.O. O'Donnell, L. Ribetto, B. O'Flynn, M. Hayes, and C. O'Mathuna, **Energy Harvesting Embedded Wireless Sensor System for Building Environment Applications**, Proceedings of the International Conference on Wireless Communications, Vehicular Technology, Information Theory and Aerospace & Electronic Systems Technology, Wireless Vitae, Aalborg (Denmark), 17-20 May, 2009